INTERNATIONAL DOCTORAL
SCHOOL OF THE USC

Javier
Fernández Lozano

PhD Thesis

Design of new high-efficiency silicon carbide-based laser power converters

Santiago de Compostela, 2024

Doctoral Programme in Renewable Energy and Energy Sustainability

ESCOLA DE DOUTORAMENTO
INTERNACIONAL DA USC

TESE DE DOUTORAMENTO

DESIGN OF NEW HIGH-EFFICIENCY SILICON CARBIDE-BASED LASER POWER CONVERTERS

Autor

Javier Fernández Lozano

Directores: Antonio Jesús García Loureiro e Natalia Seoane Iglesias

Titor: Antonio Jesús García Loureiro

PROGRAMA DE DOUTORAMENTO EN ENERXÍAS RENOVABLES E SUSTENTABILIDADE ENERXÉTICA

SANTIAGO DE COMPOSTELA

Not far from here, by a white sun, behind a green star, lived the Steelypips, illustrious, industrious, and they hadn't a care: no spats in their vats, no rules, no schools, no gloom, no evil influence of the moon, no trouble from matter or antimatter – for they had a machine, a dream of a machine, with springs and gears and perfect in every respect. And they lived with it, and on it, and under it, and inside it, for it was all they had- first they saved up all their atoms, then they put them all together, and if one didn't fit, why they chipped at it a bit, and everything was just fine.

Stanislav Lem

Como facerá Don Fulano pra ganar dez mil reás e aforrar cen mil?

Castelao e Victor Marcos Rodriguez

USC
UNIVERSIDADE DE SANTIAGO DE COMPOSTELA

Agradecimientos

Teño moito que agradecer. En primer lugar, a meus pais, por meterme na cabeza a ciencia dende neno. Sei que han de estar orgullosos. A Antonio e Natalia, pola inmensa paciencia e dedicación que demostran cada día traballando con nós. A tese, con algo de xeito e boa tutela, lévase ben, máis que ben. Eternamente agradecido.

A Julián por facer o que leva facendo media vida, aturarme no traballo. A Marta, Ro e Adras por aturarme na casa nesta etapa, cousa que se di máis fácil do que se fai. A Enrique por facer o que fai un bo científico, facer moi fácil o que parece moi difícil. A toda a xente deste centro que crea cada día un ambiente excepcional de rojos e marigallos no cual non podo sentirme máis cómodo.

Gazas a toda a xente que está na miña vida, que non é pouca, pero toda é valiosa.

August 2024

USC
UNIVERSIDADE DE SANTIAGO DE COMPOSTELA

Contents

Resumo **1**

1 Introduction **11**

1.1 Motivation 11

1.2 Hypotheses and general objectives 15

2 Methodology **17**

2.1 *Technology Computer Aided Design* (TCAD) models and material parameters 18

2.2 Devices 22

2.3 Optimization 24

3 Discussion **31**

3.1 Comparative of three *Silicon Carbide* (SiC) polytypes 32

3.2 Optimization of *Vertical Epitaxial Hetero-Structure Architecture* (VEHSA) devices using the *Photogeneration and Performance Optimization* (PhPO) algorithm 37

3.3 Cubic SiC on advanced *Laser Power Converter* (LPC) devices 41

Conclusions **55**

Implementation of SiC polytypes in the hLPC devices 56

Development of VEHSA optimization algorithm: PhPO 56

3C-SiC as base material for advanced architectures 57

Future work 59

Bibliography **61**

USC UNIVERSIDADE DE SANTIAGO DE COMPOSTELA

A Published works **71**

A.1 Journal articles in this thesis 71

A.2 Works related to this thesis 102

List of Figures **103**

List of Tables **105**

Acronyms **107**

USC UNIVERSIDADE DE SANTIAGO DE COMPOSTELA

Resumo

A transmision de alta potencia láser, ou polas súas siglas en inglés HPLT, está chamada a revolucionar o campo da transmisión de potencia inalámbrica sen fíos. Esta tecnoloxía consiste na emisión dun feixo monocromático para transferires potencia a un receptor remoto ou *laser power converter* (LPC). O HPLT permite transferir potencia a través de fibra óptica ou inclusive a través do espacio, reemplazando ao cableado convencional. Isto permite acadar illamento eléctrico e moi baixas interferencias electromagnéticas. As aplicacións para esta tecnoloxía pasan por transferir simultáneamente datos e enerxía ou alimentar antenas remotas, *rovers* ou satélites.

Na actualidade esta tecnoloxía baséase no emprego do arseniuro de galio (GaAs), con LPCs que superan o 50% de eficiencia. O dispositivo con maior rendimento acada un 68.9% a unha densidade de potencia láser de 11.4 W cm^{-2}. A arquitectura empregada neste dispositivo é a convencional *horizontal laser power converter* ou hLPC. Non obstante, este dispositivo perde eficiencia conforme aumenta a potencia do láser debido as perdas por resistencia serie. Isto representa unha importante limitación para a tecnoloxía, xa que impide enviar maiores densidades de potencia a dispositivos que requiran un consumo maior, tendo que aumentar tanto o área do LPC como a anchura do feixe láser. Ademáis, dado que a eficiencia dos LPCs tende a aumentar coa densidade de potencia (a voltaxe de circuíto aberto aumenta coa inxección de portadores), esta limitación por resistencia serie anula esta vía de mellorar a tecnoloxía.

Para mellorar este paradigma, desenrrólanse novas arquitecturas que lidien con este efecto. Unha delas é a *vertical laser power converter* ou vLPC, que evita o sombreado debido aos contactos metálicos e permite reducir as operdas por resistencia serie varios ordes de magnitude. Outra é a chamada *Vertical Epitaxial Hetero-Structure Architecture* ou VEHSA, que consiste en apilar verticalmente células para dividir a corrente e aumentar a voltaxe,

USC UNIVERSIDADE DE SANTIAGO DE COMPOSTELA

disminuíndo así as perdas por resistencia serie. Esta arquitectura presenta o problema de optimizar ben a estructura, dado que a corrente que proporciona cada célula ten que ser a mesma, tendo en conta que a corrente total que se extrae do dispositivo é a menor das correntes proporcionadas por cada célula. Na actualidade, emprégase para este cometido a lei do decaemento exponencial de Beer-Lambert para calculares a fotoxeración en cada célula. Este método é útil en materiais ben coñecidos de *bandgap* directo como o GaAs, pero resultan ineficaces cando se empregan materiais de *bandgap* indirecto.

Outra vía para mellorar a eficiencia dos LPCs é empregar materiais de moi alto bandgap. Estos materiais poden reducir tanto as perdas entrópicas (intrínsecas á conversión fotón-par) como as perdas por resistencia serie, dado que para unha mesma densidade de potencia láser o feixe monocromático terá menos fotóns con máis enerxía, aumentando a voltaxe e disminuíndo a corrente que provee o dispositivo. Uns materiais prometedores son os politipos de carburo de silicio (SiC). Os politipos máis habituais son o cúbico (3C-SiC), 4H hexagonal (4H-SiC) e o 6H hexagonal (6H-SiC). Os dous politipos hexagonais son os máis empregados na industria, en particular no campo da electrónica de potencia. O 3C está a ser investigado polas propiedades isotrópicas e altas movilidades de portadores. Ademais, estes politipos presentan propiedades moi interesantes como estabilidade térmica e resistencia á radiación, o que os converte en candidatos moi interesantes para aplicación espaciais, onde os dispositivos sofren condicións extremas. Por último, os procesos de fabricación de LPCs feitos destes politipos empregarían materiais non críticos, abundantes (carbono e silicio) e con procesos que non involucran axentes tóxicos, ao contrario que no arseniuro de galio.

Co contexto mostrado previamente, este traballo tratará de dar resposta aos diferentes retos actuais coas seguintes hipóteses:

H1. *O emprego de materiais de alto bandgap nos LPCs aumentará a eficiencia dos dispositivos en todo o rango de potencias láser, reducindo tanto as perdas intrínsecas como as perdas por resistencia serie.*

H2. *O rendemento de arquitecturas avanzadas de LPCs como a VEHSA pode mellorarse mediante o emprego de unha modelización TCAD detallada máis novos algoritmos de optimización.*

H3. *O uso combinado de materiais de alto bandgap e arquitecturas avanzadas pode reducir aínda máis as perdas por resistencia serie, permitindo convertir moi eficientemente elevadas densidades de potencia láser.*

USC
UNIVERSIDADE
DE SANTIAGO
DE COMPOSTELA

Declarados os obxectivos da tese, no Capítulo 2 (Metodoloxía) preséntanse as principais ferramentas e procedementos utilizados neste traballo, así como os dispositivos LPC empregados e as súas características. Isto inclúe os parámetros característicos dos materiais e os modelos empregados nas simulacións, así como unha descrición dos algoritmos de optimización. Comézase por unha descripción das principais figuras de mérito (FOM) que caracterizan os dispositivos fotovoltaicos, como son a voltaxe de circuíto aberto (V_{OC}), a corrente de curtocuicuíto (I_{SC}), o punto de máxima potencia (P_m), a voltaxe e corrente no punto de máxima potencia (V_m, I_m), o factor de cheado (FF) e a eficiencia (Eff).

A continuación descríbense detalladamente os modelos e parámetros empregados no curso das simulacións realizadas con Silvaco ATLAS, un software axeitado para a simulación de dispositivos semiconductores, empregado habitualmente en fotovoltaica e concretamente en LPCs. Atendendo ás propiedades máis notorias dos semiconductores presentados neste traballo (3C-SiC, 4H-SiC, 6H-SiC e GaAs), o 4H-SiC (3,23 eV) presenta a maior enerxía de bandgap, o que o converte nun candidato sólido como material base para os LPC. O 6H-SiC tamén ten un bandgap alto de 3,02 eV. O 3C-SiC ten a enerxía de bandgap máis baixa dos polimorfos de SiC propostos (2,36 eV). Non obstante, a condutividade térmica é maior para o 3C-SiC (500 W m^{-1} K^{-1}) que para o 4H-SiC e o 6H-SiC (350 e 320 W m^{-1} K^{-1}, respectivamente). Isto podería situar o 3C-SiC como a opción preferida para material base dos LPC en condicións extremas, sendo máis adecuado para aplicacións espaciais. Cómpre sinalar que tanto a enerxía de bandgap como a condutividade térmica do GaAs (1.42 eV, 50 W m^{-1} K^{-1}), o material actual de referencia, son significativamente inferiores ás dos politipos de SiC.

Para emular realisticamente o comportamento do SiC, usamos o modelo de Caughey-Thomas para describir as mobilidades dos portadores en función da densidade de dopaxe, un modelo axeitado cando se considera un campo eléctrico baixo. No caso do GaAs, as mobilidades dependentes da dopaxe son calculadas internamente por Silvaco a partir de datos extraídos de fontes experimentais fiables. Outros modelos postos en xogo son o modelo de estreitamento de *bandgap* de Lindefelt (desenrrolado para SiC) e os modelos de recombinación de Shockley–Read–Hall (SRH), Auger e recombinación óptica ou banda a banda. Todos os parámetros propios dos modelos empregados extráense de recentes estudos experimentais.

Unha vez descritos os modelos dos materiais, preséntanse as arquitecturas empregadas neste traballo. Estas son a hLPC, vLPC e VEHSA. Todos os dispositivos estudados teñen a mesma estrutura de célula, catro capas con dopaxes tipo n+/n/p/p+. A estrutura de dispositivo

USC UNIVERSIDADE DE SANTIAGO DE COMPOSTELA

máis común nesta tecnoloxía é o hLPC. Esta arquitectura experimenta unha degradación da eficiencia a altas densidades de potencia láser (>15 W cm^{-2}) debido ás perdas óhmicas. No hLPC, a luz incidente é paralela ao fluxo de corrente e perpendicular ao ánodo e ao cátodo. Nesta arquitectura, tense que acadar un compromiso entre o camiño óptico e a lonxitude de difusión dos portadores, xa que os procesos de absorción e transporte teñen lugar na mesma dirección. Nos dispositivos baseados en semiconductores de bandgap indirecto, onde a absorción de fotóns é menor que nos semiconductores directos, úsase unha capa reflectante texturizada para aumentar o camiño óptico, mellorando considerablemente a absorción de luz e o reciclado de fotóns. Este mecanismo evita un dispositivo excesivamente longo no que os portadores minoritarios non sobrevivirían. Nos dispositivos hLPC modelados neste traballo, esta capa colócase na parte inferior do dispositivo.

Para superar a limitación das perdas óhmicas a altas densidades de potencia láser, os autores propuxeron en trabalos previos unha nova estrutura de dispositivo a través de simulacións numéricas, un vLPC baseado en GaAs que acada eficiencia de máis do 76% a 3000 W cm^{-2}. Os beneficios desta arquitectura son a ausencia de efectos de sombra por parte da grella metálica frontal e unha drástica redución da resistencia serie. No vLPC, a luz incidente é perpendicular ao fluxo de corrente e paralela ao ánodo e ao cátodo. Como na arquitectura vertical non hai compromiso entre a absorción de fotóns e o transporte de portadores, a anchura do dispositivo é independente da iluminación e axústase para unha absorción óptima. Outra característica interesante é a posibilidade de conectar varios dispositivos mediante unións túnel para aumentar a área de iluminación.

Outra estrutura de dispositivo especialmente salientable é a arquitectura VEHSA, que destaca entre os LPCs de multixunción. Esta disposición consiste en apilar monoliticamente células hLPC. A principal vantaxe desta arquitectura é a capacidade de distribuír a corrente a través das células, o que reduce as perdas por quentamento de Joule. Isto permite operar baixo altas concentracións de potencia láser. A eficiencia récord actual para unha VEHSA baseada en GaAs é do 66,3% e foi alcanzada cun dispositivo de 5 células a 150 W cm^{-2}. Neste traballo, os autores tamén exploraron VEHSAs con ata 20 células para manexar potencias de entrada aínda maiores. Porén, cando se incrementou o número de células, tamén aumentou o efecto do desaxuste de corrente debido a problemas intrínsecos de fabricación, deteriorando a eficiencia. A optimización dos dispositivos VEHSA é complexa debido á gran dificultade para avaliar as correntes individuais de cada célula.

Unha vez descritos os dispositivos, preséntase o algoritmo desenrrolado para mellorar a

USC
UNIVERSIDADE DE SANTIAGO DE COMPOSTELA

optimización das diferentes arquitecturas. En primeiro lugar descríbese un algoritmo iterativo que recorre os parámetros de deseño, barrendo os valores ata atopares o óptimo. Este algoritmo é útil para dispositivos que consten de unha única célula. Nembargantes, a arquitectura VEHSA require rutinas de optimización adicadas. Na arquitectura VEHSA, un factor clave que afecta ao rendemento dos dispositivos é o axuste preciso das correntes producidas por cada célula, xa que a corrente total extraída do dispositivo será a menor de todas as células contribuintes. Ata o de agora, os dispositivos VEHSA máis avanzados conseguen o axuste de corrente aplicando a lei de Beer-Lambert, correspondente á atenuación exponencial da luz. A fotoxeración integrada debería de ser a mesma en todas as células.

Presentamos un método de optimización deseñado para superar estes problemas, válido tanto para dispositivos VEHSA de bandgap directo como indirecto, independentemente de se están alimentados por un láser ou por luz solar. O sistema consiste nun meticuloso modelado TCAD do dispositivo VEHSA combinado cun algoritmo de optimización iterativa. Dado que o modelado de unións túnel en Silvaco pode ser problemático, empregamos unha solución estándar que consiste en modelar as unións túnel como condutores perfectos para acelerar o tempo de simulación. Deste xeito, permitimos a extracción das correntes das unións túnel (TJCs), acoplándoas a electrodos con resistencias variables agrupadas. Estas resistencias poden tomar valores moi altos para simular o dispositivo completo, evitando a corrente a través destes contactos, ou valores realistas baixos para obter as diferenzas entre as correntes producidas en células adxacentes. Esta é unha ferramenta útil para axustar con precisión as correntes de todas as células e mellorar o rendemento do dispositivo VEHSA completo.

O algoritmo de optimización é un proceso iterativo que implica dúas etapas: *Photogeneration and Performance Optimization* (PhPO). Na primeira etapa, o bucle de fotoxeneración, a altura total do dispositivo (DH) é optimizada para absorber a maior parte do feixe sen aumentar innecesariamente o tamaño do dispositivo, o que afectará ao transporte do transportador. Como primeiro enfoque, utilízase a lei de Beer-Lambert para obter unha estimación inicial. O algoritmo itera, aumentando/reducindo o DH, ata que se cumpran dous criterios: i) un valor mínimo de luz absorbida, que establece as máximas perdas de fotoxeneración permitidas do total da luz incidente e ii) un valor máximo de fotoxeneración, que evita que o dispositivo creza infinitamente para absorber a totalidade dos fotóns. O DH óptimo resultante utilízase como entrada para a seguinte etapa, o bucle de rendemento. Nesta segunda etapa, o optimizador mellora o rendemento das células de forma individual. Este proceso comeza cunha subrutina que evalúa de forma iterativa os TJCs e modifica os tamaños relativos de cada célula. Este

USC UNIVERSIDADE DE SANTIAGO DE COMPOSTELA

proceso itera ata que todos os TJCs contribúan coa mesma corrente e o valor estea por baixo dunha certa tolerancia, por exemplo, 1/1000 do I_{SC} extraído no ánodo. Cando isto ocorre, o algoritmo optimiza os parámetros de deseño de cada subcélula coma no caso das hLPC e vLPC. Este proceso itérase ata que o dispositivo é idóneo.

Unha vez presentada a metodoloxía, móstranse os resultados obtidos nesta tese. A discusión consistirá primeiro na implementación dos tres politipos de carburo de silicio (3C, 4H e 6H) empregando a arquitectura habitual hLPC, para probar a hipótese **H1**. Preséntanse os parámetros de deseño dos hLPC para os tres politipos a 4 densidades de potencia: 1, 10, 100 e 1000 W cm^{-2}. Ao aumentares a densidade de potencia incidente, os dispositivos tenden a facerse máis pequenos para reducir a densidade de portadores e con eles o impacto da recombinación Auger. Tal e así que o 6H é o material máis afectado por Auger, e redúcese dende 83 μm a 38 μm ao variar a potencia de 1 a 1000 W cm^{-2}, mentras que o 3C, o menos afectado reduce de 83 μm a 75 μm. É salientable que cun valor de densidade de potencia de 1 W cm^{-2}, os tres hLPC obteñen case a mesma eficiencia, arredor do 78%. Teóricamente, agárdase que canto maior sexa a banda prohibida, maior sexa a eficiencia dos LPCs, se non se teñen en conta outras propiedades do material. Isto débese a perdas relacionadas coa absorción de luz. Para garantir unha fotoxeneración adecuada dentro dos dispositivos sen aumentar moito a súa altura, escóllense longitudes de onda incidentes para cada material que garantan un coeficiente de extinción de polo menos k = 2e-4. O 3C perde unha eficiencia do 1%, o 6H do 2.5% e o 4H do 5%. Según aumenta a potencia, o 3C mellora o seu rendemento ata os 100 W cm^{-2}, momento no que alcanza un 84.6% de eficiencia, para logo degradarse por perdas en resistencia serie. O 6H sufre por recombinación Auger e o 4H non escala coa potencia debido á alta densidade de estados, que limita o crecemento da V_{OC}. Para comparar, o actual mellor hLPC experimental de GaAs alcanza unha eficiencia do 68.9% a 11.4 W cm-2, que é un 13.4% inferior á alcanzada polo 3C a esa potencia, aínda que non se poden comparar directamente xa que os dispositivos de SiC aínda non se fabricaron. Para concluír, realízanse probas de resiliencia coa temperatura dos dispositivos optimizados de 3C, 4H e 6H a 1000 W cm^{-2}. O 3C demostra ser o menos damnificado polo aumento da temperatura.

A continuación preséntanse os resultados do algoritmo de optimización PhPO, pensado para mellorar a optimización da arquitectura VEHSA, como consta na hipótese **H2**. Para validar a metodoloxía, inicialmente modélase unha VEHSA de 5 células baseada en GaAs (VEHSA PT5 de agora en diante), que está deseñada a partir dun dispositivo experimental que actualmente ten o récord de eficiencia a temperatura ambiente. O dispositivo TCAD reproduce

USC UNIVERSIDADE DE SANTIAGO DE COMPOSTELA

con precisión os valores de I_{SC} e V_{OC} do dispositivo experimental, e as lixeiras diferenzas na forma da curva en voltaxe no punto de máxima potencia (V_m) e voltaxes intermedias poden derivar de problemas de fabricación. Unha vez que demostramos a validez da nosa metodoloxía de simulación, aplicamos o método PhPO para mellorar aínda máis o rendemento do dispositivo. As alturas das células que compoñen o dispositivo VEHSA se axustan ata que as correntes que provee cada célula son iguais cun erro por debaixo de 1/1000 do valor de I_{SC} do ánodo. Os valores relativos NH/PH devolven alturas da capa N moito maiores para células máis finas (as células superiores) (por exemplo, 0.9/0.1 para a primeira célula), que diminúen gradualmente a medida que aumenta o CH (por exemplo, 0.3/0.7 para a quinta célula). Os valores de dopaxe diminúen significativamente a $1 \cdot 10^{15}$ cm^{-3}, un valor tres ordes de magnitude inferior aos observados nos parámetros de deseño iniciais. O VEHSA PT5 optimizado logra o mesmo V_{OC} que os dispositivos calibrados e experimentais e aumenta o I_{SC} en un 6%, levando a unha eficiencia do 75.8%, un valor un 9.5% maior que o do VEHSA PT5 experimental. Estas melloras débense ó meticuloso proceso de igualar as correntes das células e a optimización individual dos parámetros de deseño de cada célula. As curvas IV de cada célula individual da VEHSA PT5 calibrada (experimental) sofren de desaxuste de corrente, e tamén hai un notable desaxuste de V_{OC}. Estes efectos redúcense drásticamente na VEHSA PT5 optimizada, onde as curvas IV son moi semellantes para todas as células.

Por último, para probar a hipótese **H3**, impleméntase o politipo de carburo de silicio cos mellores resultados, o 3C-SiC, nas arquitecturas avanzadas vLPC e VEHSA. En primeiro lugar, emprégase a arquitectura vLPC. Optimízanse os parámetros de deseño de dispositivos con esta arquitectura para o rango de densidade de potencia 1-3000 W cm^{-2}. Para comparar o efecto da resistencia serie dos dispositivos vLPC de 3C-SiC cos dispositivos hLPC, as curvas IV normalizadas resultan de utilidade. Para o vLPC non hai ningunha degradación notable debido á resistencia serie en ningún valor de potencia, ao contrario que no hLPC, onde este efecto é notable a 1000 W cm^{-2} e degrada significativamente o rendemento do hLPC a valores de potencia máis altos. A eficiencia dos vLPC crece linealmente co logaritmo da potencia para o rango estudado. Este resultado, oposto ao comportamento no hLPC, provén da baixa resistencia serie e da menor presenza de recombinación Auger nos dispositivos vLPC.

Analizando como se comporta V_{OC} para cada arquitectura, os valores de V_{OC} para a arquitectura vLPC son máis baixos en comparación cos da hLPC. Isto pódese explicar considerando a diminución na taxa de fotoxeneración a través de todo o longo do dispositivo. Na hLPC, existe un intercambio entre a absorción de luz e a lonxitude de difusión dos portadores. De

USC UNIVERSIDADE DE SANTIAGO DE COMPOSTELA

feito, requirese unha capa posterior texturizada para aumentar a absorción óptica sen aumentar drásticamente as perdas por recombinación. Isto conduce a unha alta concentración de portadores e, polo tanto, a un maior V_{OC}. Na vLPC, non hai tal intercambio, xa que a absorción de luz ocorre nunha dirección perpendicular ao fluxo de corrente. Isto produce unha mellor absorción ao aumentar o ancho do dispositivo sen afectar á difusión dos portadores. Debido ao ancho da vLPC (360 μm), a taxa de fotoxeneración diminúe nun orde de magnitude a través do dispositivo. A carga recollida, e polo tanto o V_{OC}, diminúen á medida que a luz penetra máis no vLPC. Dado que o ánodo e o cátodo cubren todo o ancho do dispositivo, o valor global de V_{OC} corresponderá á tensión na área con menos iluminación. Por tanto, o ancho da vLPC debe alcanzar un compromiso entre ser suficientemente grande para garantir a absorción da maior parte do feixe e manter densidades de portadores en exceso suficientes para evitar a degradación do V_{OC} nas áreas menos iluminadas.

A implementación de 3C-SiC faise en dispositivos tipo VEHSA con 2, 3 e 4 células. Optimízanse diferentes dispositivos para o rango de potencia 1-3000 W cm^{-2}. O algoritmo PhPO axusta as alturas individuais das células (CH) para minimizar a diferenza de corrente producida entre as células. As células superiores son máis pequenas que as inferiores, xa que a fotoxeneración decae a medida que a luz atravesa o dispositivo, polo que cada CH necesita ser maior para xerar a mesma cantidade de portadores que na célula anterior. Estes valores de CH non se poden obter a través de cálculos utilizando o decaemento exponencial de luz, xa que o camiño óptico está altamente incrementado debido aos mecanismos de captura de luz situados na parte inferior do dispositivo. Ademais, o optimizador atopou consistentemente que as configuracións óptimas son aquelas coa capa P maior que a capa N. Isto é máis pronunciado a baixas densidades de potencia de entrada e nas células inferiores (as máis próximas á célula inferior).

Para finalizar, realízase unha comparativa dos dispositivos descritos neste traballo cos do estado da arte. A eficiencia do 3C-SiC vLPC é comparable á do 3C-SiC hLPC para o rango de potencia de 1-100 W cm^{-2}. A valores de potencia máis altos, a arquitectura vertical non parece estar limitada pola resistencia serie, xa que a eficiencia segue aumentando linealmente co logaritmo de potencia. Os resultados do 3C-SiC vLPC tamén se comparan cos do vLPC baseado en GaAs, que estableceu o anterior récord de eficiencia para un LPC modelado a altos valores de potencia, logrando unha eficiencia do 76.3% a 3000 W cm^{-2}. O 3C-SiC vLPC mostra unha eficiencia extremadamente alta do 87.4% a 3000 W cm^{-2}, aumentando en 11.1% o resultado acadado polo vLPC de GaAs a este valor de potencia. Isto é notable, xa

USC UNIVERSIDADE DE SANTIAGO DE COMPOSTELA

que a metodoloxía utilizada no vLPC de GaAs é esencialmente a mesma que a que se seguiu no seu traballo. Por tanto, a diferenza nos resultados podería atribuírselle principalmente á redución da corrente debido a unha menor densidade de fluxo de fotóns e a propiedades de materiais máis favorables do 3C-SiC en comparación coas do GaAs. Os dispositivos 3C-SiC VEHSA obteñen eficiencias un ≈2% superiores que os dispositivos hLPC e vLPC no rango de 1-100 W cm^{-2}. Estas pequenas diferenzas débense á maior altura óptima do dispositivo das estruturas VEHSA en comparación co hLPC, permitindo que atrapen unha parte maior do feixe; e non hai diminución do V_{OC} debido á decrecemento da concentración de portadores como no vLPC. É importante destacar que os dispositivos propostos de 3C empregando a arquitectura VEHSA superan o actual dispositivo experimental de mellor rendemento por un 19.7%, a pesar de que os dispositivos propostos aínda non foron fabricados, polo que o rendemento final pode verse afectado por procesos de fabricación. A 3000 W cm^{-2} todos os dispositivos amosan sinais de degradación da eficiencia agás o VEHSA-4. Esta estrutura supera o resto dos dispositivos VEHSA a este valor de potencia, mostrando unha eficiencia do 87,4%. Isto demostra claramente que aumentar o número de células mitiga a degradación da eficiencia debido ás perdas por resistencia serie a altas densidades de potencia de entrada. É importante notar que o vLPC mantén consistentemente unha eficiencia moi similar á do VEHSA-4, implicando que ambas as estratexias son capaces de mitigar o efecto da resistencia serie.

Como conclusión, os resultados deste traballo xeran confianza nunha nova xeración de convertidores de potencia por láser coa capacidade de revolucionar o mercado e ampliar as posibles aplicacións da tecnoloxía de transmisión de potencia sen fíos. Aínda que o rendemento dos LPC baseados en SiC real pode verse afectado por problemas de fabricación, o traballo presentado mostra que o uso combinado de 3C-SiC e arquitecturas avanzadas son adicións beneficiosas e abren unha ruta prometedora cara á transmisión eficiente de densidades de potencia láser ultra-altas.

USC UNIVERSIDADE DE SANTIAGO DE COMPOSTELA

Chapter 1

Introduction

This thesis is organized in four chapters. Chapter 1 focuses on contextualizing the work carried out, as well as showing the main hypotheses and objectives. Chapter 2 describes the methodology and the set of tools studied and implemented. This includes the *Technology Computer Aided Design* (TCAD) models and material parameters used, the structure and characteristics of the modeled devices and the optimization algorithms developed. In chapter 3, the discussion of the contents corresponding to the core publications of this work will be carried out. First, the results of the silicon carbide polytypes in the most common power converter architecture are presented. Next, the results of the developed optimization algorithm for an advanced architecture are shown. At last, the best performance polytype is implemented in two advanced architectures. A comparative with the state-of-the-art is presented.

Finally, the conclusions highlight the main contributions of this work, presenting the most relevant results and proposing possible future lines of research. In addition, Appendix A will show the articles that compose this thesis, together with participations in both international and national congresses.

1.1 Motivation

The *High-Power Laser Transmission Technology* (HPLT) has been pointed as one of the most promising technologies for far-field wireless power transfer[1]. This technology consists of the emission of monochromatic light to transfer power onto a remote photovoltaic receiver or *Laser Power Converter* (LPC), and is considered a key development in the emerging *Wireless Power Transfer* (WPT) field[1], which has become an increasingly profitable market[2]. HPLT

USC UNIVERSIDADE DE SANTIAGO DE COMPOSTELA

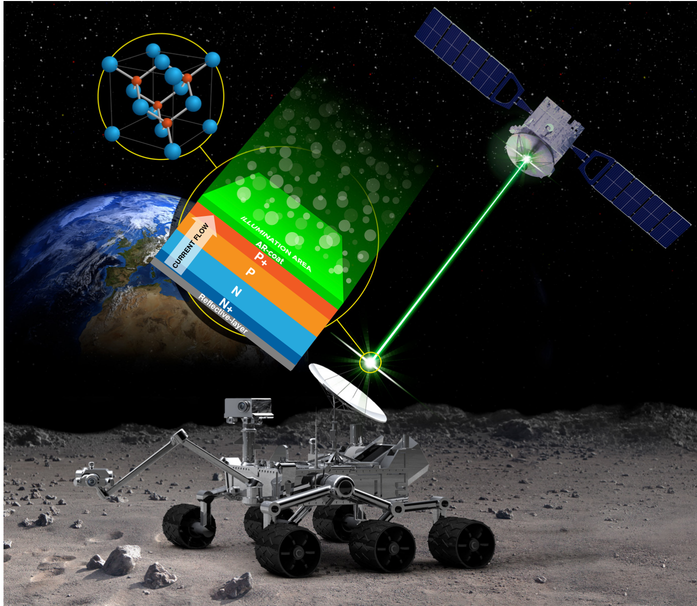

Figure 1.1: Artistic example of a high power laser transmission application, a moon rover powered by a remote laser. In the zoom-in yellow circles, a horizontal laser power converter and a cubic silicon carbide structure are depicted.

offers the possibility of transferring power through optic fiber, replacing conventional copper wires and thus reducing the risk of sparks, which is desirable in workplaces under an ATEX directive[3], or through free space, suitable for aerospace environments. This technology allows to overcome the limitations of conventional wiring since it provides electrical isolation and a reduction of electromagnetic interference and electrical noise[4]. There are many applications of this technology, such as the simultaneous transferal of power and data[5, 6] and optically powering remote antennas[7], aerial vehicles[8] or satellites[9, 10]. Figure 1.1 depicts the optical powering of a rover in a space application.

The state of the art of the photovoltaic receivers or LPCs are mostly dominated by III-V compounds, specifically *Gallium Arsenide* (GaAs)[11]. Multiple studies have achieved efficiencies over 50% using GaAs-based LPCs[12, 13, 14, 15, 16, 17, 18]. There are reports of conversion efficiencies exceeding 60% at room temperatures[16] with a record efficiency conversion of 68.9% at 11.4 W cm^{-2}, but as the input power density increases these LPCs suffer from efficiency degradation due to ohmic losses[17]. This is a relevant constrain of current

USC
UNIVERSIDADE DE SANTIAGO DE COMPOSTELA

HPLT technology as it strongly limits the amount of power density to be transferred to the remote system. To face this challenge, new architectures have been proposed[19, 20, 21, 22].

One of the proposals to overcome this limitation is the *vertical Laser Power Converters* (vLPC) design, proposed by Outes et al.[19]. This configuration, presented by numerical simulations, is a GaAs-based vertical tunnel-junction which achieves efficiencies of more than 76% at a laser power density of 3000 W cm^{-2}. The benefits of this architecture are no shadowing effects from metal grid and a very low series resistance ($\approx 10^{-5}\Omega$cm^{-2}).

Other noteworthy arrangements are multijunction LPCs. The *Vertical Epitaxial Hetero-Structure Architecture* (VEHSA) stands out among these. It consists of monolithically stacking P/N tunnel junctions[16], which is also the main pathway to achieve ultra-high efficiencies on concentrating photovoltaic solar cells[23]. The major advantage of this architecture is to distribute the current over the P/N junctions, which reduces Joule heating losses. This allows to operate under high laser power concentrations, increasing the efficiency due to the *open circuit voltage* (V_{OC}) enhancement associated with higher carrier concentration. The V_{OC} also benefits from a greater Fermi level splitting in thin layers[24]. However, the optimization of VEHSA devices is challenging because of the extreme difficulty of evaluating their individual cell currents. Up to date, the optimization is mainly done by simple approximations using the Beer-Lambert law[25], which only accounts for the photogeneration of each cell. This method is only meaningful to VEHSA devices made of well-known direct bandgap materials like GaAs, since design parameters like doping values and relative P/N sizes are extrapolable from published data[26] and the light decays exponentially in the bulk of the device, as no light-trapping mechanisms are needed. Nevertheless, not measuring the currents of each cell hinders the current matching and the optimization of design parameters, reducing the performance of the device. Although new optimizations paths have been described in literature, such as including tabulated quantum efficiency values in the photogenerated current estimation[27, 28], more sophisticated optimization techniques that broaden the range of VEHSAs are missing. This is of particular interest in the context of materials with indirect high-bandgap like *Silicon Carbide* (SiC), which has been identified as a potential new route to ultra-high efficiency LPCs[29].

Indeed, to further improve the performance of the technology, materials with high bandgap have been pointed out[29, 30, 31]. These materials will not only reduce the series resistance losses due to the higher energy of the incident photons, increasing the outcome voltage and reducing the current, but they will also reduce the intrinsic entropic losses. In this sense, the

USC UNIVERSIDADE DE SANTIAGO DE COMPOSTELA

use of high bandgap materials such as SiC will be beneficial over commonly used photovoltaic materials as *Silicon* (Si) or GaAs, which have a lower energy bandgap when compared with this material. In the last two decades, silicon carbide has been extensively researched, and their main applications are in the field of power electronics[32]. So far, *Hexagonal 4H Silicon Carbide* (4H-SiC) and *Hexagonal 6H Silicon Carbide* (6H-SiC) hexagonal polytypes are the most employed[33]. Due to the high electron mobility and isotropic properties of *Cubic Silicon Carbide* (3C-SiC)[34], efforts are been made to obtain high quality 3C crystals[35]. Indeed, long carrier lifetimes of 8.2 μs have been achieved in 3C grown by sublimation epitaxy[34]. These values are comparable to those of post growth treated chemical-vapor-deposition grown 4H[36] and 6H[37]. Beyond the high bandgap of these materials, silicon carbide polytypes exhibit other interesting properties. The thermal stability, resistance to radiation and dielectric strength[38, 39] of these polytypes make them very interesting candidates for electronic devices and sensors in space applications, where other materials like Si or GaAs will suffer great degradation due to harsh environments[40, 41]. Note that these polytypes are also good candidates to manufacture multijunction VEHSA devices, since the requirements for the *tunnel junctions* (TJ) materials are a high conductivity, optical transparency and low lattice mismatch[42]. The highly doped SiC polytypes used as TJ exhibit great conductivity, low absorption coefficient (the absorption is negligible when compared to that of the whole device) and no lattice mismatch. Furthermore, the manufacturing of LPCs made of SiC polytypes is based on non-critical raw materials (compared with the scarcity of III-V materials), more eco-friendly processes (employs less toxic agents than GaAs) and reuses some of the low-cost Si fabrication procedures[43].

This work is focused on both improving the overall efficiency of the HPLT technology and extending the operational laser power density range by reducing the series resistance losses. For this purpose, the suitability of SiC as base material for LPCs is tested, by comparing the efficiency of three different polytypes (3C, 4H and 6H) for the common *horizontal Laser Power Converter* (hLPC) architectures. To extend the use of SiC to advanced architectures, a new universal methodology to optimize the design of VEHSA devices is proposed. The procedure, based on combining device modeling with a multistage optimization algorithm, allows to further optimize state-of-the-art VEHSAs and to design and optimize new multijunction devices for both direct or indirect bandgap materials. Finally, the feasibility of the best performance SiC polytype as base material for advanced LPC architectures is tested in vLPC devices and VEHSAs with 2 (VEHSA-2), 3 (VEHSA-3) and 4 (VEHSA-4) cells. The obtained results

USC UNIVERSIDADE DE SANTIAGO DE COMPOSTELA

open a promising new path to efficiently transmit high power energy densities.

1.2 Hypotheses and general objectives

The main research lines of this thesis are based on the following hypotheses:

H1. *The use of high bandgap energy materials in Laser Power Converters (LPCs) will increase the overall efficiency by reducing the intrinsic entropic losses and the series resistance losses.*

H2. *The performance of advanced LPC architectures such as the VEHSA can be enhanced through detailed TCAD modeling and new optimization algorithms.*

H3. *The combined use of high bandgap materials and advanced architectures will reduce even further the series resistance losses, allowing to efficiently convert ultra-high laser power densities.*

In order to validate these hypotheses, the different general objectives shown below are framed:

O1. *Implement three SiC polytypes (3C, 4H and 6H, with bandgap energies of 2.36, 3.23 and 3.02 eV) as base materials for the common hLPC configuration.*

O2. *Development of a new algorithm (Photogeneration and Performance Optimization (PhPO)) to optimize the VEHSA architecture.*

O3. *Design and optimize novel LPCs based on the best performance SiC polytype and using advanced architectures such as the vLPC and VEHSA.*

To fulfill objective O1 the following works were presented in journals:

- Javier F. Lozano, Natalia Seoane, Enrique Comesaña, Florencia Almonacid, Eduardo F. Fernández, Antonio García-Loureiro. Laser Power Converter Architectures Based on 3C-SiC with Efficiencies >80% *Solar RRL*, 6, 2101077, 2022.

- Javier F. Lozano, Natalia Seoane, Enrique Comesaña, Florencia Almonacid, Eduardo F. Fernández, Antonio García-Loureiro. A new path towards ultra-high efficient laser power converters: Silicon carbide-based multijunction devices. *Results in Engineering*, 21, 101987, 2024.

USC UNIVERSIDADE DE SANTIAGO DE COMPOSTELA

Objective O2 was accomplished in the following journal publication:

- Javier F. Lozano, Natalia Seoane, Enrique Comesaña, Florencia Almonacid, Eduardo F. Fernández, Antonio García-Loureiro. Photogeneration and Performance Optimization (PhPO): A New Algorithm to Improve the Performance of Vertical Epitaxial Hetero-Structure Architecture Laser Power Converters. *IEEE Access*, 11, 84371 - 84378, 2023.

The following works in journals were presented in order to fulfill objective O3:

- Javier F. Lozano, Natalia Seoane, Enrique Comesaña, Florencia Almonacid, Eduardo F. Fernández, Antonio García-Loureiro. Laser Power Converter Architectures Based on 3C-SiC with Efficiencies >80% *Solar RRL*, 6, 2101077, 2022.

- Javier F. Lozano, Natalia Seoane, Enrique Comesaña, Florencia Almonacid, Eduardo F. Fernández, Antonio García-Loureiro. A new path towards ultra-high efficient laser power converters: Silicon carbide-based multijunction devices. *Results in Engineering*, 21, 101987, 2024.

USC
UNIVERSIDADE DE SANTIAGO DE COMPOSTELA

Chapter 2

Methodology

This chapter presents the main tools and procedures used in this work, as well as the LPC devices employed and their characteristics. These include the characteristic material parameters and models used in the simulations, as well as a description of the optimization algorithms.

The performance of a photovoltaic device, either nurtured by solar light or laser power, is reflected in the IV curve, see Figure 2.1. This curve contains several *Figures of Merit* (FoM), as the current extracted from the device without bias applied or *short circuit current* (I_{SC}), the applied voltage at which no current is extracted or V_{OC}, the *maximum power* (P_M) that this device can deliver and the associated magnitudes *voltage at the maximum power point* (V_M) and *current at the maximum power point* (I_M).

The *fill factor* (FF) is a parameter which, in conjunction with I_{SC} and V_{OC}, determines the maximum power from a solar cell. The FF is defined as the ratio of the maximum power from the solar cell to the product of I_{SC} and V_{OC} so that:

$$FF = \frac{P_M}{I_{SC} \cdot V_{OC}} = \frac{I_M \cdot V_M}{I_{SC} \cdot V_{OC}}. \tag{2.1}$$

Graphically, the FF is a measure of the "squareness" of the solar cell and is also the area of the largest rectangle which will fit in the IV curve.

The most important parameter for assessing the operation of a device is the *efficiency* (Eff), which is calculated as a function of the incident *Input power density* (P_{in}) as follows:

$$Eff = \frac{P_M}{P_{in}} = \frac{I_M \cdot V_M}{P_{in}}, \tag{2.2}$$

USC UNIVERSIDADE DE SANTIAGO DE COMPOSTELA

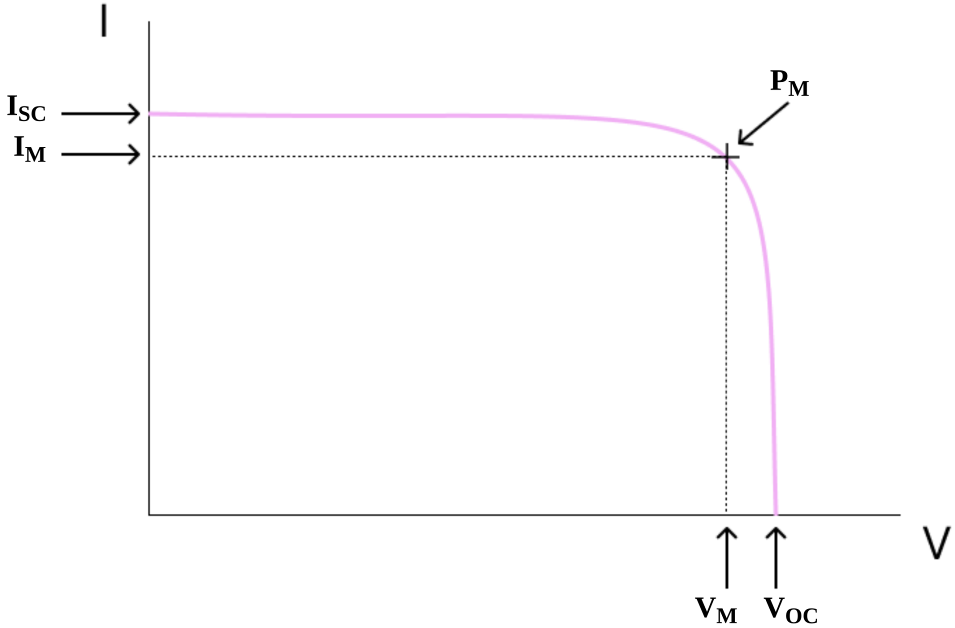

Figure 2.1: IV curve of a photovoltaic device. The main points I_{SC}, V_{OC}, P_M, V_M and I_M are highlighted.

This work was carried out using Silvaco Atlas Software[44], a TCAD simulator able to provide realistic and trustable results when modeling a wide variety of electronic devices, including photovoltaic solar cells. The Poisson and continuity equations are solved to obtain the main properties and characteristics of each device configuration.

2.1 TCAD models and material parameters

This section shows a detailed description of the models used in the TCAD simulations and the main material parameters for SiC polytypes and GaAs.

Table 2.1 shows significant material parameters used in the simulations for the three SiC polytypes and GaAs, being these the energy bandgap, the illumination wavelength, the thermal conductivity and the effective conduction and valence bands *Density Of States* (DOS). The

USC UNIVERSIDADE DE SANTIAGO DE COMPOSTELA

Table 2.1: Material parameters for 3C-SiC, 4H-SiC, 6H-SiC and GaAs included in the simulation framework. The bandgap[45] [REF FALTA GaAs], incident wavelength (λ), thermal conductivity (κ)[46][REF FALTA GaAs] and effective densities of states in the conduction/valence bands(N_C/N_V) [44][REF FALTA GaAs], are shown.

	3C-SiC	4H-SiC	6H-SiC	GaAs
Bandgap [eV]	2.36	3.23	3.02	1.42
λ [nm]	525	366	400	837
κ [W m^{-1} K^{-1}]	500	350	320	50
N_C [cm^{-3}]	6.5e18	1.7e19	7.7e18	4.7e17
N_V [cm^{-3}]	1.7e18	3.3e19	4.7e18	7.0e18

effective DOS are higher in the 4H-SiC than in the 3C-SiC and 6H-SiC, both in the conduction and valence bands[44]. The higher bandgap energy of the 4H-SiC (3.23 eV) makes it a sound candidate for LPC base material. The 6H-SiC also has a high bandgap of 3.02 eV. The 3C-SiC has the lowest bandgap energy of the proposed SiC polytypes (2.36 eV). However, the thermal conductivity is higher for the 3C-SiC (500 W m^{-1} K^{-1}) than for the 4H-SiC and 6H-SiC (350 and 320 W m^{-1} K^{-1}, respectively). This could position the 3C-SiC as the preferred choice for LPC base material in extreme conditions, making it better suited for space applications. Note that both the bandgap energy and thermal conductivity of GaAs, the current state-of-the-art material, are significantly lower than those of the SiC polytypes. Since the indirect bandgap of the SiC polytypes implies a low optical absorption, the incident wavelengths for these materials are chosen to guarantee an extinction coefficient of at least k = 2 × 10 $^{-4}$. This value was established after a preliminary analysis to maximize the light absorption without compromising the efficiency of the device due to the minority carrier diffusion length.

To realistically emulate the behavior of SiC, we use the Caughey-Thomas model to describe carrier mobilities with doping density dependence[47], a suitable model when a low electrical field is accounted[48]. Carrier mobility (μ) is expressed as:

$$\mu = \mu_{min} + \frac{\mu_{max} - \mu_{min}}{1 + (N/N_{ref})^{\alpha}} \tag{2.3}$$

where μ_{max} and μ_{min} are the mobilities of pure and high doped crystal respectively, N the doping level, N_{ref} the doping level at which the mobility is in an intermediate value between μ_{max} and μ_{min} and α a fitting parameter. Table 2.2 shows the mobility parameters used in this work. However, in the case of GaAs, the doping-dependant mobilities are internally calculated by Silvaco from data extracted from reliable experimental sources.

USC UNIVERSIDADE DE SANTIAGO DE COMPOSTELA

Table 2.2: Caughey-Thomas mobility parameters for 3C-SiC, 4H-SiC and 6H-SiC. The GaAs doping-dependant mobilities are implemented through a Silvaco internal data taken from empirical measurements. The μ_{max} and μ_{min} GaAs values shown correspond to doping values of 1e14 cm^{-3} and 1e20 cm^{-3}, respectively.

		3C-SiC		4H-SiC		6H-SiC		GaAs	
		e$^-$	h$^+$	e$^-$	h$^+$	e$^-$	h$^+$	e$^-$	h$^+$
μ_{max}	[cm^2/Vs]	900	70	950	125	420	95	8000	390
μ_{min}	[cm^2/Vs]	40	15	40	16	30	25	1200	61
N_{ref}	[cm^{-3}]	1.5e17	5.0e19	1.94e17	1.76e19	6.0e17	5.0e18	-	-
α	-	0.80	0.30	0.61	0.34	0.80	0.40	-	-

The main recombination mechanisms in the bulk of single-crystal semiconductors are divided into radiative and non-radiative recombinations, being the last ones the defect assisted recombinations (or *Shockley–Read–Hall* (SRH) recombinations) and the Auger recombinations. The radiative recombination takes place when an electron loses energy on the order of the band gap and moves from the conduction band to the valence band. This process is the inverse from the optical generation, where an electron gets promoted from the valence band to the conduction band due to photon absorption. The recombination mechanism is modeled as:

$$R_{np}^{OPT} = C_{OPT} \cdot np \tag{2.4}$$

Where R_{np}^{OPT} is the radiative recombination rate, n and p the electron and hole concentrations and C_{OPT} a parameter characteristic of each material. Since the contribution of radiative recombination has no relevance for indirect bandgap materials, it has not been included in the simulations of SiC polytypes. However, this recombination mechanism is considered in the case of GaAs, because it is a direct bandgap semiconductor.

SRH recombination is considered the main recombination process in indirect bandgap semiconductors[49]. The SRH recombination rate (R_{net}^{SRH}) with doping dependence is expressed as follows:

$$R_{net}^{SRH} = \frac{np - n_i^2}{\tau_p \left(n + n_i \cdot exp\frac{E_{trap}}{k_B T_L}\right) + \tau_n \left(p + n_i \cdot exp\frac{-E_{trap}}{k_B T_L}\right)} \tag{2.5}$$

where:

USC UNIVERSIDADE DE SANTIAGO DE COMPOSTELA

$$\tau_{n,p} = \frac{\tau_0}{1 + \left(\frac{N}{N_{norm}}\right)^{\gamma}}$$

being n_i the intrinsic carrier concentration, which is negligible for SiC at room temperature[48], E_{trap} the difference between the trap energy level and the intrinsic Fermi level, k_B the Boltzmann constant, T_L the lattice temperature, $\tau_{n,p}$ the effective electrons and holes lifetimes, τ_0 the longest lifetime observed in undoped crystal, N the doping concentration, N_{norm} a doping concentration which operates as a normalization constant and γ a fitting parameter[50, 51]. We use $E_{trap} = 0$, which corresponds to the most efficient recombination centers[44].

The Auger recombination rate (R_{Auger}) is determined by the following expression:

$$R_{Auger} = C_n(pn^2 - nn_i^2) + C_p(np^2 - pn_i^2) \tag{2.6}$$

where C_n and C_p are Auger experimental coefficients for a given material[52]. Table 2.3 shows the set of recombination parameters used in this work. A remarkable characteristic of 3C-SiC is its small Auger coefficient, an order of magnitude lower than that of 4H-SiC[53, 54], two orders of magnitude lower than that of GaAs[55] and three orders of magnitude lower than that of the 6H-SiC[56]. This is beneficial at high injection levels, when this recombination mechanism is predominant[57].

In the case of SiC polytypes, the Lindefelt bandgap narrowing model was implemented. This model was specifically developed to account for the doping-induced bandgap narrowing in the most common SiC polytypes[58]. The beam-device interaction is modeled with the ray tracing method[44]. This study is conducted at a constant temperature of 298 K, which is the standard in the photovoltaic field. Note that, to ensure the success of this technology, it will be necessary to examine how the temperature changes with increasing laser power densities and its impact on the device performance, considering relevant factors, such as efficiency, surface area, and thermal resistance. However, there are available mechanisms to manage heat waste, for instance the use of simple passive solutions based on a flat plate, already implemented in ultra-high CPV systems at concentrations up to 10,000 suns (1 kW cm^{-2})[59]. Also, note that the proposed LPCs are expected to have very high efficiencies, which means that only a small fraction of the incident beam not converted into electric power will be transformed into heat.

USC UNIVERSIDADE DE SANTIAGO DE COMPOSTELA

Table 2.3: Fitting parameters for 3C-SiC, 4H-SiC, 6H-SiC and GaAs, for the recombination models SRH, Auger and optical.

Model	Parameter	3C-SiC		4H-SiC		6H-SiC		GaAs	
		e$^-$	h$^+$	e$^-$	h$^+$	e$^-$	h$^+$	e$^-$	h$^+$
SRH	N_{norm} [cm^{-3}]	1.0e17	1.0e17	3.0e17	3.0e17	3.0e17	3.0e17	2.7e13	2.7e13
	γ [-]	0.3	0.3	0.3	0.3	0.3	0.3	1	1
	$\tau_0[\mu s]$	11.0	2.2	107	21.4	17.0	3.4	150	80
Auger	C_{Auger} [cm^6/s]	3e-32	2e-32	5e-31	2e-31	3e-29	3e-29	5e-30	1e-31
Optical	C_{OPT} [cm^3/s]	-	-	-	-	-	-	1.5e-10	1.5e-10

2.2 Devices

This section presentes the different LPC device structures used in this work, namely the hLPC, the vLPC and the VEHSA, and its characteristics. All the studied devices have the same single unit structure, four layers with n+/n/p/p+ doping types. In these modeled devices the third dimension (depth) does not affect the carrier transport and density, and it is set to 1 μm without loss of generality in order to save computational costs. The depth of the devices is only limited by fabrication issues and as some of SiC processes are very similar to those of the Si, which are well known and commonly industrialized. We apply total transmittance for the incident light in the illumination area, emulating the behavior of an antireflective coating, which is a realistic approximation because these devices are illuminated with only one wavelength.

The most common device structure in this technology is the hLPC (see a scheme in Figure 2.2a). Indeed, the current state-of-the-art is a GaAs based hLPC, which achieves a 68.9% efficiency at a laser power density of 11.4 W cm^{-2} and experiences efficiency degradation at higher laser power densities due to ohmic losses[17]. In the hLPC the incident light is parallel to the current flow and perpendicular to the anode and cathode. In this architecture, there is a trade-off between the optical path and the carrier diffusion length, as the absorption and transport processes take place in the same direction. In indirect bandgap semiconductor-based devices, where the photon absorption is lower than in direct semiconductors[60], a textured reflective layer is used to increase the optical path, greatly enhancing light absorption and photon recycling[61]. This mechanism avoids an excessively long device in which the minority carriers will not survive. In the hLPC devices modeled in this work, this layer is placed at the bottom of the device. Since there are several technological solutions to minimize the effect of surface recombination, e.g. using passivation layers[62], and considering that the generation and transport processes occur in the vertical direction, the width of the devices

USC UNIVERSIDADE DE SANTIAGO DE COMPOSTELA

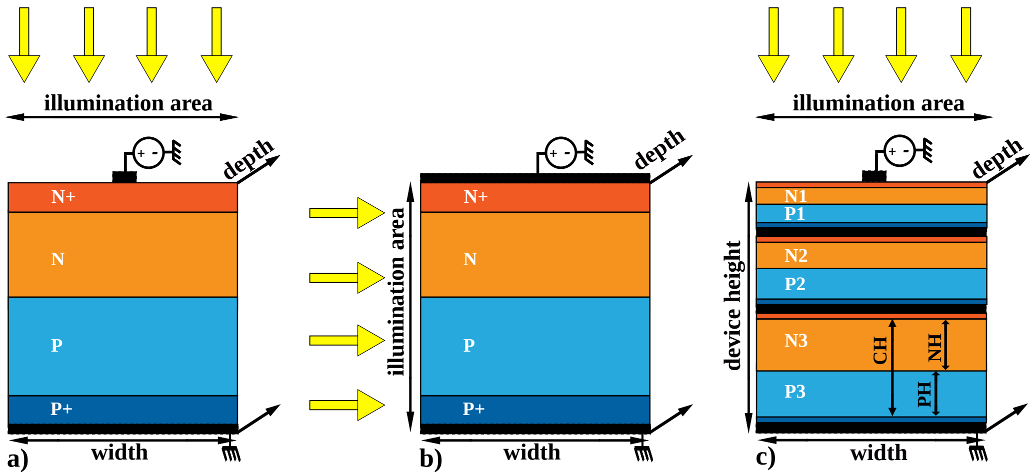

Figure 2.2: The three device structures used in this work, the a) hLPC, b) vLPC and c) a VEHSA with 3 cells.

is set to 10 μm to save computational costs. The cathode is placed at the top of the device, covering a 3% of the illumination area, while the anode is placed along the bottom of the device.

To overcome the limitation of ohmic losses at high laser power densities, Outes et al.[19] proposed a new device structure through numerical simulations, a GaAs-based vLPC which achieve efficiencies of more than 76% at 3000 W cm^{-2}, see a scheme in Figure 2.2b. The benefits of this architecture are no shadowing effects from the front metal grid and a drastic reduction of series resistance ($\approx 10^{-5}$ Ω cm^{-2})[63, 64, 20]. In the vLPC, the incident light is perpendicular to the current flow and parallel to the anode and cathode. As in the vertical architecture there is no trade-off between photon absorption and carrier transport, the width of the device is independent of illumination and is adjusted for optimal absorption. Another interesting feature is the possibility to connect several devices via tunnel junctions to increase the illumination area[63]. This could be achieved by monolithically growing multiple subcells on the top of each other, as in standard multijunction concentrator solar cells. In this sense, the viability of stacking up to 30 p/n junctions has already been proven[22, 65]. Another method to increase the illumination area is via the arrangement of a multisegment series connection[66].

Other particularly noteworthy device structure is the VEHSA architecture, which stands out among the multijunction LPCs. This arrangement consists of monolithically stacking p/n

USC UNIVERSIDADE DE SANTIAGO DE COMPOSTELA

tunnel junctions[16] (see an example of a 3-cell VEHSA in Figure 2.2c), which is also the main pathway to achieve ultra-high efficiencies on concentrating photovoltaic solar cells[23]. The major advantage of this architecture is the ability to distribute the current over the p/n junctions, which reduces Joule heating losses. This allows to operate under high laser power concentrations, increasing the efficiency due to the V_{OC} enhancement associated with higher carrier concentration. The V_{OC} also benefits from a greater Fermi level splitting in thin layers[24]. The current record efficiency for a GaAs-based VEHSA is 66.3% and has been achieved with a 5-cell device at 150 W cm^{-2}[16]. In this work, authors also explored VEHSAs with up to 20 cells to try to handle even larger input powers. However, when the number of cells was increased the effect of current mismatching also incremented, due to intrinsic fabrication issues, deteriorating the efficiency. The optimization of VEHSA devices is challenging because of the extreme difficulty of evaluating its individual cell currents.

2.3 Optimization

In this section we present the in-house-built optimization algorithms developed in this work. First, a single cell iterative algorithm is presented. After that, the main limitations in the design of state-of-the-art VEHSA devices are described. These limitations are next addressed with an in-house built optimization algorithm called PhPO to improve the performance of VEHSA devices via a meticulous current matching and the improvement of the individual efficiency of each cell.

To optimize single cell devices like the hLPC and vLPC, composed of four layer structures with n+/n/p/p+ doping types (see Figures 2.2a and 2.2b), an iterative algorithm is developed. The aim is to ensure that the best design parameters that maximize the efficiency are used for each laser power density. The target design parameters are the n and p layer thicknesses and doping values. The n+ and p+ layer thicknesses and doping values are previously optimized and fixed. The optimization algorithm for a single design parameter is described in Figure 2.3. The parameters are swept from an initial value (provided by a preliminary single cell optimization), one by one, with the scope of increasing the cell efficiency. If new optimum design parameters are found, a new iteration is needed, since these optimizations can change the current contributed by each cell and the currents need to be matched again. On the other hand, if during the whole cell optimization cycle no new design parameters are found, the process stops, and it is considered that all cells have achieved their maximum efficiency.

USC UNIVERSIDADE DE SANTIAGO DE COMPOSTELA

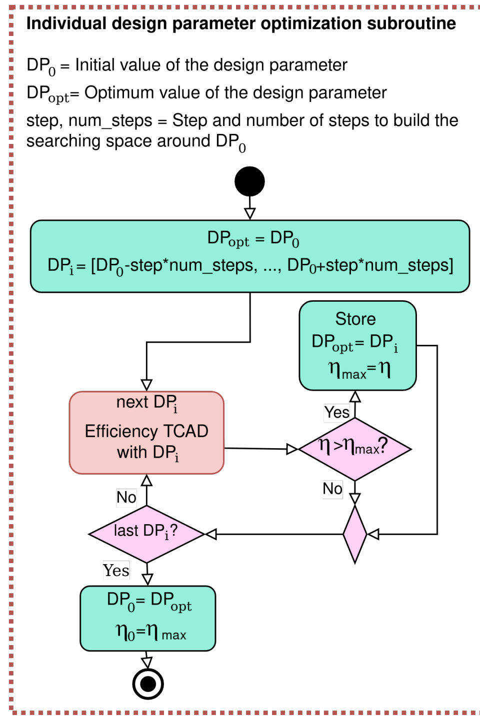

Figure 2.3: Detailed optimization of each design parameter. Efficiency TCAD is the simulation aimed to obtain the efficiency of the evaluated cell. η_0 , η, and η_{max} are the initial, latest simulated and maximum efficiencies of the evaluated cell, respectively.

The iterative algorithm works for single-cell devices. However, the multijunction LPCs require more steps to optimize the design parameters. In the VEHSA architecture, a key factor that affects the performance of the devices is the precise matching of the currents produced by every cell, since the total current drawn from the device will be the lowest of all the contributing cells. Up to date, the state- of-the-art VEHSA devices achieve current matching by applying the Beer-Lambert law, the exponential light decay[25]. The integrated photogeneration must be the same in all cells.

$$I_{i+1}(\lambda) = I_i e^{-\alpha(\lambda)t_i} \tag{2.7}$$

where I_i and I_{i+1} are the light intensities entering and leaving the i-th layer, respectively, t_i is

USC UNIVERSIDADE DE SANTIAGO DE COMPOSTELA

the thickness of the i-th layer and $\alpha(\lambda)$ the wavelength dependent absorption coefficient. This is a good approximation for direct-gap VEHSA devices, as the photogeneration can be calculated very accurately. However, this method does not take into account the performance of each cell, so there will be differences between the photogenerated current and the total current contributed. To avoid this issue, it has been proposed to consider the *Quantum Efficiency* (QE) of each cell to calculate the current supplied[27] as follows:

$$I_{abs} = \int \frac{dI_{avail}}{d\lambda} \cdot QE(\lambda) \cdot (1 - T(\lambda) - R(\lambda))d\lambda \tag{2.8}$$

where I_{abs} and I_{avail} are the absorbed and available photocurrents, R the reflectance, and T the transmittance. This has the advantage of considering beam reflection and transmission, and recombination effects, which are implicit in QE. However, it misses relevant effects such as photon recycling, which is shown to be important in the modeling of GaAs VEHSA devices[67]. These approaches generally provide good results, but the performance worsens as the number of cells increases, due to the current mismatch. The actual record efficiency for a VEHSA at room temperature is achieved by a 5-cell device, reaching a 66.3%[16], and the efficiency consistently decreases for a larger number of cells. Another disadvantage of these approximations is that they are not applicable to indirect bandgap devices that require back texturization for light trapping.

We present an optimization method aimed to overcome these issues valid for both direct or indirect bandgap VEHSA devices, independently if they are powered by a laser or by solar light. The system consists of meticulous device TCAD of the VEHSA device combined with an iterative optimization algorithm. As modeling tunnel junctions in Silvaco can be problematic[68], we used an standard workaround that consist of modeling the tunnel junctions as perfect conductors[69], to speed-up the simulation time. In these so modeled tunnel junctions we allow the extraction of the tunnel junction currents (TJCs), coupling them to electrodes with lumped variable resistances, as seen in Figure 2.4. These resistances can take very high values to simulate the full device, to avoid current through these contacts, or low realistic values to obtain the differences between the currents produced in adjacent cells. This is a useful tool to accurately match the currents of all cells and improve the performance of the full VEHSA device.

The optimization algorithm is an iterative process involving two stages: Photogeneration and Performance Optimization, as shown in Figure 2.5. In the first step, the photogeneration loop, the total device height (DH) is optimized to absorb the largest part of the beam without

USC UNIVERSIDADE DE SANTIAGO DE COMPOSTELA

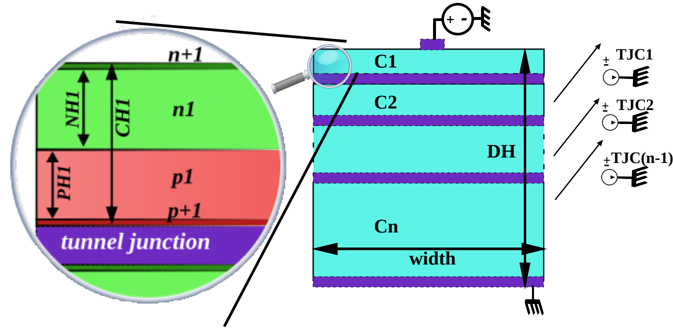

Figure 2.4: 2D-Schematic of a VEHSA device. The variable resistances in tunnel junctions allow to extract the current diferences from the adjacent cells. C1, C2, . . . , Cn are the cells of the VEHSA device. The zoom-in shows the detailed structure of the cell C1, composed by n+/n/p/p+ layers, with a CH1 total height. PH1 and NH1 are the heights of C1 p and n layers, respectively.

unnecessarily increasing the size of the device, which will affect the carrier transport. As a first approach the Beer-Lambert law is used to obtain an initial guess. The algorithm iterates, by increasing/decreasing the DH, until two criteria are fulfilled: i) a minimum absorbed light value (photo_low), that establishes the maximum photogeneration losses allowed of the total incident light and ii) a maximum photogeneration value (photo_high), which prevents the device from growing infinitely to absorb the totality of the photons. The resulting optimum DH is then used as an input for the next stage, the performance loop. In this second stage, the optimizer improves the performance of the cells individually. This process begins with a subroutine that iteratively evaluates the TJCs and modifies CH1,. . . , CHn, i.e. the relative sizes of each cell (see Fig' s 2.4 zoom-in). As the TJCs extracted are the differences between the currents of the adjacent cells, the absolute value represents their mismatch, and the sign of the current indicates which cell is limiting the performance. A negative/positive sign means that the bottom/top cell is limiting and the algorithm modifies the values of CH1, . . . , CHn to increase the limiting cells in steps normalized by the largest absolute TJC value of all tunnel junctions. This process iterates until all TJCs contribute with the same current and the value is below a certain tolerance, e.g., 1/1000 of the I_{SC} extracted in the anode. When this is achieved,

USC UNIVERSIDADE DE SANTIAGO DE COMPOSTELA

the algorithm optimizes the design parameters, which are the layer relative sizes (PHi, NHi) and doping values (PDi, NPi) for every i-th cell, from 1 to n. The optimization algorithm for a single design parameter is the same as in the single cell iterative routine, described in Figure 2.3.

USC UNIVERSIDADE DE SANTIAGO DE COMPOSTELA

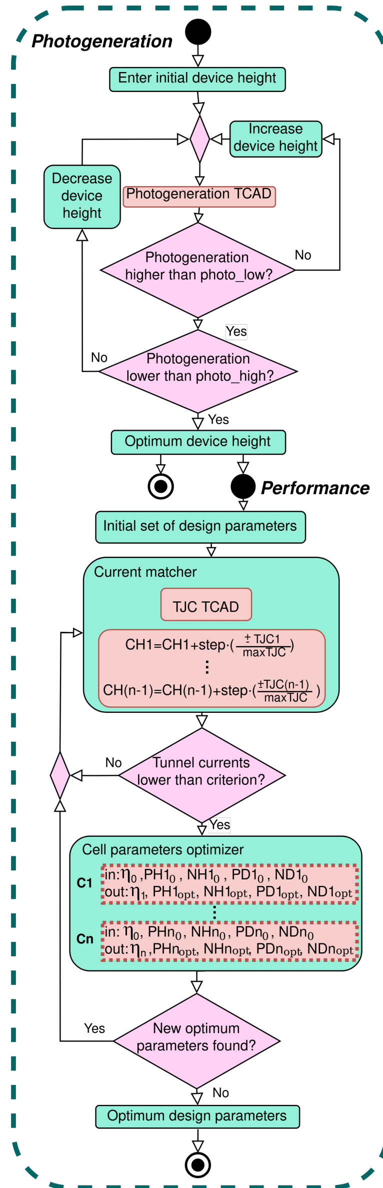

Figure 2.5: Flowchart of the different stages of the PhPO method. Photogeneration TCAD and TJC TCAD are simulations aimed to obtain the photogeneration of each cell and the currents extracted in the tunnel junctions (TJC), respectively. The optimum device height is fixed in the photogeneration loop and used as an input to the performance loop.

USC UNIVERSIDADE DE SANTIAGO DE COMPOSTELA

Chapter 3

Discussion

This thesis is focused on enhancing the efficiency of the *Laser Power Converter* (LPC) technology. Two routes are explored for this purpose: 1) The introduction of high bandgap materials to reduce both intrinsic entropic losses[31, 29] and series resistance losses, since, for a given laser power density, the beam will have a shorter wavelength than a laser feeding a low bandgap material, which implyes less photons with more energy, and 2) The introduction of advanced device architectures as the *vertical Laser Power Converters* (vLPC) and *Vertical Epitaxial Hetero-Structure Architecture* (VEHSA) to further reduce the effect of series resistance losses.

The first route will be addressed in subsection 3.1, where the feasibility of three *Silicon Carbide* (SiC) polytypes as base material for LPCs will be discussed. These polytypes are the *Cubic Silicon Carbide* (3C-SiC), *Hexagonal 4H Silicon Carbide* (4H-SiC) and *Hexagonal 6H Silicon Carbide* (6H-SiC), with bandgap energies of 2.36, 3.23 and 3.02 eV, respectively. The properties of those materials are detailed in section 2.1. These three semiconductors are implemented in the most common device configuration, the *horizontal Laser Power Converter* (hLPC). Once the best performance SiC polytype is stablished, we perform resilience tests varying the temperature and the laser power density.

The VEHSA architecture, which consists of a multijunction device with monolithically stacked cells connected by tunnel junctions, is designed to reduce the series resistance losses by splitting the current among the cells. The optimization of such devices is difficult, since the current that each cell provides must be the same. Currently, the use of the VEHSA architecture is mostly limited to *Gallium Arsenide* (GaAs) and other III-V direct bandgap materials. Subsection 3.2 covers the results of the *Photogeneration and Performance Optimization* (PhPO),

USC UNIVERSIDADE DE SANTIAGO DE COMPOSTELA

which is an in-house built algorithm suitable to optimize VEHSA devices, for both direct or indirect bandgap materials (as SiC polytypes). This algorithm is tested on a VEHSA state-of-the-art LPC[16]. Once the experimental device has been accurately modeled via *Technology Computer Aided Design* (TCAD), the PhPO optimizes all the design parameters to achieve the best performance, both from each individual cell and from the entire device.

Finally, after the best performance polytype has been stablished and the suitability of the PhPO to optimize VEHSA devices has been proved, in subsection 3.3 the high bandgap materials are implemented in two advanced architectures: the vLPC and the VEHSA. These devices are optimized to find the best desing parameters and tested to identify possible trade-offs of this technology. Finally, a comparative with the state-of-the-art is presented.

3.1 Comparative of three SiC polytypes

In this section we evaluate the feasibility of three SiC polytypes (3C, 4H and 6H) as base material for LPCs. We performed optimizations under several input power densities using the conventional horizontal architecture (hLPC).

Table 3.1 shows the optimum design parameters of the hLPCs made of the three polytypes. At an input power density of 1 W cm^{-2} the optimum thicknesses of the N/P layers for the three polytypes are identical, 14 μm for the N layer and 69 μm for the P layer, which produces a total height of the devices of 83 μm. For the 3C and 4H SiC devices these optimum thicknesses do not change at 100 W cm^{-2}, while in the 6H device the total thickness reduces to 62 μm with a 22/40 μm for the N/P layers respectively. This reduction is due to the impact of Auger recombination, which severely degrades the performance in the 6H devices. As seen in Table 2.3, the Auger coefficients for the 6H are 2 and 3 orders of magnitude larger than the 4H and 3C coefficients, respectively. Decreasing the total height reduces the total amount of photogenerated carriers and thus the Auger recombination, at the cost of reducing the amount of absorbed photons. For this reason, at 1000 W cm^{-2} the 3C, 4H and 6H device total heights reduce to 75 μm, 65 μm, and 38 μm, respectively. The optimum doping values in the P layer consistently increase with a rise in *Input power density* (P_{in}): ranging from 1 to 1000 W cm^{-2}, the 4H acceptor concentrations increase two orders of magnitude, from 1e15 to 3e17 cm^{-3}, while the 3C and 6H increase around one order of magnitude, from 7e16 to 1e18 cm^{-3} and from 1e16 to 1e17 cm^{-3}, respectively. However, the optimum donor concentration in the 3C and 4H devices remains constant at 1e15 cm^{-3} for all input power densities. In the 6H-SiC,

USC UNIVERSIDADE DE SANTIAGO DE COMPOSTELA

Table 3.1: Optimum design parameters of 3C, 4H and 6H SiC hLPCs at laser power densities (P_{in}) of 1, 100 and 1000 W cm^{-2}. The thicknesses and doping values of the P and N layers are shown.

	Layer	3C			4H			6H		
P_{in} [W cm^{-2}]		1	100	1000	1	100	1000	1	100	1000
Thickness [μm]	N	14	14	14	14	14	12	14	22	8
	P	69	69	61	69	69	53	69	40	30
Doping [cm^{-3}]	N	1e15	1e15	1e15	1e15	1e15	1e15	1e16	1e16	5e16
	P	7e16	3e17	1e18	1e15	5e16	3e17	1e16	5e16	1e17

Table 3.2: Main figures of merit for the three SiC polytypes using the hLPC architecture, being these: Short circuit current density (J_{SC}), open circuit voltage (V_{OC}), the V_{OC} growth with the laser power density (ΔV_{OC}), the fill factor (FF) and efficiency (Eff). Results are shown for input laser power densities (P_{in}) ranging from 1 to 1000 W cm^{-2}.

	Pin	Jsc	Voc	ΔVoc	FF	Eff
	[W cm^{-2}]	[A cm^{-2}]	[V]	[V]	[%]	[%]
3C	1	0.390	2.14	-	93.1	78.3
	10	3.95	2.25	0.11	92.9	82.3
	100	39.8	2.30	0.16	92.2	84.6
	1000	385	2.35	0.21	89.1	80.8
4H	1	0.280	2.88	-	94.7	77.5
	10	2.84	2.94	0.06	94.6	78.9
	100	28.4	2.99	0.12	93.6	79.4
	1000	276	3.04	0.16	91.8	77.2
6H	1	0.310	2.70	-	94.4	77.9
	10	3.08	2.74	0.04	93.3	78.9
	100	29.9	2.79	0.09	90.9	75.9
	1000	270	2.84	0.14	84.4	64.7

the optimum N doping value is 1e16cm^{-3}, one order of magnitude higher, except for a P_{in} of 1000 W cm^{-2}, which is 5e16 cm^{-3}.

Table 3.2 shows the main figures of merit that characterize the hLPCs: the *short circuit current density* (J_{SC}), the *open circuit voltage* (V_{OC}), the V_{OC} growth with the laser power density (ΔV_{OC}), which is defined as the difference between the V_{OC} at a given power density and the V_{OC} at 1 W cm^{-2}: $\Delta V_{OC}(P_{in}) = V_{OC}(P_{in}) - V_{OC}(1Wcm^{-2})$, the fill factor (FF) and the device efficiency (Eff). The J_{SC} grows proportionally to the laser power density, showing slight losses at 1000 W cm^{-2}. The 6H experiences a higher J_{SC} decay with the input power due to the reduction of the total height of the device at high laser power densities previously

USC UNIVERSIDADE DE SANTIAGO DE COMPOSTELA

discussed. The V_{OC} also grows with the laser power density, as expected from the classical approximation[70]:

$$V_{OC} = \frac{k_B T}{q} ln \left[\frac{(N_A + \Delta n)\Delta n}{n_i^2} \right] \tag{3.1}$$

where $k_B T/q$ is the thermal voltage, N_A is the doping concentration, Δn is the excess carrier concentration and n_i is the intrinsic carrier concentration. By increasing the laser power density the Δn also increases, leading to a larger V_{OC}. ΔV_{OC} is different for each material, as seen in Table 3.2. Note that the 3C has larger ΔV_{OC} than the 4H. This is due to the higher optimum doping values resulting from the optimization process, and also due to the higher N_C and N_V values of the 4H (see Table 2.1), that are related to the intrinsic carrier concentration, as follows:

$$n_i = \sqrt{N_C N_V} \cdot e^{\frac{-E_g}{2K_B T}} \tag{3.2}$$

where E_g is the bandgap energy. For a given E_g, higher N_C and N_V values increase the intrinsic carrier concentration, decreasing the open circuit voltage as seen in Equation 3.1. The 6H devices, despite having N_C and N_V values similar to those of the 3C, experience less V_{OC} growth than the 3C and 4H devices due to the Auger recombination. The *fill factor* (FF) exceeds 90% for the three polytypes at all laser power densities except for 1000 W cm^{-2} due to the series resistance losses. These high FF values are due to the large bandgap of the polytypes, which reduce the ohmic losses.

The efficiency of these devices is also shown in Table 3.2. Theoretically, it is expected that the larger the bandgap, the larger the efficiency of the LPCs, as indicated in[29], if no other material properties are taken into account. However, at a P_{in} value of 1 W cm^{-2} the three hLPCs obtain nearly the same efficiency, around ≈ 78%. This is due to to losses related to the light absorption. To ensure an adequate photogeneration inside the devices without greatly increase their height, we chose incident wavelengths for each material that guarantee an extinction coefficient of at least k = 2e-4. This value was established after a preliminary analysis to maximize the light absorption without compromising the efficiency of the device due to the minority carrier diffusion length. These wavelength values can be seen in Table 2.1. The difference between the energy of the monochromatic incident light and the energy gap of the material produces different efficiency losses. The 3C loses an efficiency of 1%, the 6H a 2.5% and the 4H a 5%. However, note that this assumption does not affect the trend of efficiency versus input power density.

USC UNIVERSIDADE DE SANTIAGO DE COMPOSTELA

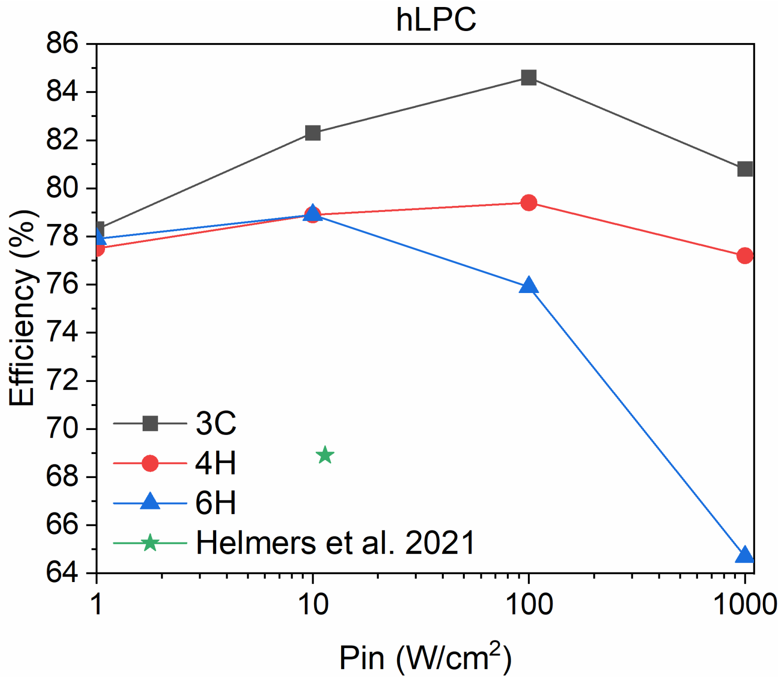

Figure 3.1: Efficiency versus input power density (P_{in}) for the three SiC polytypes using the hLPC architecture. The best performance experimental GaAs-hLPC is included for comparison[17].

As the laser power density increases, the efficiencies of the 3C hLPCs increase more than those of the two other polytypes, reaching a 82.3% efficiency at 10 W cm^{-2}, which is a 3.4% higher than those of 4H and 6H. For comparison, the current best performance experimental GaAs-hLPC achieves a 68.9% efficiency at 11.4 W cm^{-2}[17], which is 13.4% lower than the proposed 3C-SiC hLPC (note that this device has not been fabricated yet, so the performance may be impacted by manufacturing issues). The 3C-SiC hLPC efficiency keeps increasing with the laser power density, achieving a 84.6% at 100 W cm^{-2}. In the case of the 4H, the higher N_C and N_V values limit the growth of the V_{OC} with the laser power density, limiting the efficiency of the 4H hLPCs to a 79.4% at 100 W cm^{-2}. The 6H SiC devices reach a 78.9% efficiency at 10 W cm^{-2} and experience a quick performance degradation to 75.9% at 100 W cm^{-2} due to Auger recombination. At an input power density of 1000 W cm^{-2}, independently of the polytype, the SiC hLPCs reduce their performance due to series resistance losses and

USC UNIVERSIDADE DE SANTIAGO DE COMPOSTELA

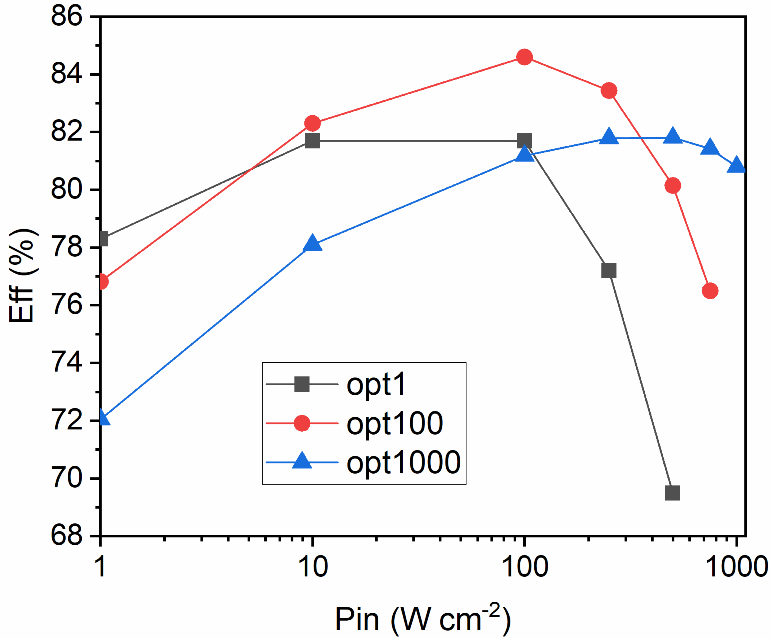

Figure 3.2: Efficiency versus input power density (P_{in}) for the 3C-SiC hLPCs optimized at 1 W cm^{-2} (opt1), 100 W cm^{-2}(opt100), and 1000 W cm^{-2} (opt1000).

Auger recombination, to efficiency values of 80.8%, 77.2% and 64.7% for the 3C, 4H and 6H SiC hLPC s, respectively. These efficiency values are also shown in Figure 3.1, where it is clear that 3C outperforms the other polytypes for the hLPC architecture.

To evaluate the performance stability with the laser power density of the optimized devices, we chose three 3C-SiC hLPCs, optimized at 1 W cm^{-2} (opt1), 100 W cm^{-2} (opt100), and 1000 W cm^{-2} (opt1000), and tested them under different P_{in} values. Their resulting efficiency values are shown in Figure 3.2. Note that the main difference in the design parameters of these devices is the P-layer doping value, which is increased from 7e16 cm^{-3} in opt1 to 1e18 cm^{-3} in opt1000 (see Table 3.1). As expected, the best performance device for each laser power density is the one that has been optimized for that particular power. At 1 W cm^{-2}, opt1 achieves an efficiency 1.5% higher than the opt100 and 6.25% higher than the opt1000. However, as the laser power density increases, the opt1 performance worsens compared to opt100, which outperforms op1 by 2.9% and opt1000 by 3.4% at 100 W cm^{-2}. At higher laser power densities, both opt1 and

USC UNIVERSIDADE DE SANTIAGO DE COMPOSTELA

opt100 experience efficiency degradation, loosing at 500 W cm^{-2} a 12.2% efficiency for the opt1 and a 4.5% for the opt100 with respect to the efficiencies achieved at 100 W cm^{-2}. The opt1000 reaches maximum efficiency of 81.81% at 500 W cm^{-2}, and manages to convert a laser power density of 1000 W cm^{-2} with only a 1% efficiency decay. It is noteworthy that by increasing the doping concentration in the P-layer greater performance stability at high P_{in} values is achieved, but limits efficiency at lower laser power densities. These results highlight the need to optimize the device structures according to the targeted laser power density, which will depend on the application of the technology.

To analyze the effect of temperature on the proposed devices, Figure 3.3 compares the efficiency of the 3C, 4H and 6H hLPC s versus the temperature (at 25, 50, 100 and 150 ºC). This study has been done at a Pin of 1000 W cm^{-2}, which is the highest laser power density tested for these hLPC s, and therefore, the most likely to suffer from heating problems. The efficiency degradation due to heating is more severe in 6H hLPC , which loses a 16.5% efficiency when the temperature is increased to 150 ºC, whereas the 4H loses a 10.2% and the 3C only loses a 4.7%, which makes the 3C-based hLPC s the most temperature-resilient. These results suggest that the effect of temperature might not be a critical point in the viability of the proposed technology.

3.2 Optimization of VEHSA devices using the PhPO algorithm

In this section we validate our TCAD methodology against an experimental VEHSA state-of-the-art device and test our algorithm to optimize LPC multijunction devices. The PhPO finds the most suitable design parameters to enhance the performance of each individual cell and also to reduce the current mismatch between cells, which is a common issue when manufacturing VEHSA devices and the main limitation to greatly extent the number of cells.

To validate our methodology we initially model a GaAs-based 5-cell VEHSA (VEHSA PT5 from now on), that is designed after the experimental device reported by Fafard et al[16], that currently holds the record breaking efficiency at room temperature. The absorption coefficient used depends on both the doping concentration and the wavelength, and fits experimental curves[71]. The material physical parameters, the incident power and the illumination area are taken from the experimental device supporting information[16]. The width of the device (see Figure 2.2) is fixed to 10 µm to save computational costs. Since the generation and transport processes occur in the vertical direction and no surface recombination is accounted in this work,

USC UNIVERSIDADE DE SANTIAGO DE COMPOSTELA

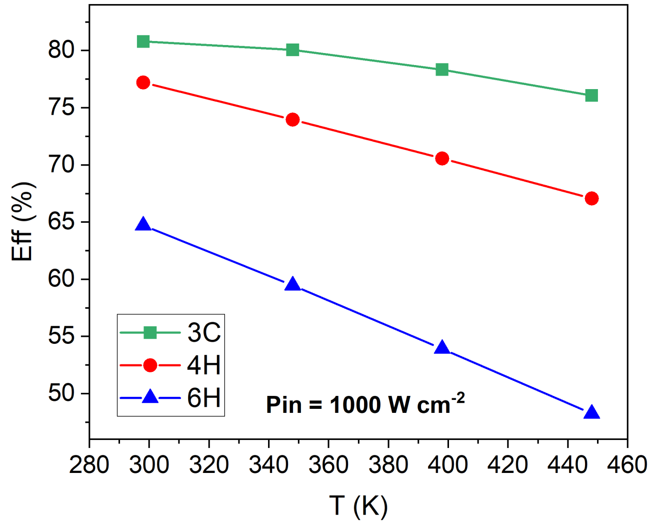

Figure 3.3: Efficiency versus temperature for the three hLPC-SiC polytypes optimized at 1000 W cm^{-2}.

which avoids perimeter recombination sources, this decision will not affect the behavior of the device. Given that no specific design parameters are provided for this particular experimental device, the cell heights (CH) were obtained by applying the Beer-Lambert law[25]. As the light penetrates the device, the CH values increase due to the photogeneration decay in the device. The CH for each cell includes the n+/n/p/p+ layers as follows: $CH = h_{np+} + h_{np}$, where h_{np+} is the sum of the p+/n+ layers heights and h_{np} the sum of the n/p layer heights. The p+/n+ layers have fixed heights and doping values of 0.02 µm and $5{\cdot}10^{19}$ cm^{-3}, respectively, selected to accurately match the experimental characteristics. The n/p relative layer heights (NH/PH) are shown as a percent of h_{np} (e.g. n layer height=NH$\cdot$ h_{np}), since this value is fixed by the CH and h_{np+}. The NH/PH values are considered to be equal (0.50/0.50)[16], and the doping values (ND/PD) range from $5{\cdot}10^{17}$-$1.0{\cdot}10^{18}$ cm^{-3}, with thinner cells more heavily doped[27]. The illumination wavelength is fixed to 837 nm as in the experimental device. These initial parameters at room temperature are shown in Table 3.3. Figure 3.4 shows a comparison between the experimental and the initial calibrated VEHSA PT5 IV curves. Note that in this figure the simulation results are scaled to the illumination area of the experimental

USC UNIVERSIDADE DE SANTIAGO DE COMPOSTELA

Table 3.3: Design parameters (DP) for the VEHSA PT5 validation and optimization. DH and CH are the device and cell heights in microns, NH/PH the N/P layer heights in percent and ND/PD the doping values for the N/P layers, respectively. The width is set to 10 μm.

DP	DH [μm]	Cell	CH [μm]	NH [%] / PH [%]	ND [cm^{-3}]	PD [cm^{-3}]
Initial	3.5	1	0.170	0.50/0.50	1e18	1e18
		2	0.218	0.50/0.50	1e18	1e18
		3	0.303	0.50/0.50	1e18	1e18
		4	0.503	0.50/0.50	1e18	1e18
		5	2.306	0.50/0.50	5e17	5e17
Optimized	3.7	1	0.175	0.90/0.10	1e15	1e15
		2	0.227	0.90/0.10	1e15	1e15
		3	0.317	0.60/0.40	1e15	1e15
		4	0.530	0.50/0.50	1e15	1e15
		5	2.450	0.30/0.70	1e15	1e15

device. The device TCAD accurately reproduces the values of Isc and Voc of the experimental device, and the slight differences in the shape of the curve at *voltage at the maximum power point* (V_M) and intermediate voltages may derive from manufacturing issues.

Once we have demonstrated the validity of our simulation methodology, we apply the PhPO method to further improve the device performance, see in Table 3.3 the optimized design parameters. The DH slightly increases with respect to the calibration, reaching 3.7 µm. The cell heights have been fine-tuned until the TJC mismatch is below 1/1000 the Isc value of the anode. The relative NH/PH values return much larger n layer heights for thinner cells (e.g., 0.9/0.1 for the first cell), that gradually decrease as the CH increases (e.g., 0.3/0.7 for the fifth cell). The doping values significantly decrease to $1{\cdot}10^{15}$ cm^{-3}, a value three orders of magnitude lower than those observed in the initial design parameters.

The optimized IV curve is also shown in Figure 3.4 for comparison. The optimized VEHSA PT5 achieves the same Voc as the calibrated and experimental devices and increases the Isc by 6%, leading to a 75.8% efficiency, a value 9.5% larger than that of the experimental VEHSA PT5. These improvements are due to the meticulous current matching and individual cell optimization. This can be more clearly seen in Figure 3.5 and Figure 3.6, that present the IV curves for each individual cell for the calibrated and optimized devices, respectively. Note that the calibrated VEHSA PT5 individual cell IV curves suffer from current mismatch, and there is also a noticeable Voc mismatch. These effects are drastically reduced in the optimized VEHSA PT5, where the IV curves are very similar for all cells.

USC UNIVERSIDADE DE SANTIAGO DE COMPOSTELA

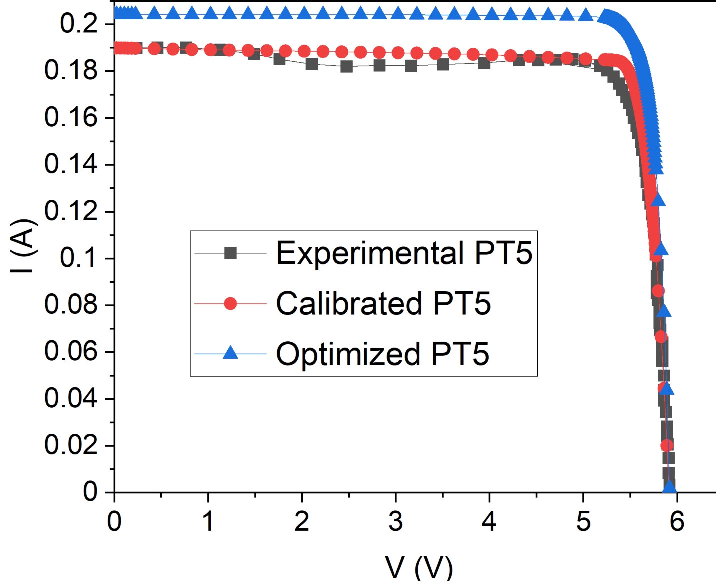

Figure 3.4: IV curves comparing the experimental[16] VEHSA PT5 against the optimized structure provided by the PhPO method. The calibrated VEHSA PT5 is also included as validation.

Given the wide variety of applications for an LPC, both aerial and terrestrial, it is worthwhile to study the impact of temperature on device performance. For that, the calibrated and optimized VEHSA PT5, are tested at three temperatures: the standard laboratory conditions (298 K) and ±75 K with respect to this value (223 K and 373 K), in order to evaluate a wide range of operation. The models[72] used in the course of the simulations take into account the dependence on temperature, namely the universal energy bandgap model, SRH concentration-dependent lifetime model, Fermi statistics and power law temperature dependence mobility.

Figure 3.7 shows the IV curves for the optimized and calibrated VEHSAs PT5. Note that, although both devices reach the same V_{OC} for each temperature (due to bandgap variation), the optimized VEHSA PT5 achieves the same *short circuit current* (I_{SC}) for all three temperatures tested. This is not the case for the calibrated VEHSA PT5, which suffers from loses in I_{SC} at high temperatures. This is due to the existence of higher recombinations in the experimental device, compared to the optimized one. In the calibrated VEHSA PT5, the

USC UNIVERSIDADE DE SANTIAGO DE COMPOSTELA

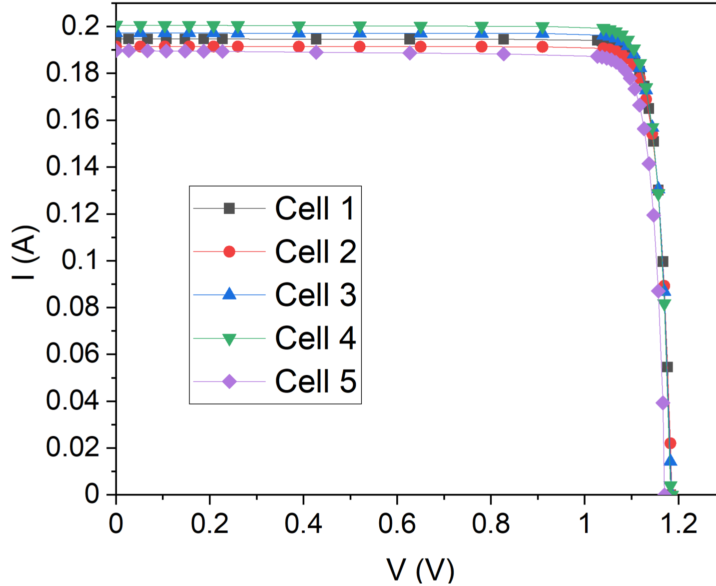

Figure 3.5: IV curves for each cell that composes the calibrated VEHSA PT5. Note that there is an appreciable dispersion in the values of Isc and, to a lesser degree, in those of Voc.

efficiency increases/decreases a 11.3% at 223/373 K with respect to the room temperature values. The efficiency of the optimized VEHSA PT5 is slightly less affected by temperature variations, increasing/decreasing a 10.3% at 223/373 K with respect to the room temperature values, respectively. The design parameters obtained through the PhPO method applied at 298 K have considerably reduced the recombinations of the VEHSA PT5, making the device more resilient to a wide range of temperature. Note that, having a single device capable of operating over a broad temperature spectrum without major losses is desirable to avoid the need to manufacture multiple devices.

3.3 Cubic SiC on advanced LPC devices

Once stablished in section 3.1 that 3C-SiC is the best performance polytype, we implemented this material in advanced architectures such as the vLPC and the VEHSA to further reduce the effect of series resistance losses. Indeed, these device configurations have been developed

USC UNIVERSIDADE DE SANTIAGO DE COMPOSTELA

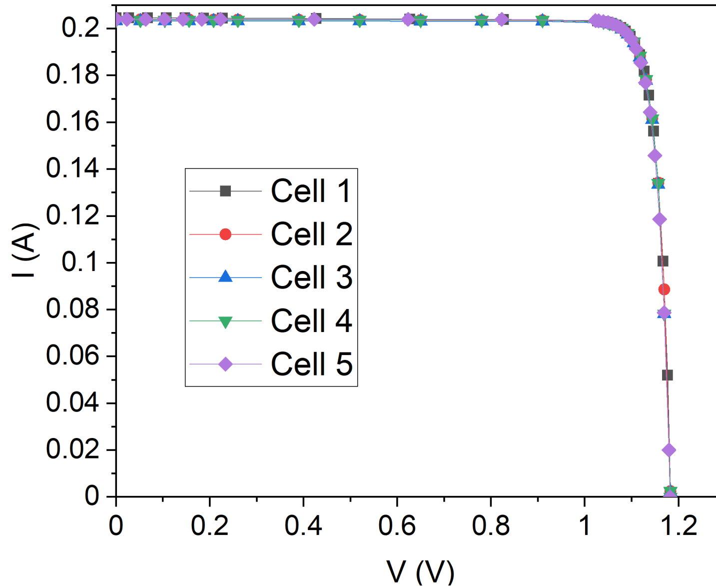

Figure 3.6: IV curves for each cell that composes the optimized VEHSA PT5. Note that, unlike in the case of the calibrated device, there is no dispersion observed in either Isc or Voc.

to mitigate this effect[20, 16], by splitting the total current in the case of the VEHSA and by greatly reducing the effect of the sheet and contact resistances in the vLPC. These devices are expected to overcome the hLPC performance at high laser power densities, where the series resistance has a strong impact in those device performances.

3.3.1 Implementation of 3C-SiC in vLPC

In this subsection the results of the optimization of 3C-SiC in vLPC devices are presented. Table 3.4 shows the optimum device dimensions and main figures of merit. As the illumination area changes with the optimization processes, the total input power in the different vLPC structures may vary. The *Quantum Efficiency* (QE) is a useful parameter in order to perform a fair comparison of these devices. Optimum p-layer remains at 51 μm for the two lower P_{in} values, and for 100 W cm^{-2}, 1000 W cm^{-2} and 3000 W cm^{-2} is reduced by a 17.6%, 47.1% and 64.7% respectively. As the P_{in} increases, SRH recombination saturates, and Auger recombination mechanism becomes more relevant. Given that the thickness of the layers in

USC UNIVERSIDADE DE SANTIAGO DE COMPOSTELA

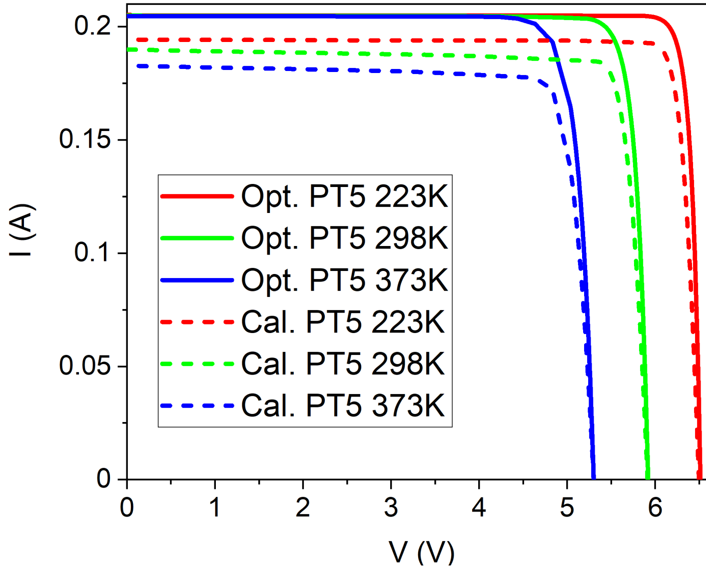

Figure 3.7: IV curves for the optimized (solid lines) and calibrated (dotted lines) VEHSA PT5 at three temperatures: 223 K (blue), 298 K (green) and 373 K (red).

the vertical architecture modifies the illumination area, the optimal thickness tends to shrink with increasing P_{in} in order to reduce the carrier concentration and thus Auger recombination. N-layer optimum thickness is 1 μm for all the P_{in} values except for 3000 W cm^{-2}, where it decreases to 0.1 μm. The optimum p-layer doping increases one order of magnitude over the entire P_{in} range, as the n-layer doping decreases by one order of magnitude. The total width of the device remains at 360 μm for all the P_{in} values studied. As in the vertical architecture there is no trade-off between photon absorption and carrier transport, the width of the device is independent of illumination and is adjusted for optimal absorption.

To compare the effect of the series resistance of the 3C-SiC vLPC with the hLPC devices, Figures 3.8 and 3.9 show the normalized IV curves for both device configurations at the laser power density studied range. Note that for the vLPC there is not any noticeable degradation due to series resistance at any P_{in} value, unlike in the hLPC, where this effect is noticeable at 1000 W cm^{-2} and significantly degrades the performance of the hLPC at higher P_{in} values. QE values are similar for all vLPC devices, reflecting a steady internal conversion between incident photon-collected pair. V_{OC} and V_M grow linearly with the logarithmic increase of

USC UNIVERSIDADE DE SANTIAGO DE COMPOSTELA

Table 3.4: vLPC optimization results and figures of merit for different input power densities (P_{in}). The p and n-layer thickness and doping concentrations are optimized, as well as the vLPC width (see Figure 2.2b). The short circuit current I_{SC}, short circuit current density J_{SC}, quantum efficiency QE, open circuit voltage V_{OC}, voltage at the maximum power point V_M, fill factor FF and efficiency η are shown. The incident wavelength is 525 nm for all the P_{in} values.

Pin[W cm^{-2}]	1		10		100		1000		3000	
Layer	Thick [μm]	Doping [cm^{-3}]	Thick [μm]	Doping [cm^{-3}]	Thick [μm]	Doping [cm^{-3}]	Thick [μm]	Doping [cm^{-3}]	Thick [μm]	Doping [cm^{-3}]
p	51	5e16	51	5e16	42	3e17	27	5e17	18	5e17
n	1	1e17	1	1e17	1	1e16	1	1e16	0.1	1e16
Width [μm]	360		360		360		360		360	
J_{SC} [A cm^{-2}]	$6.42{\cdot}10^{1}$		$6.09{\cdot}10^{2}$		$5.33{\cdot}10^{3}$		$3.29{\cdot}10^{4}$		$6.39{\cdot}10^{4}$	
QE	0.988		0.994		0.992		0.994		0.995	
V_{OC} [V]	2.04		2.10		2.16		2.21		2.23	
V_M [V]	1.92		1.98		2.04		2.08		2.10	
FF [%]	93.2		93.2		93.3		93.0		92.9	

P_{in}. FF is around 93% for all optimizations, indicating almost negligible series resistance losses. Efficiency grows linearly with the logarithmic increase of P_{in} for the studied range. This result, opposed to the behavior in the hLPC, comes from low series resistance and the lesser presence of Auger recombination in the vLPC devices. Note that, the carrier density is lower in the vLPC devices than in the hLPC, since the absorption is made along the entire width of the device without photon recycling.

Figure 3.10 shows V_{OC} and V_M for the hLPC and vLPC under several P_{in} values. The V_{OC} values for the vLPC architecture are lower when compared to those of the hLPC. This can be explained considering the decrease in photogeneration rate across the device width. In the hLPC, there is a trade-off between light absorption and carrier diffusion length. Indeed, a textured back layer is required to increase the optical absorption without drastically increase the recombination losses. This leads to high carrier concentration and therefore to a higher V_{OC}. In the vLPC, there is no such trade-off, as the light absorption occurs in a perpendicular direction to the current flow. This produces better absorption by enlarging the width of the device without affecting the carrier diffusion (see Figure 2.2). Due to the large width of the vLPC (360 μm), the photogeneration rate decreases by one order of magnitude through the device. The collected charge, and therefore the V_{OC}, diminish as light goes deeper into the vLPC. Since the anode and cathode cover the entire width of the device, the overall V_{OC} value will correspond to the voltage in the area with less illumination. Therefore, the width of the

USC UNIVERSIDADE DE SANTIAGO DE COMPOSTELA

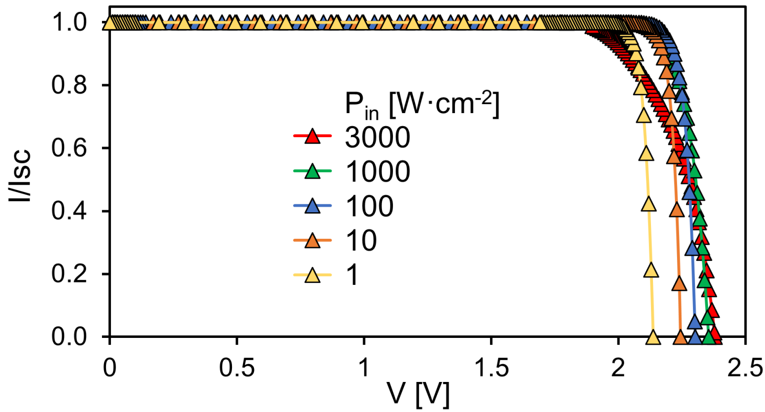

Figure 3.8: IV curves, normalised to each I_{SC}, for various optimized input power densities (P_{in}) in the hLPC.

vLPC must reach a compromise between being large enough to ensure the absorption of most of the beam and maintaining sufficient excess carrier densities to avoid V_{OC} degradation in the least illuminated areas.

For the two architectures V_M grows linearly with the logarithm of the P_{in} at low illumination rates. This progression continues in the vLPC for larger illumination rates, while in the hLPC a degradation of the FF and the V_M appears at 100 W cm^{-2} and above due to series resistance. V_{OC} also grows linearly with the logarithm of the P_{in} in both architectures until Auger recombination affects this parameter at extreme P_{in} values above 1000 W cm^{-2}. However, the vLPC shows a lower dependence on this phenomenon, as already commented. Indeed, the increasing rate of the V_{OC} for the hLPC up to 1000 W cm^{-2} is around 8%, while it is only around 6% (2% lower) above this value. On the contrary, the vLPC shows an increasing rate up to this value of around 6%, while it is only reduced to 5% (1% lower) above this P_{in} value. This also contributes to increasing the efficiency of the vLPC converter with P_{in} in a larger amount. In any case, these results also indicate that Auger recombination is not expected to limit the development of 3C-SiC converters for HPLT applications.

Possible limitations to this technology may arise from the manufacturing side, related to the illumination area. The device area of the state-of-the-art fabricated LPCs is 0.9 mm^2 for Reichmuth et al.[18], around 3 mm^2 for Huang et al.[73] and Kimovec et al.[13], 5.4 mm^2 for Helmers et al.[17] and 11.3 mm^2 for Zhao et al.[74]. In the hLPC architecture, the illumination

USC UNIVERSIDADE DE SANTIAGO DE COMPOSTELA

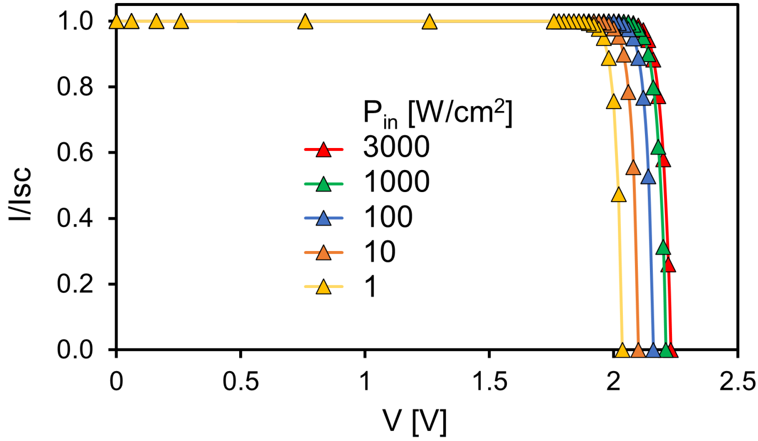

Figure 3.9: IV curves, normalised to each I_{SC}, for various optimized input power densities (P_{in}) in the vLPC.

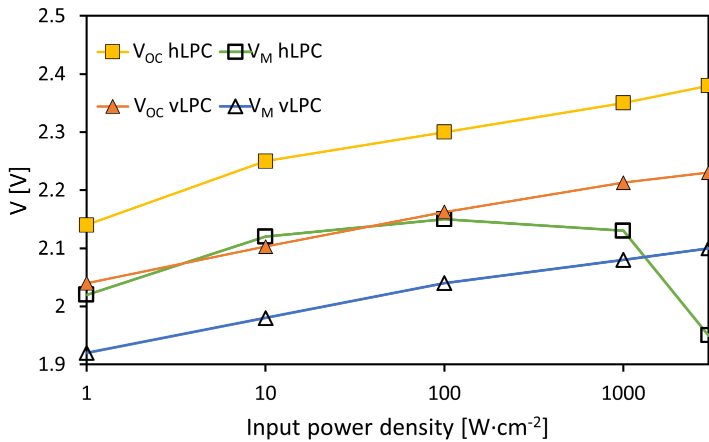

Figure 3.10: V_{OC} and V_M dependence on input power density (P_{in}) for the hLPC and vLPC.

USC UNIVERSIDADE DE SANTIAGO DE COMPOSTELA

area is defined by the width and depth of the device. As previously mentioned, we chose in this work a 1 μm depth for both architectures in order to save computational costs, and a 10 μm width in the hLPC single unit for the same reason. Since the size of 3C-SiC wafers is around 200 mm[75], the hLPC width and depth dimensions can be scaled up and consequently, the active area of this architecture can be in the order of cm^2 if needed. Hence, it would be possible to achieve the same areas than the state-of-the-art LPCs without manufacturing restrictions. In the case of the vLPC, the illumination area is determined by the depth and height of the device. Since the depth can be scaled without performance degradation, the active area of a single vLPC unit, assuming a standard square geometry, is mainly limited by the optimum height, which is also going to depend on the incident power density. For instance, the total height is around 20 μm for an optimum vLPC unit at a Pin value of 3000 W cm^{-2}. This height could be small to achieve similar illumination areas to the state-of-the-art LPCs. However, this dimension can be increased through vertically stacking multiple tunnel junctions (VEHSA), as done in Fafard et al.[16]. Indeed, it has been possible to vertically stack 30 units using tunnel junctions[22]. Taking this into account, the height of the vLPC device could be increased to around 0.6 mm. As commented, the depth can be scaled accordingly, achieving a total square 0.6 mm x 0.6 mm active area device, which is comparable to those of the state-of-the-art LPCs. These dimensions are also recommended since the goal of this architecture is to manage very high input power densities. Hence, an active area of less than 1 mm x 1 mm is recommended to reduce the heat waste and facilitate the thermal management[76]. Note that in the vLPC architecture the junctions are parallel to the light flow, and several identical single units can be vertically stacked without changing their structure, in order to obtain the same current in each single unit, so without increasing the series resistance losses[19, 20]. This simplifies the design and makes it robust against temperature variations (due to change in energy gap and photon absorption), compared to the VEHSA architecture. Finally, it is important to mention that the active area of both architectures can be further increased if needed by arranging the single units onto a series/parallel-connected module[13, 3].

3.3.2 Implementation of 3C-SiC in VEHSA

Given that all polytypes experience performance degradation at high laser power densities, we introduce the Vertical Epitaxial Hetero-Structure Architecture (VEHSA), to minimize this intrinsic limitation of the hLPC architecture. This design was introduced to reduce the series resistance losses by splitting the photogenerated current between vertically stacked N/P cells,

USC UNIVERSIDADE DE SANTIAGO DE COMPOSTELA

while increasing the output voltage in a similar ratio. As the 3C SiC based hLPC has better performance at all input power densities than those based on the other polytypes, we chose this polytype to conduct a comparative between the hLPC conventional architecture and VEHSA devices with 2, 3, and 4 cells. We optimized these devices for input power densities ranging from 1 to 3000 W cm^{-2}, since the VEHSA architecture allows us to use higher laser power densities due to the reduction of series resistance losses.

Table 3.5 shows the optimum design parameters for the VEHSA devices at 1 and 3000 W cm^{-2}, which are the individual cell heights (CH), the relative N/P layer heights, shown in percentage of the correspondent cell height (NH/PH) and the N/P layer doping values (ND/PD). The optimum device height is 106 μm for all the VEHSA devices, which is 23 μm larger than that of the 3C SiC-based hLPC (see Table 3.1). Since the VEHSA architecture consists of monolithically stacked N/P cells (see Figure 2.2), the photogenerated carriers travel less distance than in the hLPC architecture. Therefore the carrier diffusion length is not a limiting factor and the optimum height of VEHSA devices is larger, in order to absorb almost all of the incident beam. The individual cell heights (CH) are adjusted to minimize the current mismatch between the cells. The upper cells are smaller than the lower ones, since the photogeneration decays as the light traverses the device, so each CH needs to be larger to generate the same amount of carriers as in the previous cell. Note that these CH values cannot be obtained through calculations using the Beer-Lambert exponential decay of light, since the optical path is highly increased due to light trapping mechanisms placed at the bottom of the device. Moreover, the optimizer consistently found that optimal configurations are those with the P layer larger than the N layer. This is more pronounced at low input power densities and in the lower cells (those closer to the bottom cell), as can be seen in Table 3.5. The top cell has higher optimum doping values than the other cells, at all configurations and power densities. At a P_{in} value of 1 W cm^{-2} the N layer has optimum donor concentrations in the range of 5e17 and 1e18 cm^{-3}, while the P layer has acceptor concentrations ranging from 1e17 to 3e17 cm^{-3}. At 3000 W cm^{-2} the optimum N doping values decrease to 1e15 cm^{-3}, while the P doping increase to values ranging from 7e17 to 1e18 cm^{-3}.

The voltages (V_M) and current densities (J_M) at the maximum power point provided by each cell at 1 and 3000 W cm^{-2} are shown in Table 3.6. The V_M values of the top cells (cell 1) are larger than those of the other cells due to the higher density of photogenerated carriers (see Equation 3.1). Note that the current mismatch in the J_M is minimal. For example, the VEHSA-2 at 1 W cm^{-2} has a 0.04% current mismatch. The largest observed mismatch is

USC UNIVERSIDADE DE SANTIAGO DE COMPOSTELA

Table 3.5: Design parameters (DP) of the VEHSA devices at 1 and 3000 W cm^{-2}. CH is the cell height, NH/PH the relative N/P layer heights in percentage of the respective CH and ND/PD the doping values for the N/P layers.

Pin		1 W cm^{-2}				3000 W cm^{-2}			
DP		CH	NH/PH	ND	PD	CH	NH/PH	ND	PD
Device	Cell	[μm]	[%]	[cm^{-3}]	[cm^{-3}]	[μm]	[%]	[cm^{-3}]	[cm^{-3}]
VEHSA-2	1	48.6	10/90	1e18	1e17	48.1	35/65	1e15	1e18
	2	57.4	5/95	5e17	1e17	57.9	15/85	1e15	1e18
VEHSA-3	1	30.6	10/90	1e18	3e17	30.5	35/65	1e15	1e18
	2	36.3	5/95	5e17	1e17	36.5	5/95	1e15	1e18
	3	39.1	5/95	5e17	1e17	39.0	5/95	1e15	1e18
VEHSA-4	1	22.4	10/90	1e18	3e17	22.3	45/55	1e15	1e18
	2	25.7	5/95	5e17	3e17	25.8	5/95	1e15	7e17
	3	28.6	5/95	5e17	1e17	28.7	5/95	1e15	7e17
	4	29.3	5/95	5e17	3e17	29.3	5/95	1e15	7e17

a 0.73% for the VEHSA-4 at 1 W cm^{-2}, which shows the good performance of the PhPO algorithm. For 3C SiC only 4 cells are needed to handle these very high input powers, however for other low band gap materials, e.g. GaAs, a much larger number of cells will be needed, which at the same time, will increase the current mismatch, reducing the global efficiency of the system[16].

The JV curves for the hLPC and the VEHSA-2, VEHSA-3 and VEHSA-4 are shown in Figure 3.11 and 3.12 for 1 W cm^{-2} and 3000 W cm^{-2}, respectively. It can be seen that the V_{OC} values increase with larger laser power densities for all devices, ranging from 2.13 to 2.37 V in the hLPC architecture, from 4.28 V to 4.74 V in the VEHSA-2, from 6.42 V to 7.09 V in the VEHSA-3 and from 8.55 V to 9.42 V in the VEHSA-4. The FF is mainly affected by series resistance as the laser power density increases from 1 to 3000 W cm^{-2}, thus reduces from 93.17% to 79.65% in the hLPC architecture, from 93.47% to 88.94% in the VEHSA-2, from 93.62% to 91.36% in the VEHSA-3 and from 93.66% to 92.26% in the VEHSA-4. Note that the fill factor consistently increases with the number of VEHSA cells, and also experiences less degradation at high laser power densities than the hLPC, proving the resilience of the VEHSA architecture to the series resistance losses.

USC
UNIVERSIDADE
DE SANTIAGO
DE COMPOSTELA

Table 3.6: Voltage (V_M) and current density (J_M) at the maximum power point for the hLPC architecture and all the individual cells of the VEHSA-2, VEHSA-3 and VEHSA-4 for 1 and 3000 W cm^{-2} laser power densities.

Pin		1 W cm^{-2}		3000 W cm^{-2}	
FOM		Vm	Jm	Vm	Jm
Device	Cell	[V]	[A cm^{-2}]	[V]	[A cm^{-2}]
hLPC	-	2.010	0.38754	1.96	1109.2
VEHSA-2	1	2.030	0.19815	2.164	587.35
	2	2.018	0.19807	2.117	587.73
VEHSA-3	1	2.050	0.13281	2.223	397.43
	2	2.013	0.13262	2.168	397.97
	3	2.015	0.13289	2.164	396.21
VEHSA-4	1	2.050	0.09930	2.245	298.51
	2	2.021	0.09913	2.181	298.87
	3	2.009	0.09986	2.180	297.63
	4	2.015	0.09983	2.177	298.79

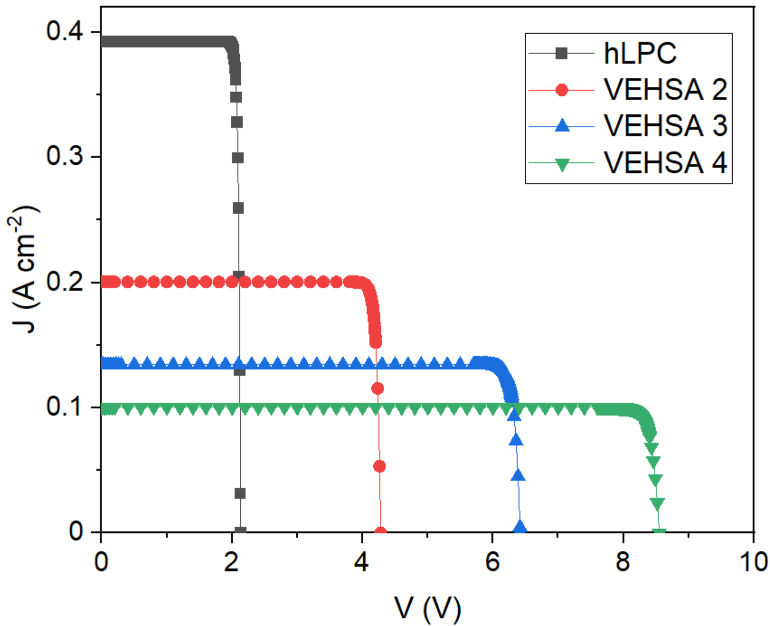

Figure 3.11: JV curves of 3C SiC-based devices using the hLPC architecture and VEHSAs with 2, 3 and 4 cells at 1 W cm^{-2}.

USC UNIVERSIDADE DE SANTIAGO DE COMPOSTELA

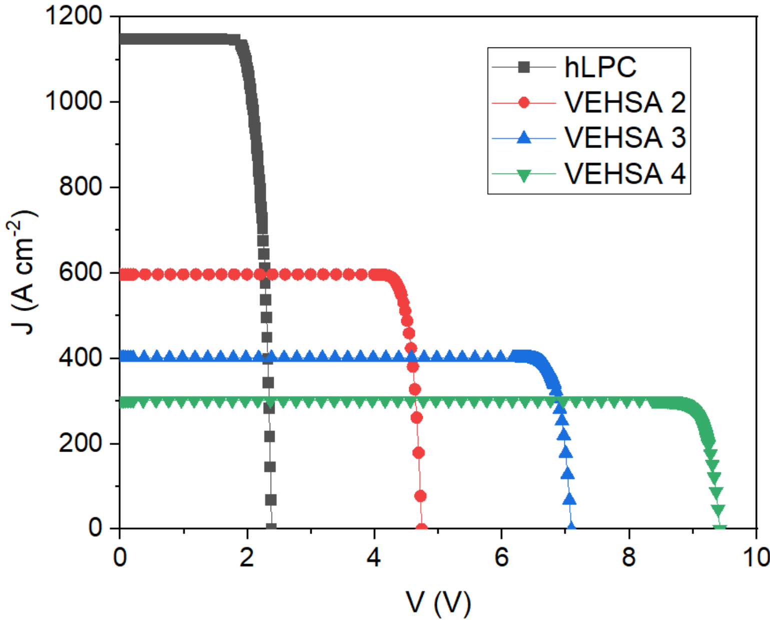

Figure 3.12: JV curves of 3C SiC-based devices using the hLPC architecture and VEHSAs with 2, 3 and 4 cells at 3000 W cm^{-2}.

3.3.3 Comparative with state-of-the-art

Figure 3.13 shows the efficiency as a function of P_{in} for the LPCs studied in this work and for several experimental and simulated state-of-the-art LPCs available in the literature. The values shown in the figure corresponding to this work are for the optimum structures at each P_{in}. The state-of-the-art LPCs shown here are GaAs or AlGaAs/GaAs based, which is the current standard technology. Helmers et al.[17] have achieved a remarkable efficiency of 68.9% at 11.4 W cm^{-2} with the implantation of an optical cavity that minimizes transmission and thermalization losses. This is the highest efficiency achieved by an experimental LPC, and the largest for P_{in} values below 100 W cm^{-2}. The performance of their horizontal device is degraded at higher irradiances than 11.4 W cm^{-2} due to ohmic losses, decreasing to 59.3% at 76.6 W cm^{-2}. Other state-of-the-art devices include a VEHSA device, presented by York et al[21], which achieves an efficiencies of 66% at 64.6 W cm^{-2}

From our proposed architectures, the 3C-SiC hLPC shows a remarkable efficiency between

USC UNIVERSIDADE DE SANTIAGO DE COMPOSTELA

10-100 W cm^{-2} , which could be considered the typical operating range of LPCs. It achieves efficiencies of 78.3%, 82.3% and 84.6% at 1, 10 and 100 W cm^{-2}, improving the current record of Helmers et al.[17] by 13.4% at it best performance laser power density. It also improves by 13.2% the efficiency reported by the Outes et al.[19] simulated GaAs vLPC. At higher P_{in} values, like other horizontal LPCs, it suffers a decrease in efficiency due to growing series resistance losses and Auger recombination. However, the efficiency over all the analyzed P_{in} range is higher than that of the other state- of-the-art horizontal LPCs and the efficiency degradation is less abrupt, resulting in a 13.2% efficiency reduction from 100 W cm^{-2} to 3000 W cm^{-2}. Although the results above are expected to be lower for a real 3C-SiC hLPC device due to additional losses related to manufacturing constraints, e.g. shunt losses, surface recombination, etc, these results are promising to motivate further investigation on the development of highly-efficiency novel LPCs based on 3C-SiC. Also, it is important to remark that the fabrication of 3C-SiC based devices is expected to be cheaper and more environmentally friendly than GaAs based ones, since it involves fewer toxic agents[77] and the fabrication processes have excellent compatibility with those used in Si, employing the same fab lines.

The 3C-SiC vLPC efficiency is comparable to that of the 3C-SiC hLPC for the P_{in} range 1-100 W cm^{-2}. At higher P_{in} values the vertical architecture does not appear to be limited by series resistance, as efficiency keeps growing linearly with the logarithm of P_{in}. The results of the 3C-SiC vLPC are also compared with those of the GaAs-based vLPC introduced by Outes et al.[19], which established the previous efficiency record for a modelled LPC at high P_{in} values, achieving a 76.3% efficiency at 3000 W cm^{-2}. The 3C-SiC vLPC shows an extremely high efficiency of 87.4% at 3000 W cm^{-2}, increasing by 11.1% the result achieved by Outes et al. at this P_{in} value. This is noteworthy since the methodology used in Outes et al. is essentially the same than the one followed in his work. Hence, the difference in the results could mainly be attributed to the reduction of the current due to a lower photon flux density and more favorable materials properties of 3C-SiC compared to those of GaAs.

The 3C-SiC VEHSA devices obtain efficiencies around ≈2% than the hLPC and vLPC devices in the 1-100 W cm^{-2} range. These small differences are due to the higher optimum device height of the VEHSA structures when compared with the hLPC, allowing them to trap a larger part of the beam; and no V_{OC} diminishing due to carrier concentration decay as in the vLPC. Note that the proposed 3C VEHSAs outperform the current best performance experimental GaAs-VEHSA-5 device[16] by a 19.7%, although the proposed devices have

USC UNIVERSIDADE DE SANTIAGO DE COMPOSTELA

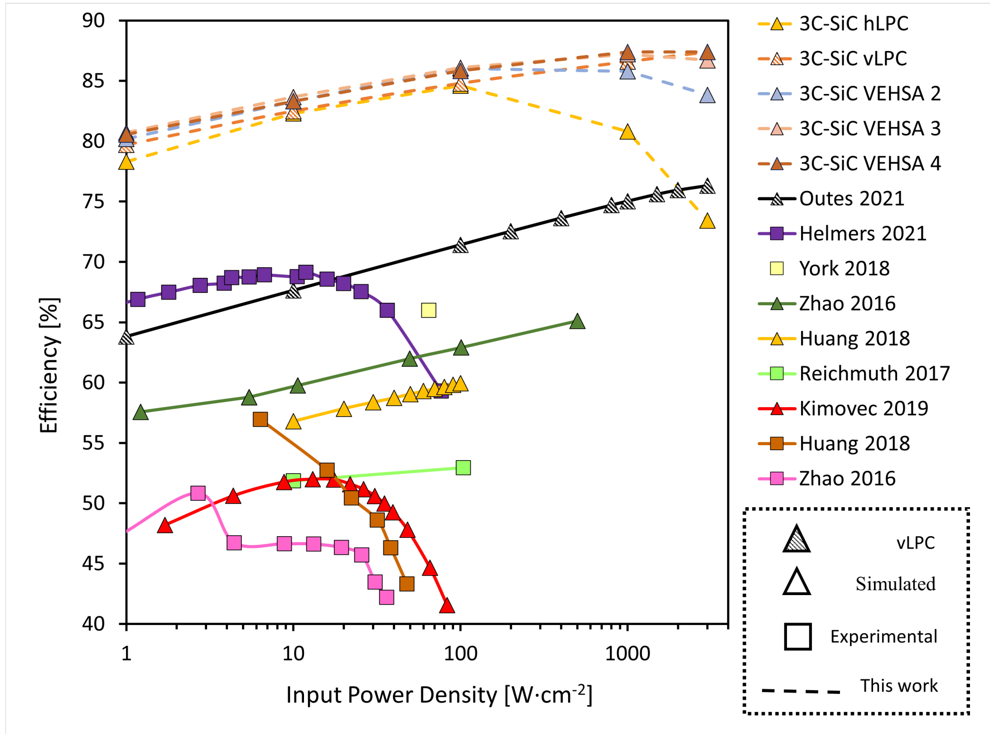

Figure 3.13: Efficiency versus input power density for present work and several state-of-the-art LPCs. vLPC and hLPC refer to the 3C-SiC architectures studied in this work. The LPCs shown correspond to Outes[19], Helmers[17] (illumination area of 0.054 cm^2), York[21], Zhao[74], Huang[73], Reichmuth[18] and Kimovec[78].

not been fabricated yet, so their final performance might be reduced due to manufacturing issues. At an input power density of 1000 W cm^{-2} the VEHSA-2 lose 1.6% efficiency, when compared to the VEHSA-3 and VEHSA-4 due to ohmic losses, which achieve an efficiency of ≈86.3%. At 3000 W cm^{-2} all devices show signs of efficiency degradation except VEHSA-4. This structure outperforms the rest of the devices at this P_{in} value, showing an efficiency of 87.4%, a value 0.7%, 3.6% and 14.9% larger than those of the VEHSA-3, VEHSA-2 and hLPC, respectively. This clearly demonstrates that increasing the number of cells mitigates efficiency degradation due to series resistance losses at high input power densities. Note that the vLPC consistently maintains an efficiency very similar to that of the VEHSA-4, implying that both strategies are capable of mitigate the series resistance effect.

USC UNIVERSIDADE DE SANTIAGO DE COMPOSTELA

Conclusions

The *High-Power Laser Transmission Technology* (HPLT) allows to transfer power sending monochromatic light onto a remote photovoltaic receiver or *Laser Power Converter* (LPC). The absence of wires provides electrical isolation, and enables to deliver power through optic fiber or free space, which is desirable for space applications, among others. This technology faces major limitations when transferring high laser power densities, since the series resistance losses degrade the efficiency of the LPCs. Indeed, the state-of-the-art LPC achieves a maximum conversion efficiency of 68.9% at an *Input power density* (P_{in}) value of 11.4 W cm^{-2}, and rapidly decays at higher laser power densities. Besides, the efficiency of the LPCs is hindered by the properties of the chosen materials, since the low bandgap energies of the semiconductors commonly employed in the state-of-the-art produce intrinsic entropic losses.

Two routes to increase the efficiency of the LPC technology have been studied in this thesis. First, the introduction of three high bandgap semiconductors as base materials for LPCs, being these the *Silicon Carbide* (SiC) polytypes *Cubic Silicon Carbide* (3C-SiC), *Hexagonal 4H Silicon Carbide* (4H-SiC) and *Hexagonal 6H Silicon Carbide* (6H-SiC). This materials could reduce both the series resistance losses and the intrinsic entropic losses. For this, the common *horizontal Laser Power Converter* (hLPC) configuration is used. Second, the implementation of these materials in advanced LPC architectures developed to reduce the series resistance losses, being these configurations the *vertical Laser Power Converters* (vLPC) and the *Vertical Epitaxial Hetero-Structure Architecture* (VEHSA). In addition, this second route required the development of *Technology Computer Aided Design* (TCAD) optimization techniques for the VEHSA architecture to make it feasible for indirect bandgap semiconductors and to improve the current state-of-the-art. For this purpose, the in-house-built optimization algorithm *Photogeneration and Performance Optimization* (PhPO) have been developed.

USC
UNIVERSIDADE DE SANTIAGO DE COMPOSTELA

Implementation of SiC polytypes in the hLPC devices

This work explores the suitability of three silicon carbide polytypes, 3C, 4H and 6H as base materials for the commonly used hLPC architecture. The hLPC structure is optimized for an input power density range of 1-1000 W cm^{-2}. The following conclusions are obtained:

- All the polytypes outperform the current best performance achieved for an experimental LPC, which is a GaAs-based hLPC that obtained a 68.9% efficiency at 11.4 W cm^{-2}. At 10 W cm^{-2}, the SiC polytypes exceed the state of the art by 13.4% for the 3C and by 10% for the 4H and 6H.

- The 3C based hLPCs show greater efficiency than the other polytypes at all the input power densities tested. This is due to the larger effective *Density Of States* (DOS) values of the 4H, which diminish the growth of the *open circuit voltage* (V_{OC}) with the increase of P_{in}, and the 6H Auger coefficients, which severely degrade the performance of the 6H hLPCs as P_{in} increases.

- 3C-SiC shows higher resilience to efficiency degradation when the temperature increases than the other two polytypes.

- The 3C hLPC reaches a maximum efficiency value of 84.6% at 100 W cm^{-2}. However, as the laser power density increases, the 3C hLPC suffers from efficiency degradation, decreasing to 80.8% at 1000 W cm^{-2}. This effect is less abrupt than in other hLPCs in the literature, indicating better performance at high injection levels.

Although the performance of real 3C-SiC-based hLPCs can be affected by manufacturing issues, these results indicate that 3C-SiC could be a promising candidate to replace *Gallium Arsenide* (GaAs) as the base material for high-efficiency LPCs for all input power range. In addition, the efficiency degradation observed at high laser power densities could be mitigated by using advanced architectures.

Development of VEHSA optimization algorithm: PhPO

This work presents a new method to optimize the design parameters of VEHSA devices, one of the most efficient architectures of state-of-the-art LPCs. The Photogeneration and Performance Optimization (PhPO) method combines device TCAD with an iterative optimization algorithm.

USC UNIVERSIDADE DE SANTIAGO DE COMPOSTELA

This method is aimed to bypass the main limitations of the VEHSA architecture, namely the current mismatch between cells and the impossibility of tailoring individual cell design parameters. Traditionally, the Beer-Lambert law of exponential decay is the main available tool to match the different cells photogeneration. However, this method obtains low accuracy results when a back reflector or light-trapping mechanisms are included. Another issue related to only applying Beer-Lambert law is that the individual currents of each cell may differ, due to the different performance of the cells, leading to current mismatch. The conclusions of the PhPO performance are the following:

- To validate the PhPO method, the current room temperature record efficiency VEHSA device is modelled, a GaAs-based 5-cell. The TCAD device accurately reproduces the experimental device IV curves at the same illumination conditions, using similar design parameters.
- The iterative optimization algorithm is applied to the calibrated VEHSA. The algorithm successfully matches all cells *short circuit current* (I_{SC}) and V_{OC} values and improves each cell performance. This leds to a 9.5% efficiency increase of the optimized device with respect to the experimental VEHSA.
- Given the diverse applications of hLPCs, this work tested both the optimized and calibrated VEHSA at 3 different temperatures: 223 K, 298 K and 373 K. The optimized device is slightly more resilient to temperature changes due to a reduction of the recombination effects achieved by the optimization of design parameters.

The PhPO method provides optimum design parameters for state-of-the-art and new generation VEHSA devices, opening a new route towards ultra-efficient VEHSAs with application to hLPC and tandem solar cells, not necessarily based on direct bandgap materials.

3C-SiC as base material for advanced architectures

The 3C-SiC hLPC devices suffer from efficiency degradation at high laser power densities. To counteract for this effect, this work presents optimizations of 3C-SiC in the advanced architectures vLPC and VEHSA in the laser power density range of 1 to 3000 W cm^{-2}, obtaining the following conclusions:

USC UNIVERSIDADE DE SANTIAGO DE COMPOSTELA

- The 3C-SiC vLPC efficiency is comparable to that of the 3C-SiC hLPC for the P_{in} range 1-100 W cm^{-2}, and improves the results of the state-of-the-art vLPC devices (based on GaAs) by 11.1%.

- The 3C-SiC vLPC shows no degradation over the entire power range studied, due to extremely low series resistance and a significantly reduced Auger recombination with respect to hLPC. This leads to a conversion efficiency of 87.4% at 3000 W cm^{-2}, exhibiting a linear growth of efficiency with the logarithm of input power density, allowing room for improvement at higher powers.

- Optimizations of 3C-SiC-based VEHSA devices with 2, 3 and 4 cells were performed with the PhPO optimization algorithm. Results show that the VEHSA performs around ≈2% better than the hLPC and vLPC architectures at the 1-100 W cm^{-2} laser power range.

- Increasing the number of VEHSA cells mitigates the losses due to Joule effect. At high laser power densities, the VEHSA-2 suffers from series resistance losses, with a 1.6% and 3.6% efficiency drop at 1000 and 3000 W cm^{-2}, respectively, when compared to the VEHSA-4, but outperforms the hLPC by a 5% and a 11.3% at these laser power densities.

- At 3000 W cm^{-2}, the VEHSA-4 achieves a 87.4% efficiency. Note that, using 3C-SiC, only 4 cells are needed to handle these extremely large input powers, whereas when using low bandgap materials (such as GaAs) VEHSA devices with larger numbers of cells are mandatory, which suffer from current mismatch issues.

- Both the vLPC and the VEHSA-4 achieve approximately the same efficiency at ultra-high laser power densities, which indicates that both strategies are viable to mitigate series resistance losses.

These results generate confidence in a new generation of laser power converters with the capacity to revolutionize the market and broaden the possible applications of the wireless power transmission technology. Although the performance of real SiC-based LPCs may be impacted by manufacturing issues, the presented work shows that the combined use of 3C-SiC and advanced architectures are beneficial additions and open a promising route towards efficiently transmit ultra-high laser power densities.

USC UNIVERSIDADE DE SANTIAGO DE COMPOSTELA

Future work

The work shown here creates a new paradigm shift with the possibility of transferring power densities up to kilowatts per square centimeter to large distances through a mediums like terrestrial atmosphere (powering aerial drones, remote sensors and robots), water (in underwater autonomous vehicles) or outer space (in rovers and satellites). Another advantage of the silicon carbide is that it can be grown on Si wafers, notably reducing the costs. The thermal conductivity of the SiC polytypes is significantly larger than that of GaAs, making it preferrable in space applications, where GaAs is currently the best choice. SiC polytypes have also high resistance to radiation and dielectric strength, and the manufacture of SiC-based power converters is based on non-critical raw materials and eco-friendly processes, contrary to the case of III-V materials.

However, the manufacturing of those devices might be challenging, since, to the authors' knowledge, silicon carbide power converters have not been fabricated yet. The production of very high quality, defect-free SiC PN junctions will be crytical to achieve successfull power converters. Good passivation of surfaces can be achieved in silicon carbide since the expertise in silicon can be applied here. Another critical aspect is to make good ohmic contacts for the anode and cathode.

In future work, the authors will explore the feasibility of other promising high bandgap materials, as Gallium Nitride (GaN). Another crucial aspect for this technology to success is the behavior of the power converters with the temperature. For that, detailed simulations with heat transport models will be carried out. Heat dissipation systems will be proposed depending on specific applications for the LPCs, either on space or terrestrial environments. The work presented here will be continued by detailed characterization of SiC crystals and manufacturing of SiC-based hLPC prototypes.

Other potential challenges to address in the future are the need of a tracking system for the target, a direct line from the laser source to the LPC, the possible high laser power attenuation in media like air (lower in SiC than in conventional GaAs based LPCs[29]) or the eye safety implications due to using high power lasers operating in the visible regime. These issues need to be considered in future projects.

USC UNIVERSIDADE DE SANTIAGO DE COMPOSTELA

Bibliography

[1] K. Jin and W. Zhou, "Wireless Laser Power Transmission: A Review of Recent Progress," *IEEE Transactions on Power Electronics*, vol. 34, no. 4, pp. 3842–3859, 2019.

[2] X. Lu, P. Wang, D. Niyato, D. I. Kim, and Z. Han, "Wireless Charging Technologies: Fundamentals, Standards, and Network Applications," *IEEE Communications Surveys and Tutorials*, vol. 18, no. 2, pp. 1413–1452, 2016.

[3] C. Algora, I. García, M. Delgado, R. Peña, C. Vázquez, M. Hinojosa, and I. Rey-Stolle, "Beaming power: Photovoltaic laser power converters for power-by-light," *Joule*, no. 2021, pp. 1–29, 12 2021. [Online]. Available: https://linkinghub.elsevier.com/retrieve/pii/S2542435121005407

[4] D. Krut, R. Sudharsanan, W. Nishikawa, T. Isshiki, J. Ermer, and N. H. Karam, "Monolithic multi-cell GaAs laser power converter with very high current density," *Conference Record of the IEEE Photovoltaic Specialists Conference*, pp. 908–911, 2002.

[5] M. Matsuura, H. Nomoto, H. Mamiya, T. Higuchi, D. Masson, and S. Fafard, "Over 40-W Electric Power and Optical Data Transmission Using an Optical Fiber," *IEEE Transactions on Power Electronics*, vol. 36, no. 4, pp. 4532–4539, 2021.

[6] H. Helmers, C. Armbruster, M. Von Ravenstein, D. Derix, and C. Schoner, "6-W Optical Power Link with Integrated Optical Data Transmission," *IEEE Transactions on Power Electronics*, vol. 35, no. 8, pp. 7904–7909, 2020.

[7] C. Vázquez, J. D. López-Cardona, P. C. Lallana, D. S. Montero, F. M. A. Al-Zubaidi, S. Pérez-Prieto, and I. Pérez Garcilópez, "Multicore Fiber Scenarios Supporting Power over Fiber in Radio over Fiber Systems," *IEEE Access*, vol. 7, pp. 158 409–158 418, 2019.

USC
UNIVERSIDADE DE SANTIAGO DE COMPOSTELA

[8] N. Kawashima, K. Takeda, H. Matsuoka, Y. Fujii, and M. Yamamoto, "Laser Energy Transmission for a Wireless Energy Supply to Robots," in *22nd International Symposium on Automation and Robotics in Construction, ISARC 2005*. Ferrara, Italy: International Association for Automation and Robotics in Construction (IAARC), 9 2005.

[9] D. Shi, L. Zhang, H. Ma, Z. Wang, Y. Wang, and Z. Cui, "Research on Wireless Power transmission system between satellites," in *2016 IEEE Wireless Power Transfer Conference, WPTC 2016*, vol. 3. IEEE, 5 2016, pp. 1–4.

[10] M. Sanders and J. S. Kang, "Utilization of Polychromatic Laser System for Satellite Power Beaming," *IEEE Aerospace Conference Proceedings*, pp. 1–7, 2020.

[11] J. Schubert, E. Oliva, F. Dimroth, W. Guter, R. Loeckenhoff, and A. W. Bett, "High-voltage GaAs photovoltaic laser power converters," *IEEE Transactions on Electron Devices*, vol. 56, no. 2, pp. 170–175, 2009.

[12] H. Helmers, L. Wagner, C. E. Garza, S. K. Reichmuth, E. Oliva, S. Philipps, D. Lackner, and A. Bett, "D1.4 - Photovoltaic Cells with Increased Voltage Output for Optical Power Supply of Sensor Electronics," in *Proceedings SENSOR 2015*. AMA Service GmbH, Von-Münchhausen-Str. 49, 31515 Wunstorf, Germany, 2015, pp. 519–524. [Online]. Available: http://www.ama-science.org/doi/10.5162/sensor2015/D1.4

[13] R. Kimovec, H. Helmers, A. W. Bett, and M. Topič, "Comprehensive electrical loss analysis of monolithic interconnected multi-segment laser power converters," *Progress in Photovoltaics: Research and Applications*, vol. 27, no. 3, pp. 199–209, 2019.

[14] T. Shan and X. Qi, "Design and optimization of GaAs photovoltaic converter for laser power beaming," *Infrared Physics and Technology*, vol. 71, pp. 144–150, 2015. [Online]. Available: http://dx.doi.org/10.1016/j.infrared.2015.03.010

[15] R. Sudharsanan, D. Krut, T. Isshiki, H. Cotal, S. Mesropian, A. Masalykin, and N. H. Karam, "A 53% high efficiency GaAs vertically integrated multi-junction laser power converter," *Conference Proceedings - Lasers and Electro-Optics Society Annual Meeting-LEOS*, vol. 196, no. 818, p. 30, 2008.

[16] S. Fafard, F. Proulx, M. C. A. York, L. S. Richard, P. O. Provost, R. Arès, V. Aimez, and D. P. Masson, "High-photovoltage GaAs vertical epitaxial monolithic

USC UNIVERSIDADE DE SANTIAGO DE COMPOSTELA

heterostructures with 20 thin p/n junctions and a conversion efficiency of 60%," *Applied Physics Letters*, vol. 109, no. 13, p. 131107, 9 2016. [Online]. Available: http://aip.scitation.org/doi/10.1063/1.4964120

[17] H. Helmers, E. Lopez, O. Höhn, D. Lackner, J. Schön, M. Schauerte, M. Schachtner, F. Dimroth, and A. W. Bett, "68.9% Efficient GaAs-Based Photonic Power Conversion Enabled by Photon Recycling and Optical Resonance," *Physica Status Solidi - Rapid Research Letters*, vol. 15, no. 7, pp. 1–7, 2021.

[18] S. K. Reichmuth, H. Helmers, S. P. Philipps, M. Schachtner, G. Siefer, and A. W. Bett, "On the temperature dependence of dual-junction laser power converters," *Progress in Photovoltaics: Research and Applications*, vol. 25, no. 1, pp. 67–75, 1 2017. [Online]. Available: https://onlinelibrary.wiley.com/doi/10.1002/pip.2814

[19] C. Outes, E. F. Fernandez, N. Seoane, F. Almonacid, and A. J. Garcia-Loureiro, "GaAs Vertical-Tunnel-Junction Converter for Ultra-High Laser Power Transfer," *IEEE Electron Device Letters*, pp. 1–1, 2021.

[20] N. Seoane, E. F. Fernández, F. Almonacid, and A. García-Loureiro, "Ultra-efficient intrinsic-vertical-tunnel-junction structures for next-generation concentrator solar cells," *Progress in Photovoltaics: Research and Applications*, vol. 29, no. 2, pp. 231–237, 2021.

[21] M. C. York, A. Mailhot, A. Boucherif, R. Arès, V. Aimez, and S. Fafard, "Challenges and strategies for implementing the vertical epitaxial heterostructure architechture (VEHSA) design for concentrated photovoltaic applications," *Solar Energy Materials and Solar Cells*, vol. 181, no. December 2017, pp. 46–52, 2018. [Online]. Available: https://doi.org/10.1016/j.solmat.2017.11.034

[22] S. Fafard and D. P. Masson, "Perspective on photovoltaic optical power converters," *Journal of Applied Physics*, vol. 130, no. 16, p. 160901, 10 2021. [Online]. Available: https://aip.scitation.org/doi/10.1063/5.0070860

[23] S. P. Philipps and A. W. Bett, "III-V Multi-junction solar cells and concentrating photovoltaic (CPV) systems," pp. 469–478, 12 2014.

[24] Y. Cui, D. van Dam, S. A. Mann, N. J. J. van Hoof, P. J. van Veldhoven, E. C. Garnett, E. P. A. M. Bakkers, and J. E. M. Haverkort, "Boosting Solar Cell Photovoltage via

USC UNIVERSIDADE DE SANTIAGO DE COMPOSTELA

Nanophotonic Engineering," *Nano Letters*, vol. 16, no. 10, pp. 6467–6471, 10 2016. [Online]. Available: https://pubs.acs.org/doi/10.1021/acs.nanolett.6b02971

[25] D. Masson, F. Proulx, and S. Fafard, "Pushing the limits of concentrated photovoltaic solar cell tunnel junctions in novel high-efficiency GaAs phototransducers based on a vertical epitaxial heterostructure architecture," *Progress in Photovoltaics: Research and Applications*, vol. 23, no. 12, pp. 1687–1696, 12 2015. [Online]. Available: http://dx.doi.org/10.1002/pip.1160https://onlinelibrary.wiley.com/doi/10.1002/pip.2709

[26] M. C. York, F. Proulx, D. P. Masson, A. Jaouad, B. Bouzazi, R. Arès, V. Aimez, and S. Fafard, "Thin n/p GaAs Junctions for Novel High-Efficiency Phototransducers Based on a Vertical Epitaxial Heterostructure Architecture," in *MRS Advances*, vol. 1, no. 14. Materials Research Society, 2016, pp. 881–890.

[27] M. C. A. York and S. Fafard, "High efficiency phototransducers based on a novel vertical epitaxial heterostructure architecture (VEHSA) with thin p/n junctions," *Journal of Physics D: Applied Physics*, vol. 50, no. 17, p. 173003, 5 2017. [Online]. Available: https://iopscience.iop.org/article/10.1088/1361-6463/aa60a6

[28] S. Čičić and S. Tomić, "Genetic algorithm designed high efficiency laser power converters based on the vertical epitaxial heterostructure architecture," *Solar Energy Materials and Solar Cells*, vol. 200, p. 109878, 9 2019. [Online]. Available: https://linkinghub.elsevier.com/retrieve/pii/S0927024819301680

[29] E. F. Fernández, A. García-Loureiro, N. Seoane, and F. Almonacid, "Band-gap material selection for remote high-power laser transmission," *Solar Energy Materials and Solar Cells*, vol. 235, no. September 2021, p. 111483, 2022.

[30] E. Oliva, F. Dimroth, and A. W. Bett, "GaAs converters for high power densities of laser illumination," *Progress in Photovoltaics: Research and Applications*, vol. 16, no. 4, pp. 289–295, 6 2008. [Online]. Available: https://onlinelibrary.wiley.com/doi/10.1002/pip.811

[31] M. Lin, W. E. Sha, W. Zhong, and D. Xu, "Intrinsic losses in photovoltaic laser power converters," *Applied Physics Letters*, vol. 118, no. 10, pp. 1–5, 2021.

[32] X. She, A. Q. Huang, O. Lucia, and B. Ozpineci, "Review of Silicon Carbide Power Devices and Their Applications," *IEEE Transactions on Industrial*

USC UNIVERSIDADE DE SANTIAGO DE COMPOSTELA

Electronics, vol. 64, no. 10, pp. 8193–8205, 10 2017. [Online]. Available: http://ieeexplore.ieee.org/document/7815312/

[33] J. N. Shenoy, J. A. Cooper, and M. R. Melloch, "High-voltage double-implanted power MOSFET's in 6H-SiC," *IEEE Electron Device Letters*, vol. 18, no. 3, pp. 93–95, 1997.

[34] I. G. Ivanov, R. Liljedahl, R. Yakimova, and M. Syväjärvi, "Considerably long carrier lifetimes in high-quality 3C-SiC(111)," *Applied Physics Letters*, vol. 100, no. 25, p. 252101, 6 2012. [Online]. Available: http://aip.scitation.org/doi/10.1063/1.4729583

[35] P. Neudeck, A. Trunek, D. Spry, J. Powell, H. Du, M. Skowronski, X. Huang, and M. Dudley, "CVD Growth of 3C-SiC on 4H/6H Mesas," *Chemical Vapor Deposition*, vol. 12, no. 8-9, pp. 531–540, 9 2006. [Online]. Available: https://onlinelibrary.wiley.com/doi/10.1002/cvde.200506460

[36] T. Miyazawa, M. Ito, and H. Tsuchida, "Evaluation of long carrier lifetimes in thick 4H silicon carbide epitaxial layers," *Applied Physics Letters*, vol. 97, no. 20, 11 2010.

[37] S. A. Reshanov and G. Pensl, "Comparison of Electrically and Optically Determined Minority Carrier Lifetimes in 6H-SiC," *Materials Science Forum*, vol. 483-485, pp. 417–420, 5 2005. [Online]. Available: https://www.scientific.net/MSF.483-485.417

[38] J.-M. Lauenstein, M. C. Casey, R. L. Ladbury, H. S. Kim, A. M. Phan, and A. D. Topper, "Space Radiation Effects on SiC Power Device Reliability," in *2021 IEEE International Reliability Physics Symposium (IRPS)*. IEEE, 3 2021, pp. 1–8.

[39] S. Tudisco, F. La Via, C. Agodi, C. Altana, G. Borghi, M. Boscardin, G. Bussolino, L. Calcagno, M. Camarda, F. Cappuzzello, D. Carbone, S. Cascino, G. Casini, M. Cavallaro, C. Ciampi, G. Cirrone, G. Cuttone, A. Fazzi, D. Giove, G. Gorini, L. Labate, G. Lanzalone, G. Litrico, G. Longo, D. Lo Presti, M. Mauceri, R. Modica, M. Moschetti, A. Muoio, F. Musumeci, G. Pasquali, G. Petringa, N. Piluso, G. Poggi, S. Privitera, S. Puglia, V. Puglisi, M. Rebai, S. Ronchin, A. Santangelo, A. Stefanini, A. Trifirò, and M. Zimbone, "SiCILIA—Silicon Carbide Detectors for Intense Luminosity Investigations and Applications," *Sensors*, vol. 18, no. 7, p. 2289, 7 2018.

[40] R. K. Baruah, B. K. Mahajan, Y.-P. Chen, and R. P. Paily, "A Junctionless Silicon Carbide Transistor for Harsh Environment Applications," *Journal of Electronic Materials*, vol. 50, no. 10, pp. 5682–5690, 10 2021.

USC UNIVERSIDADE DE SANTIAGO DE COMPOSTELA

[41] E. J. Brandon, R. Bugga, J. Grandidier, J. L. Hall, J. A. Schwartz, and S. Limaye, "Power Beaming for Long Life Venus Surface Missions NIAC Phase I Final Report," Tech. Rep., 2020.

[42] P. Colter, B. Hagar, and S. Bedair, "Tunnel junctions for III-V multijunction solar cells review," 12 2018.

[43] A. E. Arvanitopoulos, M. Antoniou, S. Perkins, M. Jennings, M. B. Guadas, K. N. Gyftakis, and N. Lophitis, "On the Suitability of 3C-Silicon Carbide as an Alternative to 4H-Silicon Carbide for Power Diodes," *IEEE Transactions on Industry Applications*, vol. 55, no. 4, pp. 4080–4090, 7 2019.

[44] Silvaco, "Silvaco software (version 5.30.0.R)," *https://www.silvaco.com*, 2020.

[45] Y. Goldberg, M. Levinshtein, and S. Rumyantsev, "Properties of advanced semiconductor materials: GaN, AIN, InN, BN, SiC, SiGe," *SciTech Book News*, vol. 25, pp. 93–146, 10 2001.

[46] Z. Cheng, J. Liang, K. Kawamura, H. Zhou, H. Asamura, H. Uratani, J. Tiwari, S. Graham, Y. Ohno, Y. Nagai, T. Feng, N. Shigekawa, and D. G. Cahill, "High thermal conductivity in wafer-scale cubic silicon carbide crystals," *Nature Communications*, vol. 13, no. 1, 12 2022.

[47] D. M. Caughey and R. E. Thomas, "Carrier Mobilities in Silicon Empirically Related to Doping and Field," *Proceedings of the IEEE*, vol. 55, no. 12, pp. 2192–2193, 1967.

[48] A. Arvanitopoulos, N. Lophitis, K. N. Gyftakis, S. Perkins, and M. Antoniou, "Validated physical models and parameters of bulk 3C-SiC aiming for credible technology computer aided design (TCAD) simulation," *Semiconductor Science and Technology*, vol. 32, no. 10, pp. 1–15, 2017.

[49] G. L. Harris, *Properties of silicon carbide*, ser. EMIS datareviews series ; no. 13, G. L. Harris, Ed. London: INSPEC, Institution of Electrical Engineers, 1995.

[50] M. E. Law, E. Solley, M. Liang, and D. E. Burk, "Self-Consistent Model of Minority-Carrier Lifetime, Diffusion Length, and Mobility," *IEEE Electron Device Letters*, vol. 12, no. 8, pp. 401–403, 1991.

USC
UNIVERSIDADE DE SANTIAGO DE COMPOSTELA

[51] W. Shockley and W. T. Read, “Statistics of the recombinations of holes and electrons,” *Physical Review*, vol. 87, no. 5, pp. 835–842, 1952.

[52] J. Dziewior and W. Schmid, “Auger coefficients for highly doped and highly excited silicon,” *Applied Physics Letters*, vol. 31, no. 5, pp. 346–348, 1977.

[53] J. D. Beck and R. Conradt, “Auger-rekombination in Si,” *Solid State Communications*, vol. 13, no. 1, pp. 93–95, 1973.

[54] A. Arvanitopoulos, N. Lophitis, S. Perkins, K. N. Gyftakis, M. Belanche Guadas, and M. Antoniou, “Physical parameterisation of 3C-Silicon Carbide (SiC) with scope to evaluate the suitability of the material for power diodes as an alternative to 4H-SiC,” in *2017 IEEE 11th International Symposium on Diagnostics for Electrical Machines, Power Electronics and Drives (SDEMPED)*. IEEE, 8 2017, pp. 565–571.

[55] U. Strauss, W. W. Rühle, and K. Köhler, “Auger recombination in intrinsic GaAs,” *Applied Physics Letters*, vol. 62, no. 1, pp. 55–57, 1993.

[56] S. Onoda, T. Ohshima, T. Hirao, K. Mishima, S. Hishiki, N. Iwamoto, and K. Kawano, “Impact of auger recombination on charge collection of a 6H-SiC diode by heavy ions,” *IEEE Transactions on Nuclear Science*, vol. 54, no. 6, pp. 2706–2713, 2007.

[57] A. Vossier, B. Hirsch, and J. M. Gordon, “Is Auger recombination the ultimate performance limiter in concentrator solar cells?” *Applied Physics Letters*, vol. 97, no. 19, pp. 0–3, 2010.

[58] U. Lindefelt, “A model for doping-induced band gap narrowing in 3C-, 4H-, and 6H-SiC,” *Materials Science and Engineering: B*, vol. 61-62, pp. 225–228, 7 1999. [Online]. Available: https://linkinghub.elsevier.com/retrieve/pii/S0921510798005078

[59] A. Valera, E. F. Fernández, P. M. Rodrigo, and F. Almonacid, “Feasibility of flat-plate heat-sinks using microscale solar cells up to 10,000 suns concentrations,” *Solar Energy*, vol. 181, no. November 2018, pp. 361–371, 2019. [Online]. Available: https://doi.org/10.1016/j.solener.2019.02.013

[60] E. D. Palik, S. Diego, L. Boston, N. York, and S. T. Toronto, “Handbook of Optical Constants of Solids,” Tech. Rep., 1998.

USC UNIVERSIDADE DE SANTIAGO DE COMPOSTELA

[61] M. A. Green, J. Zhao, A. Wang, and S. R. Wenham, “45% Efficient Silicon Photovoltaic Cell Under Monochromatic Light,” *IEEE Electron Device Letters*, vol. 13, no. 6, pp. 317–318, 1992.

[62] H. Ou, Y. Ou, A. Argyraki, S. Schimmel, M. Kaiser, P. Wellmann, M. K. Linnarsson, V. Jokubavicius, J. Sun, R. Liljedahl, and M. Syväjärvi, “Advances in wide bandgap SiC for optoelectronics,” *The European Physical Journal B*, vol. 87, no. 3, p. 58, 4 2014. [Online]. Available: http://link.springer.com/10.1140/epjb/e2014-41100-0

[63] E. F. Fernandez, N. Seoane, F. Almonacid, and A. J. Garcia-Loureiro, “Vertical-tunnel-junction (VTJ) solar cell for ultra-high light concentrations (>2000 suns),” *IEEE Electron Device Letters*, vol. 40, no. 1, pp. 1–1, 2018. [Online]. Available: https://ieeexplore.ieee.org/document/8528429/

[64] C. Outes, E. F. Fernández, N. Seoane, F. Almonacid, and A. J. García-Loureiro, “Numerical optimisation and recombination effects on the vertical-tunnel-junction (VTJ) GaAs solar cell up to 10,000 suns,” *Solar Energy*, vol. 203, no. January, pp. 136–144, 2020. [Online]. Available: https://doi.org/10.1016/j.solener.2020.04.029

[65] S. Fafard, D. Masson, J. G. Werthen, J. Liu, T. C. Wu, C. Hundsberger, M. Schwarzfischer, G. Steinle, C. Gaertner, C. Piemonte, B. Luecke, J. Wittl, and M. Weigert, “Power and spectral range characteristics for optical power converters,” *Energies*, vol. 14, no. 15, pp. 1–14, 2021.

[66] L. Wagner, S. K. Reichmuth, S. P. Philipps, E. Oliva, A. W. Bett, and H. Helmers, “Integrated series/parallel connection for photovoltaic laser power converters with optimized current matching,” *Progress in Photovoltaics: Research and Applications*, vol. 29, no. 2, pp. 172–180, 2021.

[67] M. C. A. York, F. Proulx, D. P. Masson, A. Jaouad, B. Bouzazi, R. Arès, V. Aimez, and S. Fafard, “Enhanced photocarrier extraction mechanisms in ultra-thin photovoltaic GaAs n/p junctions,” A. Freundlich, L. Lombez, and M. Sugiyama, Eds., 3 2016, p. 97430Y.

[68] M. H. Tsutagawa and S. Michael, “Triple junction InGaP/GaAS/Ge solar cell optimization: The design parameters for a 36.2% efficient space cell using Silvaco ATLAS modeling & simulation,” in *2009 34th IEEE Photovoltaic Specialists*

USC UNIVERSIDADE DE SANTIAGO DE COMPOSTELA

Conference (PVSC). IEEE, 6 2009, pp. 001 954–001 957. [Online]. Available: http://ieeexplore.ieee.org/document/5411544/

[69] R. J. Kilway II, "Five-junction solar cell optimization using Silvaco ATLAS," Ph.D. dissertation, Naval Postgraduate School, Monterey, 2017. [Online]. Available: https://archive.org/details/fivejunctionsola1094556146

[70] R. A. Sinton and A. Cuevas, "Contactless determination of current–voltage characteristics and minority-carrier lifetimes in semiconductors from quasi-steady-state photoconductance data," *Applied Physics Letters*, vol. 69, no. 17, pp. 2510–2512, 10 1996. [Online]. Available: https://pubs.aip.org/apl/article/69/17/2510/66640/Contactless-determination-of-current-voltage

[71] H. C. Casey, D. D. Sell, and K. W. Wecht, "Concentration dependence of the absorption coefficient for n and p type GaAs between 1.3 and 1.6 eV," *Journal of Applied Physics*, vol. 46, no. 1, pp. 250–257, 1 1975. [Online]. Available: http://aip.scitation.org/doi/10.1063/1.321330

[72] S. Sze and K. K. Ng, *Physics of Semiconductor Devices*. Hoboken, NJ, USA: John Wiley & Sons, Inc., 10 2006. [Online]. Available: http://doi.wiley.com/10.1002/0470068329

[73] J. Huang, Y. Sun, Y. Zhao, S. Yu, J. Dong, J. Xue, C. Xue, J. Wang, Y. Lu, and Y. Ding, "Four-junction AlGaAs/GaAs laser power converter," *Journal of Semiconductors*, vol. 39, no. 4, p. 044003, 4 2018. [Online]. Available: https://iopscience.iop.org/article/10.1088/1674-4926/39/4/044003

[74] Y. Zhao, Y. Sun, Y. He, S. Yu, and J. Dong, "Design and fabrication of six-volt vertically-stacked GaAs photovoltaic power converter," *Scientific Reports*, vol. 6, no. June, pp. 1–9, 2016. [Online]. Available: http://dx.doi.org/10.1038/srep38044

[75] M. Schoeler, P. Schuh, G. Litrico, F. L. Via, M. Mauceri, and Peter J. Wellmann, "Characterization of protrusions and stacking faults in 3C-SiC grown by sublimation epitaxy using 3C-SiC-on-Si seeding layers," *Advanced Materials Proceedings*, vol. 2, no. 12, pp. 774–778, 12 2017. [Online]. Available: https://amp.iaamonline.org/article_16263.html

[76] L. Micheli, E. F. Fernández, F. Almonacid, T. K. Mallick, and G. P. Smestad, "Performance, limits and economic perspectives for passive cooling of High

USC UNIVERSIDADE DE SANTIAGO DE COMPOSTELA

Concentrator Photovoltaics," *Solar Energy Materials and Solar Cells*, vol. 153, pp. 164–178, 2016. [Online]. Available: http://dx.doi.org/10.1016/j.solmat.2016.04.016

[77] H. Joël Tchognia Nkuissi, F. Kouadio Konan, B. Hartiti, and J.-M. Ndjaka, "Toxic Materials Used in Thin Film Photovoltaics and Their Impacts on Environment," *Reliability and Ecological Aspects of Photovoltaic Modules*, pp. 1–18, 2020.

[78] R. Kimovec, H. Helmers, A. W. Bett, and M. Topič, "Comprehensive electrical loss analysis of monolithic interconnected multi-segment laser power converters," *Progress in Photovoltaics: Research and Applications*, vol. 27, no. 3, pp. 199–209, 2019.

USC
UNIVERSIDADE
DE SANTIAGO
DE COMPOSTELA

Appendix A

Published works

A.1 Journal articles in this thesis

A.1.1 Laser Power Converter Architectures Based on 3C-SiC with Efficiencies >80%

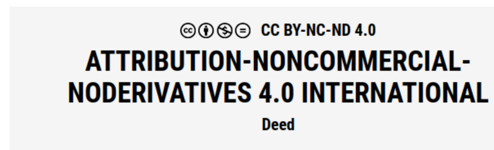
CC BY-NC-ND 4.0

ATTRIBUTION-NONCOMMERCIAL-NODERIVATIVES 4.0 INTERNATIONAL

Deed

Canonical URL : https://creativecommons.org/licenses/by-nc-nd/4.0/

See the legal code

You are free to:

Share — copy and redistribute the material in any medium or format

The licensor cannot revoke these freedoms as long as you follow the license terms.

Under the following terms:

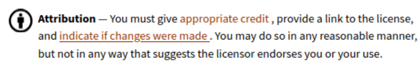
Attribution — You must give appropriate credit , provide a link to the license, and indicate if changes were made . You may do so in any reasonable manner, but not in any way that suggests the licensor endorses you or your use.

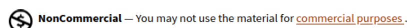
NonCommercial — You may not use the material for commercial purposes .

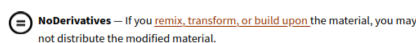
NoDerivatives — If you remix, transform, or build upon the material, you may not distribute the modified material.

No additional restrictions — You may not apply legal terms or technological measures that legally restrict others from doing anything the license permits.

USC UNIVERSIDADE DE SANTIAGO DE COMPOSTELA

- Publication quality indicators:
  - Impact factor (JCR 2022): 7.9
  - Quartile: Q1
  - Category: MATERIALS SCIENCE, MULTIDISCIPLINARY
  - Rank: 71/344
- PhD candidate contribution:
  - Data curation.
  - Investigation.
  - Writing – original draft.

USC UNIVERSIDADE DE SANTIAGO DE COMPOSTELA

Check for updates

Laser Power Converter Architectures Based on 3C-SiC with Efficiencies >80%

Javier F. Lozano, Natalia Seoane, Enrique Comesaña, Florencia Almonacid, Eduardo F. Fernández, and Antonio García-Loureiro*

High power laser transmission technology is based on energy transfer through a monochromatic laser onto a photovoltaic receiver avoiding the limitations of conventional wiring. Current technology, headed by GaAs-based devices, faces two limitations: the intrinsic entropic losses and the degradation at high input power densities due to ohmic losses. Two novel laser power converters focused on overcoming these limitations are proposed. 3C-SiC is used as base material because of its high bandgap (2.36 eV) and its excellent crystallographic properties in order to reduce the entropic losses. Also, the current decreases due to the inherent flux reduction of high energy photons. To minimize ohmic losses, a recently proposed vertical architecture is explored, which can significantly reduce series resistance around two orders of magnitude (≈10^{-5} Ω cm^2). Furthermore, 3C-SiC is also implemented in a conventional horizontal architecture to show the advantage of increasing the energy gap to reduce the ohmic losses. The two laser power converters obtain efficiencies above the state-of-the-art (87.4% at 3000 W cm^{-2} for the vertical architecture and 81.1% at 100 W cm^{-2} for the horizontal architecture) Taking this into account, the new devices open a new route for ultrahigh efficiency remote powered systems.

1. Introduction

High power laser transmission (HPLT) has been pointed as a key development in the emerging technology of wireless power transfer (WPT)[1] which has become an increasingly profitable market.[2] HPLT is based on the emission of monochromatic light to transfer energy to a remote photovoltaic device or laser power converter (LPC). In this sense, HPLT represents a paradigm shift with the possibility of transferring around a hundred watts of power density to several kilometers distance without using wires. The technology allows to overcome the limitations of conventional wiring because it provides electrical isolation and a reduction of electromagnetic interference and electrical noise.[3] Applications of this technology include, among others, dual transmission of power and data,[4,5] and optical powering of Internet-of-Things devices,[6] remote antennas,[7] aerial vehicles[8,9] and satellites.[10,11]

The LPC state-of-the-art is mostly based on III–V compounds, being GaAs the most used material.[12] Multiple studies have achieved efficiencies over 50% using GaAs-based LPCs.[13–25] In fact, the current experimental record set by Helmers et al.[21] has an efficiency of 68.9% under an input power density of 11.4 W cm^{-2} with a single GaAs cell. However, the efficiency of this device suffers from degradation with increasing input power density due to ohmic losses. This is a relevant constrain of current HPLT technology as it strongly limits the amount of power density to be transferred to the remote system. In order to overcome this limitation, Outes et al.[22] proposed a new architecture through numerical simulations, a GaAs-based vertical tunnel junction which achieves efficiencies of more than 76% at 3000 W cm^{-2}. The benefits of this architecture are no shadowing effects from the front metal grid and a very low series resistance (≈10^{-5} Ω cm^2).

Although this vertical architecture may mitigate the efficiency degradation at high input power densities, the advancement of the current LPC technology is hindered by the properties of the base materials employed. There are several studies reporting that the maximum efficiency achievable for a material increases with its bandgap,[26,27] as high bandgap materials reduce the intrinsic entropic losses. This limits the improvement of devices based on Si (1.11 eV) and GaAs (1.43 eV). High bandgap materials have been recently pointed as the key to develop a new generation of ultraefficient LPCs.[28]

Among the wide bandgap semiconductors, silicon carbide (SiC) has been extensively researched and commercialized in

J. F. Lozano, N. Seoane, E. Comesaña, A. García-Loureiro
Centro Singular de Investigación en Tecnoloxías de Información (CiTiUS)
Departament of Electrónica e Computación
Universidade de Santiago de Compostela
15782 Santiago de Compostela, Spain

F. Almonacid, E. F. Fernández
Advances in Photovoltaic Technology (AdPVTech)
CEACTEMA
University of Jaén
23071 Jaén, Spain
E-mail: fenandez@ujaen.es

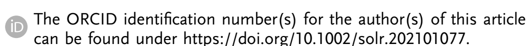
The ORCID identification number(s) for the author(s) of this article can be found under https://doi.org/10.1002/solr.202101077.

© 2022 The Authors. Solar RRL published by Wiley-VCH GmbH. This is an open access article under the terms of the Creative Commons Attribution-NonCommercial-NoDerivs License, which permits use and distribution in any medium, provided the original work is properly cited, the use is non-commercial and no modifications or adaptations are made.

DOI: 10.1002/solr.202101077

USC UNIVERSIDADE DE SANTIAGO DE COMPOSTELA

the last two decades, mostly due to its application in power electronics.[29] SiC is found in several polytypes, being the hexagonal 4H and 6H the most employed so far.[30] Efforts are being made to obtain high-quality cubic 3C crystals because of the high electron mobility and isotropic properties,[31] and the fact that 3C can be grown on large commercially available Si wafers, notably reducing fabrication costs.[32] SiC has not been considered for solar PV applications due to its high energy gap and poor solar spectrum absorption.[33] However, this material becomes very interesting in the context of laser power converters due to the properties previously mentioned. Despite of this, to the date, it has not been investigated as an alternative to current LPC technologies and its actual potential remains unknown.

In this work, we study the feasibility of 3C-SiC as a base material for LPC for the first time. We employ two different architectures, a conventional horizontal laser power converter (hLPC) and a vertical laser power converter (vLPC), based on the structure proposed by Outes et al.[22]. We carried out a series of optimizations for both architectures under several input power densities (P_{in}) with the aim to enhance the LPC efficiencies. The simulation procedure is based on Silvaco Atlas,[34] a trustable and well-known TCAD tool, widely employed for accurate simulations of semiconductors performance. We have considered all the relevant phenomena in order to achieve reliable results and the material properties are taken from an exhaustive literature review based on experimental data. This work is intended to show the potential of this material to produce a new generation of low-cost and high-efficiency LPCs beyond current state-of-the-art technologies.

2. Devices and Simulation

In this section we present the two architectures considered, as well as the simulation framework applied in this work, which includes the TCAD software and the models being used.

2.1. Device Architectures

We investigate the feasibility of 3C-SiC as a promising material for LPC through two different architectures shown in **Figure 1**: hLPC and vLPC. The single unit structure of both LPCs consists of four layers with p+/p/n/n+ doping types. The third dimension (depth) does not affect the carrier transport and density, and it is set to 1 μm without loss of generality in order to save computational costs. The depth of the devices is only limited by fabrication issues and as some of 3C-SiC processes are very similar to those of the Si, these are well known and commonly industrialized. We apply total transmittance for the incident light in the illumination area, emulating the behavior of an antireflective coating.

In the hLPC the incident light is parallel to the current flow and perpendicular to the anode and cathode. In this architecture, there is a trade-off between the optical path and the carrier diffusion length, as the absorption and transport processes take place in the same direction. To avoid an excessively long device in which the minority carriers do not survive, a textured reflective layer is placed at the bottom of the structure. This layer increases the optical path, greatly enhancing light absorption and photon recycling.[35]

In the vLPC, the incident light is perpendicular to the current flow and parallel to the anode and cathode. This architecture shows a drastic reduction of series resistance and the absence of shadowing due to the metal grid.[36–38] Another interesting feature is the possibility to connect several devices via tunnel junctions to increase the illumination area.[36] This could be achieved by monolithically growing multiple subcells on the top of each other, as in standard multijunction concentrator solar cells. In this sense, the viability of stacking up to 30 p/n junctions has already been proven.[39,40] Another method to increase the illumination area is via the arrangement of a multisegment series connection.[41]

2.2. Simulation Framework

This work was carried out using Silvaco Atlas Software,[34] a TCAD simulator able to provide realistic and trustable results when modeling a wide variety of electronic devices, including photovoltaic solar cells. For instance, Michael et al.[42] applied it in the design and optimization of a III–V multijunction, Ochoa et al.[43] improved the efficiency of a multijunction

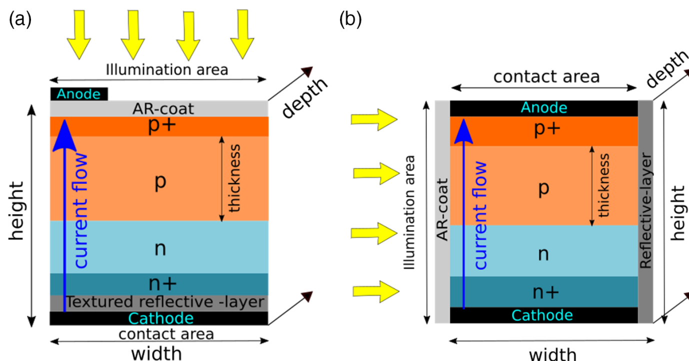

Figure 1. 2D single unit schemes of the a) hLPC and b) vLPC architectures. The third dimension of the two architectures (depth) is set to 1 μm. AR-coat is the antireflective coating.

© 2022 The Authors. Solar RRL published by Wiley-VCH GmbH

2367198x, 2022, 8, Downloaded from https://onlinelibrary.wiley.com/doi/10.1002/solr.202101077 by Consorcio Interuniversitario Do Sistema Universitario De Galicia (Cisug), Wiley Online Library on [06/06/2024]. See the Terms and Conditions (https://onlinelibrary.wiley.com/terms-and-conditions) on Wiley Online Library for rules of use; OA articles are governed by the applicable Creative Commons License

USC UNIVERSIDADE DE SANTIAGO DE COMPOSTELA

concentrator under 5000 suns by optimizing the window layer and Seoane et al.[38] studied a vertical tunnel junction under 15 000 suns. ATLAS was also applied to design and optimize vertical laser power converters by Outes et al.,[22] and to evaluate the impact of design variables in a vertical epitaxial heterostructure architecture (VEHSA) LPC by York et al.[44]

In this work, Poisson and continuity equations were solved to obtain the main properties and characteristics of each device configuration. To realistically emulate the behavior of silicon carbide, we use the Caughey–Thomas model to describe carrier mobilities with doping density dependence,[45] a suitable model when a low electrical field is accounted.[46] Carrier mobility (μ) is expressed as

$$\mu = \mu_{\min} + \frac{\mu_{\max} - \mu_{\min}}{1 + (N/N_{\text{ref}})^{\alpha}} \tag{1}$$

where $\mu_{\max}$ and $\mu_{\min}$ are the mobilities of pure and high doped crystal, respectively, N is the doping level, N_{ref} is the doping level at which the mobility is in an intermediate value between $\mu_{\min}$ and $\mu_{\max}$, and α is a fitting parameter. **Table 1** shows the mobility parameters used in this work.

We consider Shockley–Read–Hall (SRH) and Auger recombinations. After a preliminary study, we have found that the contribution of radiative recombination has no relevance because the radiative coefficient for 3C-SiC is an order of magnitude smaller than that of Si[48,49]; and therefore it has not been included in the simulations.

SRH recombination is considered the main recombination process in indirect bandgap semiconductors.[50] The SRH recombination rate ($R_{\text{net}}^{\text{SRH}}$) with doping dependence is expressed as follows

$$R_{\text{net}}^{\text{SRH}} = \frac{np - n_i^2}{\tau_p\left(n + n_i \exp\frac{E_{\text{trap}}}{k_B T_L}\right) + \tau_n\left(p + n_i \exp\frac{-E_{\text{trap}}}{k_B T_L}\right)} \tag{2}$$

where

$$\tau_{n,p} = \frac{\tau_0}{1 + \left(\frac{N}{N_{\text{norm}}}\right)^{\gamma}} \tag{3}$$

n and p are the electron and hole concentrations, n_i is the intrinsic carrier concentration, which is negligible for 3C-SiC at room temperature,[46] E_{trap} is the difference between the trap energy level and the intrinsic Fermi level, k_B is the Boltzmann constant, T_L is the lattice temperature, $\tau_{n,p}$ is the effective electrons and holes lifetimes, τ_0 is the longest lifetime observed in undoped crystal, N_{norm} is a doping concentration which operates as a normalization constant, and γ is a fitting parameter.[51,52] We use $E_{\text{trap}} = 0$, which corresponds to the most efficient recombination centers.[34] Although carrier lifetimes in SiC heavily depend on the crystal growth conditions, under low injection levels, lifetimes of up to 15 μs in 3C-SiC bulk are reported in the literature.[31] At low illumination levels, SRH dominates the recombinations because there are a large number of traps available. However, an increase in the input power density leads to higher SRH lifetimes due to a lower percentage of vacant traps compared to the excess carrier concentration.[53] To account for this effect, we increase the τ_0 lifetime with the excess carrier concentration following the trend observed in Hayashi et al.[54] We apply, for hole lifetimes, $\tau_p = \tau_n/5$, which is an usual relation in silicon and SiC.[55]

The Auger recombination rate (R_{Auger}) is determined by the following expression

$$R_{\text{Auger}} = C_n(pn^2 - nn_i^2) + C_p(np^2 - pn_i^2) \tag{4}$$

where C_n and C_p are the Auger experimental coefficients for a given material.[56] **Table 2** shows the set of recombination parameters used in this work. A remarkable characteristic of 3C-SiC is its small Auger coefficient, an order of magnitude less than that of Si and 4H-SiC,[57,58] and two orders of magnitude lower than in GaAs.[59] This is beneficial at high injection levels, when this recombination mechanism is predominant.[53]

In this study we consider bandgap narrowing with doping dependence and ideal surface passivation. All simulations were performed at a constant temperature of 298 K. The absorption coefficient with incident wavelength dependence is taken from experimental data.[60]

3. Results and Discussion

We initially present the optimization results for the hLPC and vLPC architectures under several P_{in} values and, at the end of the section, compare the efficiency of the proposed LPCs against that of several state-of-the-art devices. Optimization is performed by a multivariable iterative process, varying the parameters (layer thicknesses, doping concentrations, device width, incident wavelength) in discrete steps with the target of increasing the

Table 1. 3C-SiC mobility parameters for electrons and holes, extracted from refs. [32,47]. $\mu_{\max}$ and $\mu_{\min}$ are the mobilities of pure and high doped crystal respectively, N_{ref} is the doping level at which the mobility is in an intermediate value between $\mu_{\min}$ and $\mu_{\max}$, and α is a fitting parameter.

Mobility parameters			
Mobility model	Parameter	Electrons	Holes
Caughey–Thomas	$\mu_{\max}$ [cm^2 Vs^{-1}]	900	70
	$\mu_{\min}$ [cm^2 Vs^{-1}]	40	15
	N_{ref} [cm^{-3}]	1.5×10^{17}	5×10^{19}
	α	0.8	0.3

Table 2. 3C-SiC recombination parameters used during the simulations, extracted from refs. [31,55,58]. N_{norm} is a reference doping level which operates as a normalization constant, E_{trap} is the difference between the trap energy level and the intrinsic Fermi level, γ is a fitting parameter, and C is the Auger experimental coefficient.

Recombination parameters			
Recombination model	Parameter	Electrons	Holes
Shockley–Read–Hall	N_{norm} [cm^{-3}]	1×10^{17}	1×10^{17}
	γ	0.3	0.3
	E_{trap}	0	0
Auger	C	3×10^{-32}	2×10^{-32}

© 2022 The Authors. Solar RRL published by Wiley-VCH GmbH

2367198x, 2022, 8, Downloaded from https://onlinelibrary.wiley.com/doi/10.1002/solr.202101077 by Consorcio Interuniversitario De Sistema Universitario De Galicia (Cisug), Wiley Online Library on [06/06/2024]. See the Terms and Conditions (https://onlinelibrary.wiley.com/terms-and-conditions) on Wiley Online Library for rules of use; OA articles are governed by the applicable Creative Commons License

USC UNIVERSIDADE DE SANTIAGO DE COMPOSTELA

efficiency. The p+ and n+ layers are initially optimized, finding that their optimal values are a 40 nm thickness and 5×10^{19} cm^{-3} doping concentration for all the hLPC devices, and a 50 nm thickness and 8×10^{19} cm^{-3} doping concentration for all the vLPC devices studied. Next, we optimize the p and n layers thicknesses and doping concentrations. In the hLPC, we set the device width to 10 µm because no surface recombination is accounted in this work as first step, avoiding perimeter recombination sources, and the generation and transport processes occur in the vertical direction. However, in the vLPC, the width of the device needs to be considered. As the depth (the third dimension) does not affect the efficiency of these devices, both architectures can scale in that direction, increasing the illumination area and thus the incident power to the desired values as much as manufacturing processes allow it. The optimum incident wavelength is 525 nm for all the studied devices.

3.1. hLPC Optimization Results

Table 3 shows the optimum device structure and the main figures of merit that characterize the hLPC behavior, i.e., the short-circuit current (I_{SC}), the short-circuit current density (J_{SC}), the quantum efficiency (QE), the open-circuit voltage (V_{OC}), the voltage at the maximum power point (V_{MP}), the fill factor (FF), and the device efficiency (η). J_{SC} is obtained from dividing I_{SC} by the electrical contact area of the hLPC (the width of the device times the depth). For the lower P_{in} values ranging from 1 to 100 W cm^{-2}, the optimal layer thickness varies between 65 and 70 µm for the *p*-layer and is 9 µm for the n-layer. For 1000 and 3000 W cm^{-2}, the thickness is reduced to 49 and 40 µm, respectively, in the *p*-layer and to 6 µm in the *n*-layer. The optimum *p*-layer doping concentration increases with P_{in}, ranging from 5×10^{16} cm^{-3} at 1 W cm^{-2} to 1×10^{18} cm^{-3} at 3000 W cm^{-2}, while the n-layer doping concentration is 1×10^{14} cm^{-3} for all the P_{in} values studied.

Figure 2 shows the normalized *I–V* curves for the hLPC architecture. At P_{in} values ranging from 1 to 100 W cm^{-2}, the effect of the series resistance is not relevant, becoming noticeable at

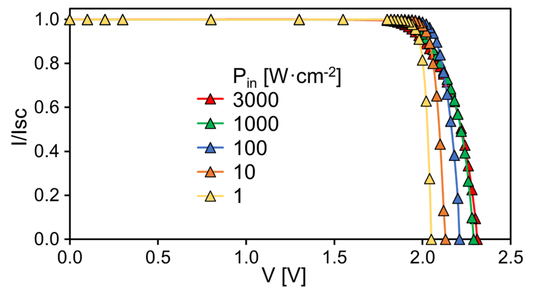

Figure 2. *I–V* curves, normalized to each I_{SC}, for various optimized input power densities (P_{in}) in the hLPC. The incident wavelength is 525 nm for all the P_{in} values.

1000 W cm^{-2} and significantly degrading the performance of the hLPC at higher P_{in} values.

QE is almost constant for the lower P_{in} values, slightly decreasing at 1000 and 3000 W cm^{-2} mainly due to Auger recombination. Also, although V_{OC} increases over the whole range of illumination, V_{MP} does not follow this trend, reaching a peak at 100 W cm^{-2} and then decreasing at higher P_{in} values. This can be mainly attributed to the series resistance, which produces a continuous decrease in FF from 92.7% at 1 W cm^{-2} to 80.3% at 3000 W cm^{-2}. The efficiency grows with the P_{in} from a 77.5% at 1 W cm^{-2} until it reaches a maximum of 81.1% at 100 W cm^{-2} and then, as a result of the increase of series resistance and Auger recombination, it decreases to 73.6% at 3000 W cm^{-2}.

3.2. vLPC Optimization Results

Table 4 shows the optimum device dimensions and main figures of merit. As the illumination area changes with the optimization processes, the total input power in the different vLPC structures may vary. The QE is a useful parameter in order to perform a fair comparison of these devices. Optimum *p*-layer remains at 51 µm

Table 3. hLPC optimization results and figures of merit for different input power densities (pin) values. The *p*- and *n*-layer thickness and doping concentrations are optimized. The I_{SC}, J_{SC}, QE, V_{OC}, V_{MP}, FF, and η are shown. The incident wavelength is 525 nm for all the pin values.

P_{in} [W cm^{-2}]		1		10		100		1000		3000	
Optimized structure	Layer	Thick [µm]	Doping [cm^{-3}]	Thick [µm]	Doping [cm^{-3}]	Thick [µm]	Doping [cm^{-3}]	Thick [µm]	Doping [cm^{-3}]	Thick [µm]	Doping [cm^{-3}]
	p	65	5×10^{16}	70	1×10^{17}	65	3×10^{17}	49	5×10^{17}	40	1×10^{18}
	n	9	1×10^{14}	9	1×10^{14}	9	1×10^{14}	6	1×10^{14}	6	1×10^{14}
	Width [µm]	10		10		10		10		10	
	J_{SC} [mA cm^{-2}]	4.08×10^{2}		4.10×10^{3}		4.10×10^{4}		4.06×10^{5}		1.19×10^{6}	
	QE	0.964		0.968		0.968		0.958		0.936	
	V_{OC} [V]	2.05		2.13		2.21		2.29		2.31	
	V_{MP} [V]	1.92		1.98		2.02		1.94		1.92	
	FF [%]	92.7		91.8		89.3		82.8		80.3	
	η [%]	77.5		80.0		81.1		76.9		73.6	

© 2022 The Authors. Solar RRL published by Wiley-VCH GmbH

2367198x, 2022, 8, Downloaded from https://onlinelibrary.wiley.com/doi/10.1002/solr.202101077 by Consorcio Interuniversitario Do Sistema Universitario De Galicia (Cisug), Wiley Online Library on [06/06/2024]. See the Terms and Conditions (https://onlinelibrary.wiley.com/terms-and-conditions) on Wiley Online Library for rules of use; OA articles are governed by the applicable Creative Commons License

USC UNIVERSIDADE DE SANTIAGO DE COMPOSTELA

2367198x, 2022, 8, Downloaded from https://onlinelibrary.wiley.com/doi/10.1002/solr.202101077 by Consorcio Interuniversitario De Sistema Universitario De Galicia (Cisug), Wiley Online Library on [06/06/2024]. See the Terms and Conditions (https://onlinelibrary.wiley.com/terms-and-conditions) on Wiley Online Library for rules of use; OA articles are governed by the applicable Creative Commons License

Table 4. vLPC optimization results and figures of merit for different input power densities (pin). The *p*- and n-layer thickness and doping concentrations are optimized, as well as the vLPC width (see Figure 1b)). The I_{SC}, J_{SC}, QE, V_{OC}, V_{MP}, FF, and η are shown. The incident wavelength is 525 nm for all the P_{in} values.

P_{in} [W [cm]$^{-2}$]		1		10		100		1000		3000	
Optimized structure	Layer	Thick [μm]	Doping [cm^{-3}]	Thick [μm]	Doping [cm^{-3}]	Thick [μm]	Doping [cm^{-3}]	Thick [μm]	Doping [cm^{-3}]	Thick [μm]	Doping [cm^{-3}]
	p	51	5×10^{16}	51	5×10^{16}	42	3×10^{17}	27	5×10^{17}	18	5×10^{17}
	n	1	1×10^{17}	1	1×10^{17}	1	1×10^{16}	1	1×10^{16}	0.1	1×10^{16}
	Width [μm]	360		360		360		360		360	
	J_{SC} [mA cm^{-2}]	6.42×10^{1}		6.09×10^{2}		5.33×10^{3}		3.29×10^{4}		6.39×10^{4}	
	QE	0.988		0.994		0.992		0.994		0.995	
	V_{OC} [V]	2.04		2.10		2.16		2.21		2.23	
	V_{MP} [V]	1.92		1.98		2.04		2.08		2.10	
	FF [%]	93.2		93.2		93.3		93.0		92.9	
	η [%]	79.7		82.5		84.8		86.6		87.4	

for the two lower P_{in} values, and for 100, 1000, and 3000 W cm^{-2} is reduced by a 17.6%, 47.1%, and 64.7%, respectively. As the P_{in} increases, SRH recombination saturates, and Auger recombination mechanism becomes more relevant. Given that the thickness of the layers in the vertical architecture modifies the illumination area, the optimal thickness tends to shrink with increasing P_{in} in order to reduce the carrier concentration and thus Auger recombination. *N*-layer optimum thickness is 1 μm for all the P_{in} values except for 3000 W cm^{-2}, where it decreases to 0.1 μm. The optimum *p*-layer doping increases one order of magnitude over the entire P_{in} range, as the n-layer doping decreases by one order of magnitude. The total width of the device remains at 360 μm for all the P_{in} values studied. As in the vertical architecture there is no trade-off between photon absorption and carrier transport, the width of the device is independent of illumination and is adjusted for optimal absorption.

Figure 3 shows the vLPC normalized *I–V* curves for the P_{in} studied range. Note that for this architecture there is not any noticeable degradation due to series resistance at any P_{in} value, unlike in the hLPC. QE values are similar for all vLPCs, reflecting a steady internal conversion between incident photon-collected pair. V_{OC} and V_{MP} grow linearly with the logarithmic increase of P_{in}. FF is around 93% for all optimizations, indicating almost negligible series resistance losses. Efficiency grows linearly with the logarithmic increase of P_{in} for the studied range. This result, opposed to the behavior in the hLPC, comes from low series resistance and the lesser presence of Auger recombination in the vLPC architecture. Note that, the carrier density is lower in the vLPC architecture than in the hLPC because the absorption is made along the entire width of the device without photon recycling.

Comparing the two architectures, the QE is greater in the vLPC for all the P_{in} values studied, and no degradation appears in this parameter, in contrast to what happens in the hLPC. This is due to the regulation of incident light in the vLPC by the thickness of the layers, managing the excess carrier concentration and thus Auger recombination. **Figure 4** shows V_{OC} and V_{MP} for the hLPC and vLPC under several P_{in} values. For the two architectures, V_{MP} has similar values and grows linearly with the

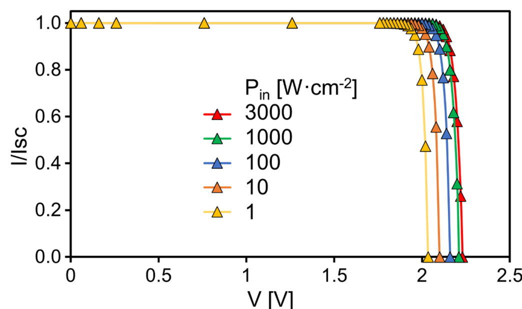

Figure 3. *I–V* curves, normalized to each I_{SC}, for the input power densities (P_{in}) optimized in the vLPC architecture. The incident wavelength is 525 nm for all the P_{in} values.

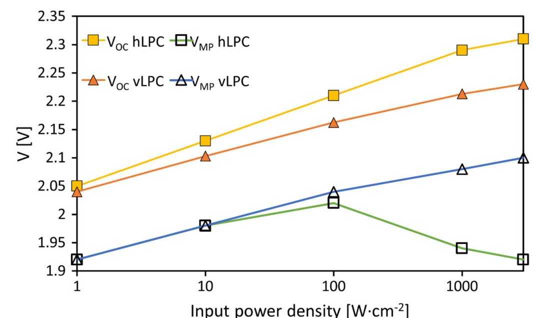

Figure 4. V_{OC} and V_{MP} dependence on input power density (P_{in}) for the hLPC and vLPC architectures. The incident wavelength is 525 nm for all cases.

© 2022 The Authors. Solar RRL published by Wiley-VCH GmbH
USC UNIVERSIDADE DE SANTIAGO DE COMPOSTELA

2367198x, 2022, 8, Downloaded from https://onlinelibrary.wiley.com/doi/10.1002/solr.202101077 by Consorcio Interuniversitario Do Sistema Universitario De Galicia (Cisug), Wiley Online Library on [06/06/2024]. See the Terms and Conditions (https://onlinelibrary.wiley.com/terms-and-conditions) on Wiley Online Library for rules of use; OA articles are governed by the applicable Creative Commons License

logarithm of the P_{in} at low illumination rates. This progression continues in the vLPC for larger illumination rates, while in the hLPC a degradation of the FF and the V_{MP} appears at 100 W cm^{-2} and above due to series resistance. V_{OC} also grows linearly with the logarithm of the P_{in} in both architectures until Auger recombination affects this parameter at extreme P_{in} values above 1000 W cm^{-2}. However, the vLPC shows a lower dependence on this phenomenon, as already commented. Indeed, the increasing rate of the V_{OC} for the hLPC up to 1000 W cm^{-2} is around 8%, while it is only around 6% (2% lower) above this value. On the contrary, the vLPC shows an increasing rate up to this value of around 6%, while it is only reduced to 5% (1% lower) above this P_{in} value. This also contributes to increasing the efficiency of the vLPC converter with P_{in} in a larger amount. In any case, these results also indicate that Auger recombination is not expected to limit the development of 3C-SiC converters for HPLT applications.

As can be also seen in this figure, the V_{OC} values for the vLPC architecture are lower when compared to those of the hLPC. This can be explained considering the decrease in photogeneration rate across the device width. In the hLPC, there is a trade-off between light absorption and carrier diffusion length. Indeed, a textured back layer is required to increase the optical absorption without drastically increase the recombination losses. This leads to high carrier concentration and therefore to a higher V_{OC}. In the vLPC, there is no such trade-off, as the light absorption occurs in a perpendicular direction to the current flow. This produces better absorption by enlarging the width of the device without affecting the carrier diffusion (see Figure 1). Due to the large width of the vLPCs (360 μm), the photogeneration rate decreases by one order of magnitude through the device. The collected charge, and therefore the V_{OC}, diminishes as light goes deeper into the vLPC. As the anode and cathode cover the entire width of the device, the overall V_{OC} value will correspond to the voltage in the area with less illumination. Therefore, the width of the vLPC must reach a compromise between being large enough to ensure the absorption of most of the beam and maintaining sufficient excess carrier densities to avoid V_{OC} degradation in the least illuminated areas.

3.3. Comparative with State-of-the-Art LPCs

Figure 5 shows the efficiency as a function of P_{in} for the LPCs studied in this work and for several experimental and simulated state-of-the-art LPCs available in the literature. The values shown in the figure corresponding to this work are for the optimum structures at each P_{in}. The state-of-the-art LPCs shown here are GaAs or AlGaAs/GaAs based, which is the current standard technology. Helmers et al.[21] have achieved a remarkable efficiency of 68.9% at 11.4 W cm^{-2} with the implantation of an optical cavity that minimizes transmission and thermalization losses. This is the highest efficiency achieved by an experimental LPC, and the largest for P_{in} values below 100 W cm^{-2}. The performance of their horizontal LPC is degraded at higher irradiances than 11.4 W cm^{-2} due to ohmic losses, decreasing to 59.3% at 76.6 W cm^{-2}. In order to allow higher power to be transferred, other horizontal designs, such as the VEHSA architecture, presented by York et al.,[24] implement the strategy of stacking multiple thin photovoltaic semiconductor subcells on the top of each other to divide current, and therefore reduce the series resistance losses, achieving efficiencies of 66% at 64.6 W cm^{-2}.

From our proposed architectures, the 3C-SiC hLPC shows a remarkable efficiency between 10 and 100 W cm^{-2}, which could be considered the typical operating range of LPCs. This hLPC, optimized at 10 W cm^{-2}, achieves a 80.0% efficiency, improving

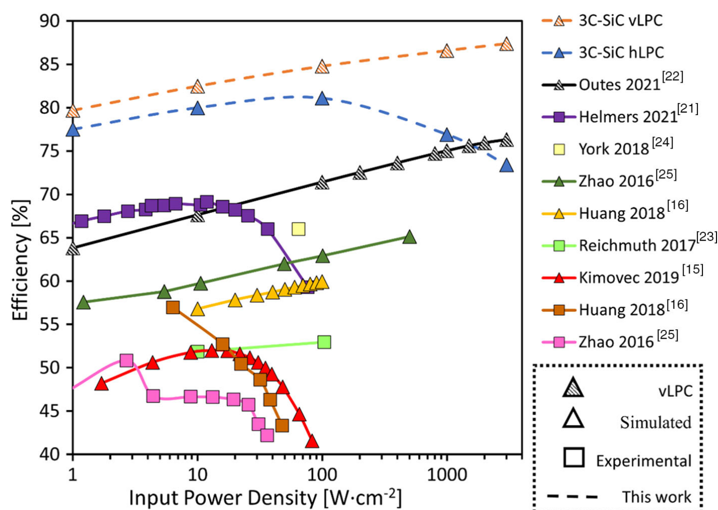

Figure 5. Efficiency versus input power density for present work and several state-of-the-art LPCs. vLPC and hLPC refer to the 3C-SiC architectures studied in this work. The LPCs shown correspond to Kimovec,[15] Huang,[16] Helmers[21] (illumination area of 0.054 cm^2), Outes,[22] Reichmuth,[23] York,[24] and Zhao.[25]

© 2022 The Authors. Solar RRL published by Wiley-VCH GmbH

USC UNIVERSIDADE DE SANTIAGO DE COMPOSTELA

the current record of Helmers et al.[21] by 11.1%, and increases to 81.1% at 100 W cm^{-2}, exceeding by 9.7% the efficiency reported by the Outes et al.[22] simulated vLPC. At higher P_{in} values, like other horizontal LPCs, it suffers a decrease in efficiency due to growing series resistance losses and Auger recombination. However, the efficiency over all the analyzed P_{in} range is higher than that of the other state-of-the-art horizontal LPCs and the efficiency degradation is less abrupt, resulting in a 7.7% efficiency reduction from 100 to 3000 W cm^{-2}. Although the results above are expected to be lower for a real 3C-SiC hLPC device due to additional losses related to manufacturing constraints, e.g., shunt losses, surface recombination, etc., these results are promising to motivate further investigation on the development of highly efficiency novel LPCs based on 3C-SiC. Also, it is important to remark that the fabrication of 3C-SiC based devices is expected to be cheaper and more environmentally friendly than GaAs-based ones because it involves fewer toxic agents[61] and the fabrication processes have excellent compatibility with those used in Si, employing the same fab lines.

The 3C-SiC vLPC efficiency is higher than that of the 3C-SiC hLPC for all the P_{in} range studied, exceeding its efficiency in the typical operating range by a 2.5% at 10 W cm^{-2}, and by a 3.7% at 100 W cm^{-2}. At higher P_{in} values the vertical architecture does not appear to be limited by series resistance, as efficiency keeps growing linearly with the logarithm of P_{in}. The results of the 3C-SiC vLPC are also compared with those of the GaAs-based vLPC introduced by Outes et al.,[22] which established the previous efficiency record for a modeled LPC at high P_{in} values, achieving a 76.3% efficiency at 3000 W cm^{-2}. The 3C-SiC vLPC shows an extremely high efficiency of 87.4% at 3000 W cm^{-2}, increasing by 11.1% the result achieved by Outes et al. at this P_{in} value. This is noteworthy because the methodology used in Outes et al. is essentially the same than the one followed in his work. Hence, the difference in the results could mainly be attributed to the reduction of the current due to a lower photon flux density and more favorable materials properties of 3C-SiC compared to those of GaAs.

Possible limitations to this technology may arise from the manufacturing side, related to the illumination area. The device area of the state-of-the-art fabricated LPCs is 0.9 mm^2 for Reichmuth et al.,[23] around 3 mm^2 for Huang et al.[16] and Kimovec et al.,[15] 5.4 mm^2 for Helmers et al.,[21] and 11.3 mm^2 for Zhao et al.[25] In the hLPC architecture, the illumination area is defined by the width and depth of the device. As previously mentioned, we chose in this work a 1 μm depth for both architectures in order to save computational costs, and a 10 μm width in the hLPC single unit for the same reason. As the size of 3C-SiC wafers is around 200 mm,[62] the hLPC width and depth dimensions can be scaled up and consequently, the active area of this architecture can be in the order of cm^2 if needed. Hence, it would be possible to achieve the same areas than the state-of-the-art LPCs without manufacturing restrictions. In the case of the vLPC, the illumination area is determined by the depth and height of the device. As the depth can be scaled without performance degradation, the active area of a single vLPC unit, assuming a standard square geometry, is mainly limited by the optimum height, which is also going to depend on the incident power density. For instance, the total height is around 20 μm for an optimum vLPC unit at a P_{in} value of 3000 W cm^{-2}. This height could be small to achieve similar illumination areas to the state-of-the-art LPCs. However, this dimension can be increased through vertically stacking multiple tunnel junctions (VEHSA), as done in Fafard et al.[20] Indeed, it has been possible to vertically stack 30 units using tunnel junctions.[39] Taking this into account, the height of the vLPC device could be increased to around 0.6 mm. As commented, the depth can be scaled accordingly, achieving a total square 0.6 mm × 0.6 mm active area device, which is comparable to those of the state-of-the-art LPCs. These dimensions are also recommended because the goal of this architecture is to manage very high input power densities. Hence, an active area of less than 1 mm × 1 mm is recommended to reduce the heat waste and facilitate the thermal management.[63] Note that in the vLPC architecture the junctions are parallel to the light flow, and several identical single units can be vertically stacked without changing their structure, in order to obtain the same current in each single unit, so without increasing the series resistance losses.[22,38] This simplifies the design and makes it robust against temperature variations (due to change in energy gap and photon absorption), compared to the VEHSA architecture. Finally, it is important to mention that the active area of both architectures can be further increased if needed by arranging the single units onto a series/parallel-connected module.[15,64]

As previously commented, although the efficiency of 3C-SiC-based experimental LPCs could be reduced due to unexpected manufacturing issues, the simulation results indicate that this material opens a new promising route to improve the efficiency of current and future LPCs.

4. Conclusions

We have proposed cubic silicon carbide as base material for LPC because of its high bandgap and excellent crystalline properties. To study its suitability, we have considered two different architectures, a hLPC and a vLPC, whose design allows a reduction in series resistance. The devices are investigated by performing simulations with a TCAD software up to 3000 W cm^{-2}. In this work, the temperature is assumed to be constant and equal to 298 K, as the reference air temperature in the PV field. The increase of the temperature with the input power density and its effects on the device's performances are crucial for this technology to succeed, and many factors are involved (e.g., efficiency, area, thermal resistance, medium temperature, etc.).These effects were no considered at this stage of the investigation, although they will be carefully studied in future works.

Results show that, for both architectures, silicon carbide-based LPCs have better performance than GaAs-based LPCs in the whole illumination range studied. The 3C-SiC hLPC shows an efficiency of 81.1% at 100 W cm^{-2}, exceeding the current state-of-the-art record efficiency for hLPCs by 12.2%. Although at higher irradiances the performance of the 3C-SiC hLPC is degraded due to increasing series resistance and Auger recombination, the downgrading is less abrupt than in other hLPCs in the literature, indicating better performance at high injection levels.

The 3C-SiC vLPC improves the results of the state-of-the-art vLPCs by 11.1%, showing an efficiency of 87.4% at 3000 W.

© 2022 The Authors. Solar RRL published by Wiley-VCH GmbH

2367198x, 2022, 8, Downloaded from https://onlinelibrary.wiley.com/doi/10.1002/solr.202101077 by Consorcio Interuniversitario Do Sistema Universitario De Galicia (Cisug), Wiley Online Library on [06/06/2024]. See the Terms and Conditions (https://onlinelibrary.wiley.com/terms-and-conditions) on Wiley Online Library for rules of use; OA articles are governed by the applicable Creative Commons License

USC UNIVERSIDADE DE SANTIAGO DE COMPOSTELA

The 3C-SiC vLPC shows no degradation over the entire power range studied, due to extremely low series resistance and a significantly reduced Auger recombination with respect to hLPC. As these mechanisms do not affect the device performance, the 3C-SiC vLPC exhibits a linear growth of efficiency with the logarithm of input power density, allowing room for improvement at higher powers.

Although the performance of real LPCs based on 3C-SiC can be affected by manufacturing issues, these results support that 3C-SiC could be a promising candidate to replace GaAs as the base material for high-efficiency LPCs for all input power range.

Acknowledgements

This work was supported by the Spanish Government, Xunta de Galicia, Junta de Andalucía, and FEDER funds (grant nos. PID2019-106497RB-I00, P18- RT-1595, PID2019-104834GB-I00, ED431F 2020/008, GRC 2014/008, RYC-2017-23312, and RYC-2017-21910).

Conflict of Interest

The authors declare no conflict of interest.

Data Availability Statement

The data that support the findings of this study are available from the corresponding author upon reasonable request.

Keywords

3C-SiC, high power densities, laser power converters, vertical structures, wireless power transfer

Received: December 22, 2021
Revised: March 28, 2022
Published online: May 1, 2022

[1] K. Jin, W. Zhou, *IEEE Trans. Power Electron.* **2019**, *34*, 3842.
[2] X. Lu, P. Wang, D. Niyato, D. I. Kim, Z. Han, *IEEE Commun. Surv. Tutorials* **2016**, *18*, 1413.
[3] D. Krut, R. Sudharsanan, W. Nishikawa, T. Isshiki, J. Ermer, N. H. Karam, *Conf. Record of the IEEE Photovoltaic Specialists Conf.* **2002**, p. 908.
[4] M. Matsuura, H. Nomoto, H. Mamiya, T. Higuchi, D. Masson, S. Fafard, *IEEE Trans. Power Electron.* **2021**, *36*, 4532.
[5] H. Helmers, C. Armbruster, M. Von Ravenstein, D. Derix, C. Schoner, *IEEE Trans. Power Electron.* **2020**, *35*, 7904.
[6] P. D. Diamantoulakis, G. K. Karagiannidis, Z. Ding, *IEEE Trans. Green Commun. Networking* **2018**, *2*, 764.
[7] C. Vázquez, J. D. López-Cardona, P. C. Lallana, D. S. Montero, F. M. A. Al- Zubaidi, S. Pérez-Prieto, I. Pérez Garcilópez, *IEEE Access* **2019**, *7*, 158409.
[8] N. Kawashima, K. Takeda, H. Matsuoka, Y. Fujii, M. Yamamoto, in *22nd Int. Symp. on Automation and Robotics in Construction*, Ferrara, September 2005.
[9] T. Blackwell, *AIP Conf. Proc.* **2005**, *766*, 73.
[10] D. Shi, L. Zhang, H. Ma, Z. Wang, Y. Wang, Z. Cui, in *2016 IEEE Wireless Power Transfer Conf.*, Aveiro, May 2016.
[11] M. Sanders, J. S. Kang, *IEEE Aerospace Conf. Proc.*, IEEE, Piscataway, NJ **2020**, p. 1.
[12] J. Schubert, E. Oliva, F. Dimroth, W. Guter, R. Loeckenhoff, A. W. Bett, *IEEE Trans. Electron Devices* **2009**, *56*, 170.
[13] A. N. Panchak, P. V. Pokrovskiy, D. A. Malevskiy, V. R. Larionov, M. Z. Shvarts, *Tech. Phys. Lett.* **2019**, *45*, 24.
[14] H. Helmers, L. Wagner, C. E. Garza, S. K. Reichmuth, E. Oliva, S. Philipps, D. Lackner, A. Bett, in *Proc. SENSOR 2015*, Wunstorf, **2015**.
[15] R. Kimovec, H. Helmers, A. W. Bett, M. Topič, *Prog. Photovoltaics Res. Appl.* **2019**, *27*, 199.
[16] J. Huang, Y. Sun, Y. Zhao, S. Yu, J. Dong, J. Xue, C. Xue, J. Wang, Y. Lu, Y. Ding, *J. Semicond.* **2018**, *39*, 044003.
[17] T. Shan, X. Qi, *Infrared Phys. Technol.* **2015**, *71*, 144.
[18] R. Sudharsanan, D. Krut, T. Isshiki, H. Cotal, S. Mesropian, A. Masalykin, N. H. Karam, in *2008 IEEE LEOS Annual Meeting Conf. Proceedings*, Newport Beach, November 2008.
[19] L. C. Olsen, D. A. Huber, G. Dunham, F. W. Addis, *Conf. Rec. IEEE Photovoltaics Spec. Conf.* **1992**, *1*, 419.
[20] S. Fafard, F. Proulx, M. C. A. York, L. S. Richard, P. O. Provost, R. Arès, V. Aimez, D. P. Masson, *Appl. Phys. Lett.* **2016**, *109*, 131107.
[21] H. Helmers, E. Lopez, O. Höhn, D. Lackner, J. Schön, M. Schauerte, M. Schachtner, F. Dimroth, A. W. Bett, *Phys. Status Solidi RRL* **2021**, *15*, 1.
[22] C. Outes, E. F. Fernandez, N. Seoane, F. Almonacid, A. J. Garcia-Loureiro, *IEEE Electron Device Lett.* **2021**, *42*, 1882.
[23] S. K. Reichmuth, H. Helmers, S. P. Philipps, M. Schachtner, G. Siefer, A. W. Bett, *Prog. Photovoltaics Res. Appl.* **2017**, *25*, 67.
[24] M. C. A. York, A. Mailhot, A. Boucherif, R. Arès, V. Aimez, S. Fafard, *Sol. Energy Mater. Sol. Cells* **2018**, *181*, 46.
[25] Y. Zhao, Y. Sun, Y. He, S. Yu, J. Dong, *Sci. Rep.* **2016**, *6*, 1.
[26] E. Oliva, F. Dimroth, A. W. Bett, *Prog. Photovoltaics Res. Appl.* **2008**, *16*, 289.
[27] M. Lin, W. E. I. Sha, W. Zhong, D. Xu, *Appl. Phys. Lett.* **2021**, *118*, 1.
[28] E. F. Fernández, A. García-Loureiro, N. Seoane, F. Almonacid, *Sol. Energy Mater. Sol. Cells* **2022**, *235*, 111483.
[29] X. She, A. Q. Huang, O. Lucia, B. Ozpineci, *IEEE Trans. Ind. Electron.* **2017**, *64*, 8193.
[30] J. N. Shenoy, J. A. Cooper, M. R. Melloch, *IEEE Electron Device Lett.* **1997**, *18*, 93.
[31] I. G. Ivanov, R. Liljedahl, R. Yakimova, M. Syväjärvi, *Appl. Phys. Lett.* **2012**, *100*, 252101.
[32] A. E. Arvanitopoulos, M. Antoniou, S. Perkins, M. Jennings, M. B. Guadas, K. N. Gyftakis, N. Lophitis, *IEEE Trans. Ind. Appl.* **2019**, *55*, 4080.
[33] M. Syväjärvi, Q. Ma, V. Jokubavicius, A. Galeckas, J. Sun, X. Liu, M. Jansson, P. Wellmann, M. Linnarsson, P. Runde, B. A. Johansen, A. Thøgersen, S. Diplas, P. A. Carvalho, O. M. Løvvik, D. N. Wright, A. Y. Azarov, B. G. Svensson, *Sol. Energy Mater. Sol. Cells* **2016**, *145*, 104.
[34] Silvaco, https://www.silvaco.com.
[35] M. A. Green, J. Zhao, A. Wang, S. R. Wenham, *IEEE Electron Device Lett.* **1992**, *13*, 317.
[36] E. F. Fernandez, N. Seoane, F. Almonacid, A. J. Garcia-Loureiro, *IEEE Electron Device Lett.* **2018**, *40*, 1.
[37] C. Outes, E. F. Fernández, N. Seoane, F. Almonacid, A. J. García-Loureiro, *Sol. Energy* **2020**, *203*, 136.
[38] N. Seoane, E. F. Fernández, F. Almonacid, A. García-Loureiro, *Prog. Photovoltaics Res. Appl.* **2021**, *29*, 231.
[39] S. Fafard, D. P. Masson, *J. Appl. Phys.* **2021**, *130*, 160901.
[40] S. Fafard, D. Masson, J. G. Werthen, J. Liu, T. C. Wu, C. Hundsberger, M. Schwarzfischer, G. Steinle, C. Gaertner, C. Piemonte, B. Luecke, J. Wittl, M. Weigert, *Energies* **2021**, *14*, 1.

© 2022 The Authors. Solar RRL published by Wiley-VCH GmbH

2367198x, 2022, 8, Downloaded from https://onlinelibrary.wiley.com/doi/10.1002/solr.202101077 by Consorcio Interuniversitario Do Sistema Universitario De Galicia (Cisug), Wiley Online Library on [06/06/2024]. See the Terms and Conditions (https://onlinelibrary.wiley.com/terms-and-conditions) on Wiley Online Library for rules of use; OA articles are governed by the applicable Creative Commons License

USC UNIVERSIDADE DE SANTIAGO DE COMPOSTELA

[41] L. Wagner, S. K. Reichmuth, S. P. Philipps, E. Oliva, A. W. Bett, H. Helmers, *Prog. Photovoltaics Res. Appl.* **2021**, *29*, 172.
[42] S. Michael, A. Bates, *Sol. Energy Mater. Sol. Cells* **2005**, *87*, 785.
[43] M. Ochoa, E. Barrigón, L. Barrutia, I. García, I. Rey-Stolle, C. Algora, *Prog. Photovoltaics Res. Appl.* **2016**, *24*, 1332.
[44] M. C. A. York, S. Fafard, *J. Phys. D. Appl. Phys* **2017**, *50*, 173003.
[45] D. M. Caughey, R. E. Thomas, *Proc. IEEE* **1967**, *55*, 2192.
[46] A. Arvanitopoulos, N. Lophitis, K. N. Gyftakis, S. Perkins, M. Antoniou, *Semicond. Sci. Technol.* **2017**, *32*, 1.
[47] F. La Via, A. Severino, R. Anzalone, C. Bongiorno, G. Litrico, M. Mauceri, M. Schoeler, P. Schuh, P. Wellmann, *Mater. Sci. Semicond. Process.* **2018**, *78*, 57.
[48] P. Ščajev, M. Karaliūnas, E. Kuokštis, K. Jarašiūnas, *J. Lumin.* **2013**, *134*, 588.
[49] W. Gerlach, H. Schlangenotto, H. Maeder, *Phys. Status Solidi* **1972**, *13*, 277.
[50] G. L. Harris, *Properties of Silicon Carbide*, INSPEC, Institution of Electrical Engineers, London **1995**.
[51] M. E. Law, E. Solley, M. Liang, D. E. Burk, *IEEE Electron Device Lett.* **1991**, *12*, 401.
[52] W. Shockley, W. T. Read, *Phys. Rev.* **1952**, *87*, 835.
[53] A. Vossier, B. Hirsch, J. M. Gordon, *Appl. Phys. Lett.* **2010**, *97*, 0.
[54] T. Hayashi, K. Asano, J. Suda, T. Kimoto, *Mater. Sci. Forum* **2010**, *645–648*, 199.
[55] M. Ruff, H. Mitlehner, R. Helbig, *IEEE Trans. Electron Devices* **1994**, *41*, 1040.
[56] J. Dziewior, W. Schmid, *Appl. Phys. Lett.* **1977**, *31*, 346.
[57] J. D. Beck, R. Conradt, *Solid State Commun.* **1973**, *13*, 93.
[58] A. Arvanitopoulos, N. Lophitis, S. Perkins, K. N. Gyftakis, M. Belanche Guadas, M. Antoniou, in *2017 IEEE 11th Inter. Symp. on Diagnostics for Electrical Machines, Power Electronics and Drives*, Tinos, August 2017.
[59] U. Strauss, W. W. Rühle, K. Köhler, *Appl. Phys. Lett.* **1993**, *62*, 55.
[60] L. Patrick, W. J. Choyke, *Phys. Rev.* **1969**, *186*, 775.
[61] H. Joël Tchognia Nkuissi, F. Kouadio Konan, B. Hartiti, J.-M. Ndjaka, *Reliab. Ecol. Asp. Photovolt. Modul.* **2020**, 1.
[62] M. Schoeler, P. Schuh, G. Litrico, F. La Via, M. Mauceri, P. J. Wellmann, *Adv. Mater. Proc.* **2017**, *2*, 774.
[63] L. Micheli, E. F. Fernández, F. Almonacid, T. K. Mallick, G. P. Smestad, *Sol. Energy Mater. Sol. Cells* **2016**, *153*, 164.
[64] C. Algora, I. García, M. Delgado, R. Peña, C. Vázquez, M. Hinojosa, I. Rey- Stolle, *Joule* **2021**, *6*, 340.

© 2022 The Authors. Solar RRL published by Wiley-VCH GmbH

2367198x, 2022, 8, Downloaded from https://onlinelibrary.wiley.com/doi/10.1002/solr.202101077 by Consorcio Interuniversitario Do Sistema Universitario De Galicia (Cisug), Wiley Online Library on [06/06/2024]. See the Terms and Conditions (https://onlinelibrary.wiley.com/terms-and-conditions) on Wiley Online Library for rules of use; OA articles are governed by the applicable Creative Commons License

USC UNIVERSIDADE DE SANTIAGO DE COMPOSTELA

A.1.2 Photogeneration and Performance Optimization (PhPO): A New Algorithm to Improve the Performance of Vertical Epitaxial Hetero-Structure Architecture Laser Power Converters

ATTRIBUTION 4.0 INTERNATIONAL

Deed

Canonical URL : https://creativecommons.org/licenses/by/4.0/

See the legal code

You are free to:

Share — copy and redistribute the material in any medium or format for any purpose, even commercially.

Adapt — remix, transform, and build upon the material for any purpose, even commercially.

The licensor cannot revoke these freedoms as long as you follow the license terms.

- Publication quality indicators:
  - Impact factor (JCR 2023): 3.4
  - Quartile: Q2
  - Category: ENGINEERING, ELECTRICAL ELECTRONIC
  - Rank: 122/352
- PhD candidate contribution:

USC UNIVERSIDADE DE SANTIAGO DE COMPOSTELA

- Data curation.
- Investigation.
- Software development
- Writing – original draft.

USC
UNIVERSIDADE
DE SANTIAGO
DE COMPOSTELA

IEEE Access
Multidisciplinary | Rapid Review | Open Access Journal

Received 26 June 2023, accepted 28 July 2023, date of publication 8 August 2023, date of current version 14 August 2023.
Digital Object Identifier 10.1109/ACCESS.2023.3302523

RESEARCH ARTICLE

Photogeneration and Performance Optimization (PhPO): A New Algorithm to Improve the Performance of Vertical Epitaxial Hetero-Structure Architecture Laser Power Converters

JAVIER F. LOZANO[1], NATALIA SEOANE[1], ENRIQUE COMESAÑA[2], (Member, IEEE), FLORENCIA M. ALMONACID[3], EDUARDO F. FERNÁNDEZ[3], AND ANTONIO GARCÍA-LOUREIRO[1], (Member, IEEE)
[1]Centro Singular de Investigación en Tecnoloxías Intelixentes (CiTiUS), Departamento de Electrónica e Computación, University of Santiago de Compostela, 15782 Santiago de Compostela, Spain
[2]Escola Politécnica Superior de Enxeñaría, Campus Terra, University of Santiago de Compostela, 27002 Lugo, Spain
[3]Advances in Photovoltaic Technology (AdPVTech), CEACTEMA, University of Jaén, 23071 Jaén, Spain

Corresponding author: Javier F. Lozano (javier.fernandez.lozano@rai.usc.es)

This work was supported in part by the Spanish Government, in part by Xunta de Galicia, in part by Junta de Andalucía, and in part by Fondo Europeo de Desarrollo Regional (FEDER) Funds under Grant PID2019-106497RB-I00, Grant P18-RT-1595, Grant PID2019-104834GB-I00, Grant ED431F 2020/008, Grant ED431C 2022/16, Grant RYC-2017-23312, Grant RYC-2017-21910, and Grant PID2022-141623NB-I00.

ABSTRACT The state of the art in the field of high-power laser transmission is dominated by the so called Vertical Epitaxial Hetero-Structure Architecture (VEHSA), which consists of monolithically stacking p/n cells connected by tunnel junctions. This configuration distributes the current between the cells and reduces the losses due to Joule heating. Since assessing the performance of each individual cell is very challenging, the design and optimization of these devices relies on simple approximations based on the Beer-Lambert law, the exponential decay of light, and guessing from published data. The limitations of these approaches are i) the current of each cell may differ from the calculated photocurrent, producing a mismatch and limiting the overall current, ii) the design parameters cannot be individually evaluated, and iii) the loss of accuracy when applied to devices with light trapping mechanisms. In this work, we present a novel optimization methodology aimed to overcome these limitations, based on a meticulous device Technology Computer-Aided Design (TCAD) and an iterative optimization algorithm with two stages: Photogeneration and Performance Optimization (PhPO). The proposed procedure improves the performance of the current state-of-the-art VEHSA devices, allows the use of new semiconductors and makes the design more resilient to a wide range of operation conditions.

INDEX TERMS Device modeling, new algorithm, laser power converters, VEHSA architecture, photo-current optimization, multijunction photovoltaic devices.

I. INTRODUCTION

The high power laser transmission (HPLT) technology has been pointed as a key development in the wireless power transfer (WPT) field [1]. It consists of transmitting power through a monochromatic light to a remote photovoltaic device, or laser power converter (LPC). This technology has the advantage of providing electrical isolation and avoiding electromagnetic interference [2], replacing traditional copper wires when security restrictions require the absence of sparks. Such is the case for workplaces under an ATEX directive, like refineries or mines where there is risk of fire or explosion [3].

The associate editor coordinating the review of this manuscript and approving it for publication was Marcelo Antonio Pavanello.

This work is licensed under a Creative Commons Attribution 4.0 License. For more information, see https://creativecommons.org/licenses/by/4.0/

USC UNIVERSIDADE DE SANTIAGO DE COMPOSTELA

Dual transmission of power and data [4], [5] and optically powering satellites [6], [7] or aerial vehicles [8], [9] are other possible applications of this technology. Another remarkable aspect is the possibility of deliver power through optic fiber or wireless transmission through free space [3].

Current state-of-the-art LPC devices exceed 60% efficiency values at room temperature [10], [11]. The base materials used are mostly III-V compounds, being GaAs the preferred one [12], since it achieves efficiencies much larger than LPCs based on Si [13] or InGaAsP/InP [14]. Multijunction GaAs LPCs are particularly noteworthy [15], as well as devices with enhanced photon recycling and treatment of thermalization losses [11]. New advances in photovoltaics provide hints for future efficiency improvements, such as new architectures [16], [17], [18], [19] or the use of materials with fewer limitations [20].

The Vertical Epitaxial Hetero-Structure Architecture (VEHSA) stands out among the multijunction LPCs. This arrangement consists of monolithically stacking p/n tunnel junctions [10], which is also the main pathway to achieve ultra-high efficiencies on concentrating photovoltaic solar cells [21]. The major advantage of this architecture is to distribute the current over the p/n junctions, which reduces Joule heating losses. This allows to operate under high laser power concentrations, increasing the efficiency due to the open circuit voltage (V_{oc}) enhancement associated with higher carrier concentration. The V_{oc} also benefits from a greater Fermi level splitting in thin layers [22]. However, the optimization of VEHSA devices is challenging because of the extreme difficulty of evaluating its individual cell currents. Up to date, the optimization is mainly done by simple approximations using the Beer-Lambert law [23], which only accounts for the photogeneration of each cell. This method is only meaningful to VEHSA devices made of well-known direct bandgap materials like GaAs, since design parameters like doping values and relative p/n sizes are extrapolable from published data [24] and the light decays exponentially in the bulk of the device, as no light-trapping mechanisms are needed. Nevertheless, not measuring the currents of each cell hinders the current matching and the optimization of design parameters, reducing the performance of the device. Although new optimizations paths have been described in literature, such as including tabulated quantum efficiency values in the photogenerated current estimation [25], [26], more sophisticated optimization techniques that broaden the range of VEHSAs are missing. This is of particular interest in the context of materials with indirect high-bandgap like silicon carbide, which has been identified as a potential new route to ultra-high efficiency LPCs [27].

In this paper we propose a new universal methodology to optimize the design of VEHSA devices. The procedure, based on combining device modeling with a multistage optimization algorithm, allows not only to further optimize state-of-the-art VEHSAs, but also opens the door to design and optimize new multijunction devices. This feature skips many trial and error processes when manufacturing novel VEHSA devices, considerably reducing costs. This methodology is valid for both direct or indirect bandgap materials, regardless of whether they are powered by laser or by sunlight.

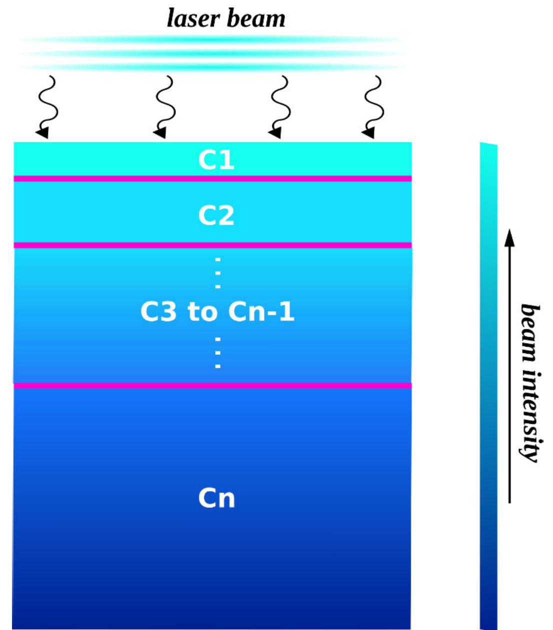

FIGURE 1. Exponential decay of light intensity, according to Beer-Lambert law. To accurately match the photocurrents, the integrated photogeneration must be the same in all cells.

II. METHODOLOGY

In this section we present the main limitations in the design of state-of-the-art VEHSA devices, and we introduce an optimization method to improve their performance via a meticulous current matching and the improvement of the individual efficiency of each cell.

A key factor that affects the performance of VEHSA devices is the precise matching of the currents produced by every cell, since the total current drawn from the device will be the lowest of all the contributing cells. Up to date, the state-of-the-art VEHSAs achieve current matching by applying the Beer-Lambert law, the exponential light decay [23]. The integrated photogeneration must be the same in all cells, as illustrated in **Figure 1:**

$$I_{i+1}(\lambda) = I_i e^{-\alpha(\lambda) t_i} \tag{1}$$

where I_i and I_{i+1} are the light intensities entering and leaving the i-th layer, respectively. t_i is the thickness of the i-th layer and $\alpha(\lambda)$ the wavelength dependent absorption coefficient. This is a good approximation for direct-gap VEHSA devices, as the photogeneration can be calculated very accurately. However, this method does not take into account the performance of each cell, so there will be

USC UNIVERSIDADE DE SANTIAGO DE COMPOSTELA

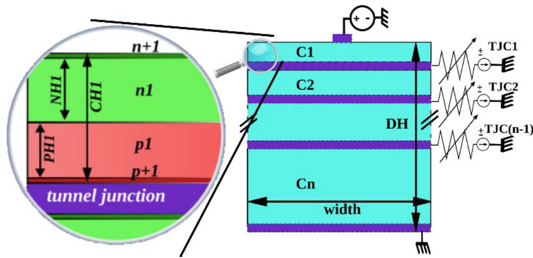

FIGURE 2. 2D-Schematic of a VEHSA device. The variable resistances in tunnel junctions allow to extract the current diferences from the adjacent cells. C1, C2, …, Cn are the cells of the VEHSA device. The zoom-in shows the detailed structure of the cell C1, composed by n+/n/p/p+ layers, with a CH1 total height. PH1 and NH1 are the heights of C1 p and n layers, respectively.

differences between the photogenerated current and the total current contributed. To avoid this issue, it has been proposed to consider the quantum efficiency, QE, of each cell to calculate the current supplied [25] as follows:

$$I_{abs} = \int \frac{dI_{avail}}{d\lambda} \cdot QE(\lambda) \cdot (1 - T(\lambda) - R(\lambda))d\lambda \quad (2)$$

where I_{abs} and I_{avail} are the absorbed and available photocurrents, R the reflectance, and T the transmittance. This has the advantage of considering beam reflection and transmission, and recombination effects, which are implicit in QE. However, it misses relevant effects such as photon recycling, which is shown to be important in the modeling of GaAs VEHSA devices [28].

These approaches generally provide good results, but the performance worsens as the number of cells increases, due to the current mismatch. The actual record efficiency for a VEHSA at room temperature is achieved by a 5-cell device, reaching a 66.3% [10], and the efficiency consistently decreases for a larger number of cells. Another disadvantage of these approximations is that they are not applicable to indirect bandgap devices that require back texturization for light trapping.

We present an optimization method aimed to overcome these issues valid for both direct or indirect bandgap VEHSAs, independently if they are powered by a laser or by solar light. The system consists of meticulous device TCAD (Technology Computer-Aided Design) of the VEHSA device combined with an iterative optimization algorithm. As modeling tunnel junctions in Silvaco can be problematic [29], we used an standard workaround that consist of modeling the tunnel junctions as perfect conductors [30], to speed-up the simulation time. In these so modeled tunnel junctions we allow the extraction of the tunnel junction currents (TJCs), coupling them to electrodes with lumped variable resistances, as seen in **Figure 2**. These resistances can take very high values to simulate the full device, to avoid current through these contacts, or low realistic values to obtain the differences between the currents produced in adjacent cells. This is a useful tool to accurately match the currents of all cells and improve the performance of the full VEHSA device.

The optimization algorithm is an iterative process involving two stages: Photogeneration and Performance Optimization (PhPO from now on), as shown in **Figure 3**. In the first step, the photogeneration loop, the total device height (DH) is optimized to absorb the largest part of the beam without unnecessarily increasing the size of the device, which will affect the carrier transport. As a first approach the Beer-Lambert law is used to obtain an initial guess. The algorithm iterates, by increasing/decreasing the DH, until two criteria are fulfilled: i) a minimum absorbed light value (photo_low), that establishes the maximum photogeneration losses allowed of the total incident light and ii) a maximum photogeneration value (photo_high), which prevents the device from growing infinitely to absorb the totality of the photons. The resulting optimum DH is then used as an input for the next stage, the performance loop.

In this second stage, the optimizer improves the performance of the cells individually. This process begins with a subroutine that iteratively evaluates the TJCs and modifies *CH1,…, CHn*, i.e. the relative sizes of each cell (see Fig' s 2 zoom-in). As the TJCs extracted are the differences between the currents of the adjacent cells, the absolute value represents their mismatch, and the sign of the current indicates which cell is limiting the performance. A negative/positive sign means that the bottom/top cell is limiting and the algorithm modifies the values of *CH1, …,CHn* to increase the limiting cells in steps normalized by the largest absolute TJC value of all tunnel junctions. This process iterates until all TJCs contribute with the same current and the value is below a certain tolerance, e.g., 1/1000 of the I_{sc} extracted in the anode. When this is achieved, the algorithm optimizes the design parameters, which are the layer relative sizes (*PHi*, *NHi*) and doping values (*PDi*, *NPi*) for every i-th cell, from 1 to n. The optimization algorithm for a single design parameter is described in **Figure 4**. The parameters are swept from an initial value (provided by a preliminary single cell optimization), one by one, with the scope of increasing the cell efficiency. If new optimum design parameters are found, a new iteration is needed, since these optimizations can change the current contributed by each cell and the currents need to be matched again. On the other hand, if during the whole cell optimization cycle no new design parameters are found, the process stops, and it is considered that all cells have achieved their maximum efficiency.

III. RESULTS

To validate our methodology we initially model a GaAs-based 5-cell VEHSA (VEHSA PT5 from now on), that is designed after the experimental device reported by Fafard et al [10], that currently holds the record breaking efficiency at room temperature. We carried the simulation with Silvaco Atlas [31], a device TCAD simulator able to provide realistic and trustable results when modeling a

USC UNIVERSIDADE DE SANTIAGO DE COMPOSTELA

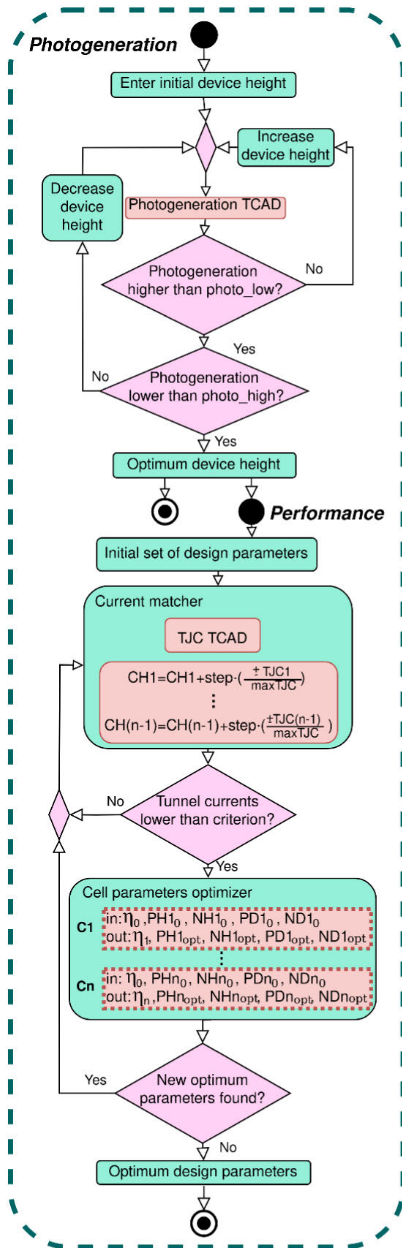

FIGURE 3. **Flowchart of the different stages of the PhPO method. Photogeneration TCAD and TJC TCAD are simulations aimed to obtain the photogeneration of each cell and the currents extracted in the tunnel junctions (TJC), respectively. The optimum device height is fixed in the photogeneration loop and used as an input to the performance loop.**

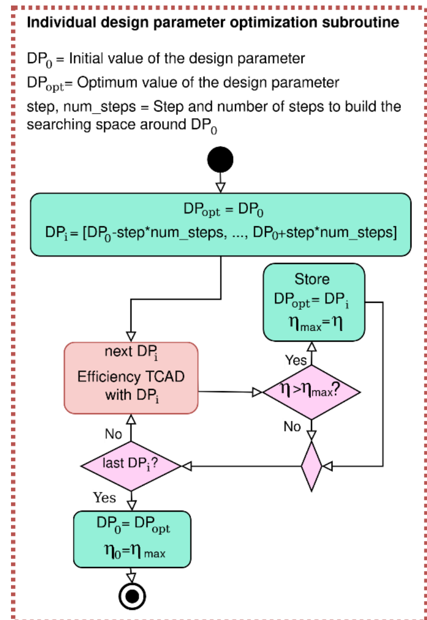

FIGURE 4. **Detailed optimization of each design parameter. Efficiency TCAD is the simulation aimed to obtain the efficiency of the evaluated cell. η_0, η, and η_{max} are the initial, latest simulated and maximum efficiencies of the evaluated cell, respectively.**

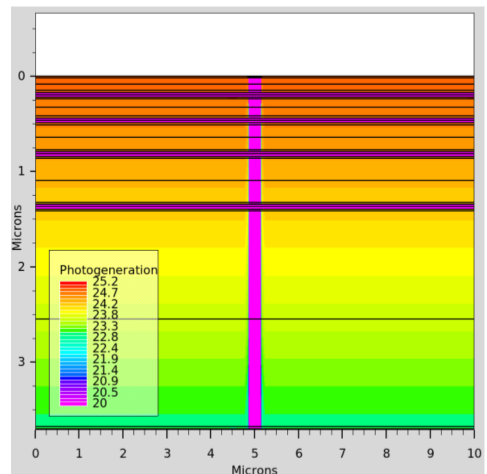

FIGURE 5. **Photogeneration rate in a VEHSA PT5.**

wide variety of devices, including photovoltaic cells [17], [32]. The Poisson and continuity equations are solved to obtain the characteristics of the device. The beam-device interaction is modelled with the ray tracing method [31] and an example of the photogeneration rate for a VEHSA PT5 is pictured in **Figure 5**. For carrier mobility we use doping concentration-dependent tabulated data, available via Silvaco. The Shockley-Read-Hall (SRH) recombination also considers the doping concentration, following experimental

USC UNIVERSIDADE DE SANTIAGO DE COMPOSTELA

data [33]. We also include optical and Auger recombinations in the simulation framework. All simulations were performed at T = 298 K. The absorption coefficient used depends on both the doping concentration and the wavelength, and fits experimental curves [34]. The material physical parameters, the incident power and the illumination area are taken from the experimental device supporting information [10]. The width of the device (see Figure 2) is fixed to 10 μm to save computational costs. Since the generation and transport processes occur in the vertical direction and no surface recombination is accounted in this work, which avoids perimeter recombination sources, this decision will not affect the behavior of the device. The contact finger (see Figure 5) covers a 3 percent of the width of the device. Given that no specific design parameters are provided for this particular experimental device, the cell heights (CH) were obtained by applying the Beer-Lambert law [23].

As the light penetrates the device, the CH values increase due to the photogeneration decay in the device, as seen in Figure 1. The CH for each cell includes the n+/n/p/p+ layers as follows: $\mathbf{CH} = \boldsymbol{h_{np+}} \, \boldsymbol{\mathcal{C}} \, \mathbf{h_{np}}$, where h_{np+} is the sum of the p+/n+ layers heights and h_{np} the sum of the n/p layer heights. The p+/n+ layers have fixed heights and doping values of 0.02 μm and $5{\cdot}10^{19}$ cm^{-3}, respectively, selected to accurately match the experimental characteristics. The n/p relative layer heights (NH/PH) are shown as a percent of h_{np} (e.g. n layer height = NH$\cdot$ h_{np}), since this value is fixed by the CH and h_{np+}. The NH/PH values are considered to be equal (0.50/0.50) [10], and the doping values (ND/PD) range from $5{\cdot}10^{17}$-$1.0{\cdot}10^{18}$ cm^{-3}, with thinner cells more heavily doped [25]. The illumination wavelength is fixed to λ =837 nm as in the experimental device. These initial parameters at room temperature are shown in **Table 1**. **Figure 6** shows a comparison between the experimental and the initial calibrated VEHSA PT5 IV curves. Note that in this figure the simulation results are scaled to the illumination area of the experimental device. The device TCAD accurately reproduces the values of I_{sc} and V_{oc} of the experimental device, and the slight differences in the shape of the curve at V_m and intermediate voltages may derive from manufacturing issues.

Once we have demonstrated the validity of our simulation methodology, we apply the PhPO method to further improve the device performance, see in Table 1 the optimized design parameters. The DH slightly increases with respect to the calibration, reaching 3.7 μm. The cell heights have been fine-tuned until the TJC mismatch is below 1/1000 the I_{sc} value of the anode. The relative NH/PH values return much larger n layer heights for thinner cells (e.g., 0.9/0.1 for the first cell), that gradually decrease as the CH increases (e.g., 0.3/0.7 for the fifth cell). The doping values significantly decrease to $1{\cdot}10^{15}$ cm^{-3}, a value three orders of magnitude lower than those observed in the initial design parameters.

The optimized IV curve is also shown in Figure 6 for comparison. The optimized VEHSA PT5 achieves the same V_{oc} as the calibrated and experimental devices and increases

TABLE 1. Design parameters (DP) for the VEHSA PT5 validation, optimization and constant values. DH and CH are the device and cell heights, NH/PH, N$^+$/P$^+$H the n/p, n$^+$/p$^+$ layer heights and ND/PD, N$^+$/P$^+$D the doping values for the n/p, n$^+$/p$^+$ layers, respectively. T is the temperature, λ the incident wavelength and CF the cover factor, which is the portion of the device covered by the contact.

DP	DH [µm]	Cell	CH [µm]	NH [%] / PH [%]	ND [cm^{-3}]	PD [cm^{-3}]
Initial	3.5	1	0.170	0.50/0.50	1e18	1e18
		2	0.218	0.50/0.50	1e18	1e18
		3	0.303	0.50/0.50	1e18	1e18
		4	0.503	0.50/0.50	1e18	1e18
		5	2.306	0.50/0.50	5e17	5e17
Optimized	3.7	1	0.175	0.90/0.10	1e15	1e15
		2	0.227	0.90/0.10	1e15	1e15
		3	0.317	0.60/0.40	1e15	1e15
		4	0.530	0.50/0.50	1e15	1e15
		5	2.450	0.30/0.70	1e15	1e15
Constant	T [K]	Width [µm]	N$^+$/P$^+$H [µm]	N$^+$/P$^+$D [cm^{-3}]	λ [nm]	CF [%]
	298	10	0.02	5e19	837	3

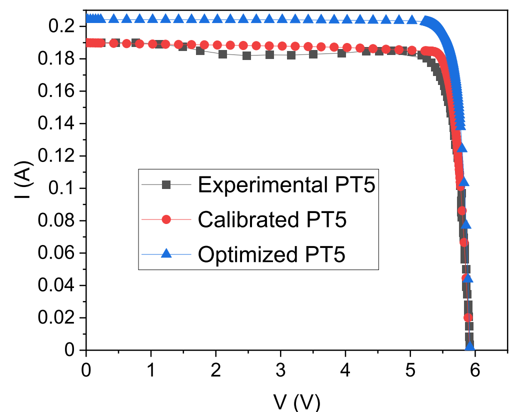

FIGURE 6. IV curves comparing the experimental [12] VEHSA PT5 against the optimized structure provided by the PhPO method. The calibrated VEHSA PT5 is also included as validation.

the I_{sc} by ≈6%, leading to a 75.8% efficiency, a value 9.5% larger than that of the experimental VEHSA PT5. These improvements are due to the meticulous current matching and individual cell optimization. This can be more clearly seen in **Figure 7** and **Figure 8**, that present the IV curves for each individual cell for the calibrated and optimized devices, respectively. Note that the calibrated VEHSA PT5 individual cell IV curves suffer from current mismatch, and there is also a noticeable V_{oc} mismatch. These effects are drastically reduced in the optimized VEHSA PT5, where the IV curves are very similar for all cells.

Given the wide variety of applications for an LPC, both aerial and terrestrial, it is worthwhile to study the impact of temperature on device performance. For that, the calibrated and optimized VEHSA PT5, are tested at three temperatures:

USC UNIVERSIDADE DE SANTIAGO DE COMPOSTELA

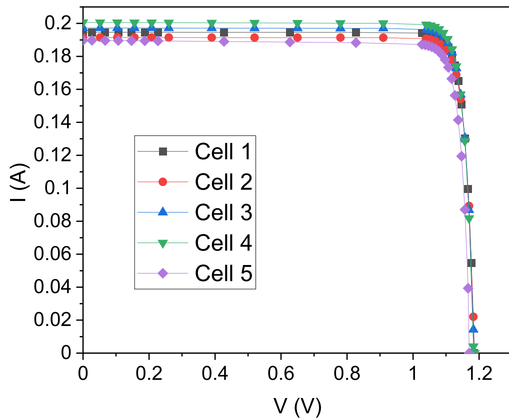

FIGURE 7. IV curves for each cell that composes the calibrated VEHSA PT5. Note that there is an appreciable dispersion in the values of I_{SC} and, to a lesser degree, in those of V_{OC}.

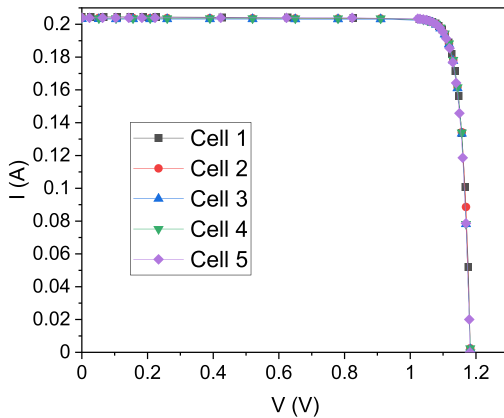

FIGURE 8. IV curves for each cell that composes the optimized VEHSA PT5. Note that, unlike in the case of the calibrated device, there is no dispersion observed in either I_{SC} or V_{OC}.

the standard laboratory conditions (298 K) and ±75 K with respect to this value (223 K and 373 K), in order to evaluate a wide range of operation. The models [35] used in the course of the simulations take into account the dependence on temperature, namely the universal energy bandgap model, SRH concentration-dependent lifetime model, Fermi statistics and power law temperature dependence mobility.

Figure 9 shows the IV curves for the optimized and calibrated VEHSAs PT5 at the three tested temperatures. Note that, although both devices reach the same V_{oc} for each temperature (due to bandgap variation), the optimized VEHSA PT5 achieves the same I_{sc} for all three temperatures tested. This is not the case for the calibrated VEHSA PT5, which suffers from loses in I_{sc} at high temperatures. This is due to the existence of higher recombinations in the experimental device, compared to the optimized one. In the

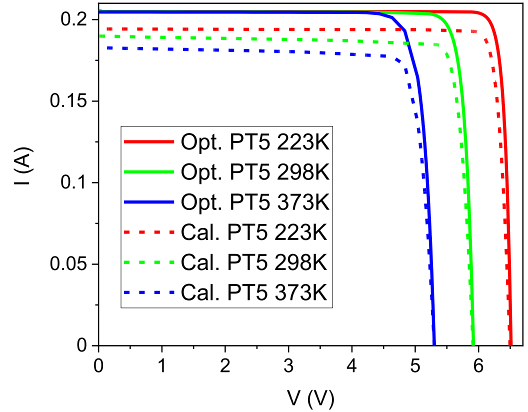

FIGURE 9. IV curves for the optimized (solid lines) and calibrated (dotted lines) VEHSA PT5 at three temperatures: 223 K (blue), 298 K (green) and 373 K (red).

calibrated VEHSA PT5, the efficiency increases/decreases a 11.3% at 223/373 K with respect to the room temperature values. The efficiency of the optimized VEHSA PT5 is slightly less affected by temperature variations, increasing/decreasing a 10.3% at 223/373 K with respect to the room temperature values, respectively. The design parameters obtained through the PhPO method applied at 298 K have considerably reduced the recombinations of the VEHSA PT5, making the device more resilient to a wide range of temperature. Note that, having a single device capable of operating over a broad temperature spectrum without major losses is desirable to avoid the need to manufacture multiple devices.

IV. CONCLUSION

We have presented a new method to optimize the design parameters of VEHSA devices, one of the most efficient architectures of state-of-the-art LPCs. The Photogeneration and Performance Optimization (PhPO) method combines device TCAD with an iterative optimization algorithm. This method is aimed to bypass the main limitations of the VEHSA architecture, namely the current mismatch between cells and the impossibility of tailoring individual cell design parameters. Traditionally, the Beer-Lambert law of exponential decay is the main available tool to match the different cells photogeneration. However, this method obtains low accuracy results when a back reflector or light-trapping mechanisms are included. Another issue related to only applying Beer-Lambert law is that the individual currents of each cell may differ, due to the different performance of the cells, leading to current mismatch.

To validate the PhPO method, we initially modelled the current room temperature record efficiency VEHSA device, a GaAs-based 5-cell reported by Fafard et al. We have accurately reproduced the experimental device IV curves at the same illumination conditions, using similar design parameters. Next, we have applied the iterative optimization algorithm to the calibrated VEHSA. The algorithm has

USC UNIVERSIDADE DE SANTIAGO DE COMPOSTELA

successfully matched all cells I_{sc} and V_{oc} values and improved each cell performance. This has led to a 9.5% efficiency increase of the optimized device with respect to the experimental VEHSA.

Given the diverse applications of LPCs, we have tested both the optimized and calibrated VEHSAs at 3 different temperatures: 223 K, 298 K and 373 K. The optimized device is slightly more resilient to temperature changes due to a reduction of the recombination effects achieved by the optimization of design parameters.

In conclusion, the PhPO method provides optimum design parameters for state-of-the-art and new generation VEHSA devices, opening a new route towards ultra-efficient VEHSAs with application to LPC and tandem solar cells, not necessarily based on direct bandgap materials.

REFERENCES

[1] K. Jin and W. Zhou, ‘‘Wireless laser power transmission: A review of recent progress,’’ *IEEE Trans. Power Electron.*, vol. 34, no. 4, pp. 3842–3859, Apr. 2019, doi: 10.1109/TPEL.2018.2853156.

[2] D. Krut, R. Sudharsanan, W. Nishikawa, T. Isshiki, J. Ermer, and N. H. Karam, ‘‘Monolithic multi-cell GaAs laser power converter with very high current density,’’ in *Proc. Conf. Rec. 29th IEEE Photovoltaic Specialists Conf.*, 2002, pp. 908–911, doi: 10.1109/pvsc.2002.1190727.

[3] C. Algora, I. García, M. Delgado, R. Peña, C. Vázquez, M. Hinojosa, and I. Rey-Stolle, ‘‘Beaming power: Photovoltaic laser power converters for power-by-light,’’ *Joule*, no. 2021, pp. 1–29, Dec. 2021, doi: 10.1016/j.joule.2021.11.014.

[4] M. Matsuura, H. Nomoto, H. Mamiya, T. Higuchi, D. Masson, and S. Fafard, ‘‘Over 40-W electric power and optical data transmission using an optical fiber,’’ *IEEE Trans. Power Electron.*, vol. 36, no. 4, pp. 4532–4539, Apr. 2021, doi: 10.1109/TPEL.2020.3027551.

[5] H. Helmers, C. Armbruster, M. von Ravenstein, D. Derix, and C. Schöner, ‘‘6-W optical power link with integrated optical data transmission,’’ *IEEE Trans. Power Electron.*, vol. 35, no. 8, pp. 7904–7909, Aug. 2020, doi: 10.1109/TPEL.2020.2967475.

[6] D. Shi, L. Zhang, H. Ma, Z. Wang, Y. Wang, and Z. Cui, ‘‘Research on wireless power transmission system between satellites,’’ in *Proc. IEEE Wireless Power Transf. Conf. (WPTC)*, May 2016, pp. 1–4, doi: 10.1109/WPT.2016.7498851.

[7] M. Sanders and J. S. Kang, ‘‘Utilization of polychromatic laser system for satellite power beaming,’’ in *Proc. IEEE Aerosp. Conf.* , 2020, pp. 1–7, doi: 10.1109/AERO47225.2020.9172561.

[8] N. Kawashima, K. Takeda, H. Matsuoka, Y. Fujii, and M. Yamamoto, ‘‘Laser energy transmission for a wireless energy supply to robots,’’ in *Proc. 22nd Int. Symp. Automat. Robot. Construct.*, Ferrara, Italy, Sep. 2005, doi: 10.22260/ISARC2005/0068.

[9] T. Blackwell, ‘‘Recent demonstrations of laser power beaming at DFRC and MSFC,’’ in *Proc. AIP Conf. Proc.*, 2005, pp. 73–85, doi: 10.1063/1.1925133.

[10] S. Fafard, F. Proulx, M. C. A. York, L. S. Richard, P. O. Provost, R. Arès, V. Aimez, and D. P. Masson, ‘‘High-photovoltage GaAs vertical epitaxial monolithic heterostructures with 20 thin p/n junctions and a conversion efficiency of 60%,’’ *Appl. Phys. Lett.*, vol. 109, no. 13, Sep. 2016, Art. no. 131107, doi: 10.1063/1.4964120.

[11] H. Helmers, E. Lopez, O. Höhn, D. Lackner, J. Schön, M. Schauerte, M. Schachtner, F. Dimroth, and A. W. Bett, ‘‘68.9% Efficient GaAs-based photonic power conversion enabled by photon recycling and optical resonance,’’ *Phys. Status Solidi, Rapid Res. Lett.*, vol. 15, no. 7, pp. 1–7, 2021, doi: 10.1002/pssr.202100113.

[12] J. Schubert, E. Oliva, F. Dimroth, W. Guter, R. Loeckenhoff, and A. W. Bett, ‘‘High-voltage GaAs photovoltaic laser power converters,’’ *IEEE Trans. Electron Devices*, vol. 56, no. 2, pp. 170–175, Feb. 2009, doi: 10.1109/TED.2008.2010603.

[13] U. Ortabasi and H. Friedman, ‘‘Powersphere: A photovoltaic cavity converter for wireless power transmission using high power lasers,’’ in *Proc. IEEE 4th World Conf. Photovoltaic Energy Conf.*, May 2006, pp. 126–129, doi: 10.1109/WCPEC.2006.279380.

[14] J. Mukherjee, S. Jarvis, M. Perren, and S. J. Sweeney, ‘‘Efficiency limits of laser power converters for optical power transfer applications,’’ *J. Phys. D, Appl. Phys.*, vol. 46, no. 26, Jul. 2013, Art. no. 264006, doi: 10.1088/0022-3727/46/26/264006.

[15] S. Fafard and D. P. Masson, ‘‘Perspective on photovoltaic optical power converters,’’ *J. Appl. Phys.*, vol. 130, no. 16, Oct. 2021, Art. no. 160901, doi: 10.1063/5.0070860.

[16] C. Outes, E. F. Fernández, N. Seoane, F. Almonacid, and A. J. García-Loureiro, ‘‘GaAs vertical-tunnel-junction converter for ultra-high laser power transfer,’’ *IEEE Electron Device Lett.*, vol. 42, no. 12, pp. 1882–1885, Dec. 2021, doi: 10.1109/led.2021.3121501.

[17] N. Seoane, E. F. Fernández, F. Almonacid, and A. García-Loureiro, ‘‘Ultra-efficient intrinsic-vertical-tunnel-junction structures for next-generation concentrator solar cells,’’ *Prog. Photovolt., Res. Appl.*, vol. 29, no. 2, pp. 231–237, Feb. 2021, doi: 10.1002/pip.3369.

[18] C. Outes, E. F. Fernández, N. Seoane, F. Almonacid, and A. J. García-Loureiro, ‘‘Numerical optimisation and recombination effects on the vertical-tunnel-junction (VTJ) GaAs solar cell up to 10,000 suns,’’ *Sol. Energy*, vol. 203, pp. 136–144, Jun. 2020, doi: 10.1016/j.solener.2020.04.029.

[19] E. F. Fernandez, N. Seoane, F. Almonacid, and A. J. Garcia-Loureiro, ‘‘Vertical-tunnel-junction (VTJ) solar cell for ultra-high light concentrations (>2000 suns),’’ *IEEE Electron Device Lett.*, vol. 40, no. 1, pp. 167–170, Dec. 2018, doi: 10.1109/LED.2018.2880240.

[20] J. F. Lozano, N. Seoane, E. Comesaña, F. Almonacid, E. F. Fernández, and A. García-Loureiro, ‘‘Laser power converter architectures based on 3C-SiC with efficiencies 80%,’’ *Sol. RRL*, vol. 6, no. 8, Aug. 2022, Art. no. 2101077, doi: 10.1002/solr.202101077.

[21] S. P. Philipps and A. W. Bett, ‘‘III-V multi-junction solar cells and concentrating photovoltaic (CPV) systems,’’ *Adv. Opt. Technol.*, vol. 3, nos. 5–6, pp. 469–478, Dec. 2014, doi: 10.1515/aot-2014-0051.

[22] Y. Cui, D. van Dam, S. A. Mann, N. J. J. van Hoof, P. J. van Veldhoven, E. C. Garnett, E. P. A. M. Bakkers, and J. E. M. Haverkort, ‘‘Boosting solar cell photovoltage via nanophotonic engineering,’’ *Nano Lett.*, vol. 16, no. 10, pp. 6467–6471, Oct. 2016, doi: 10.1021/acs.nanolett.6b02971.

[23] D. Masson, F. Proulx, and S. Fafard, ‘‘Pushing the limits of concentrated photovoltaic solar cell tunnel junctions in novel high-efficiency GaAs phototransducers based on a vertical epitaxial heterostructure architecture,’’ *Prog. Photovolt., Res. Appl.*, vol. 23, no. 12, pp. 1687–1696, Dec. 2015, doi: 10.1002/pip.2709.

[24] M. C. A. York, F. Proulx, D. P. Masson, A. Jaouad, B. Bouzazi, R. Arès, V. Aimez, and S. Fafard, ‘‘Thin n/p GaAs junctions for novel high-efficiency phototransducers based on a vertical epitaxial heterostructure architecture,’’ *MRS Adv.*, vol. 1, no. 14, pp. 881–890, 2016, doi: 10.1557/adv.2016.9.

[25] M. C. A. York, A. Mailhot, A. Boucherif, R. Arès, V. Aimez, and S. Fafard, ‘‘Challenges and strategies for implementing the vertical epitaxial heterostructure architechture (VEHSA) design for concentrated photovoltaic applications,’’ *Sol. Energy Mater. Sol. Cells*, vol. 181, pp. 46–52, Jul. 2018, doi: 10.1016/j.solmat.2017.11.034.

[26] S. Čičić and S. Tomić, ‘‘Genetic algorithm designed high efficiency laser power converters based on the vertical epitaxial heterostructure architecture,’’ *Sol. Energy Mater. Sol. Cells*, vol. 200, Sep. 2019, Art. no. 109878, doi: 10.1016/j.solmat.2019.03.050.

[27] E. F. Fernández, A. García-Loureiro, N. Seoane, and F. Almonacid, ‘‘Band-gap material selection for remote high-power laser transmission,’’ *Sol. Energy Mater. Sol. Cells*, vol. 235, Jan. 2022, Art. no. 111483, doi: 10.1016/j.solmat.2021.111483.

[28] M. C. A. York, F. Proulx, D. P. Masson, A. Jaouad, B. Bouzazi, R. Arès, V. Aimez, and S. Fafard, ‘‘Enhanced photocarrier extraction mechanisms in ultra-thin photovoltaic GaAs n/p junctions,’’ *Phys., Simul. Photonic Eng. Photovoltaic Devices*, vol. 9743, Mar. 2016, Art. no. 97430Y, doi: 10.1117/12.2212960.

[29] M. H. Tsutagawa and S. Michael, ‘‘Triple junction InGaP/GaAS/Ge solar cell optimization: The design parameters for a 36.2% efficient space cell using silvaco ATLAS modeling & simulation,’’ in *Proc. 34th IEEE Photovoltaic Spec. Conf. (PVSC)*, Jun. 2009, pp. 001954–001957, doi: 10.1109/PVSC.2009.5411544.

[30] R. J. Kilway II, ‘‘Five-junction solar cell optimization using Silvaco Atlas,’’ Thesis, Naval Postgraduate School, Monterey, CA, USA, Sep. 2017. [Online]. Available: https://archive.org/details/fivejunctionsola1094556146

USC UNIVERSIDADE DE SANTIAGO DE COMPOSTELA

[31] Silvaco. (2020). *Silvaco software (version 5.30.0.R)*. [Online]. Available: https://www.silvaco.com
[32] M. Ochoa, E. Barrigón, L. Barrutia, I. García, I. Rey-Stolle, and C. Algora, "Limiting factors on the semiconductor structure of III-V multijunction solar cells for ultra-high concentration (1000-5000 suns)," *Prog. Photovolt., Res. Appl.*, vol. 24, no. 10, pp. 1332–1345, Oct. 2016, doi: 10.1002/pip.2791.
[33] G. B. Lush, H. F. Macmillan, B. M. Keyes, D. H. Levi, M. R. Melloch, R. K. Ahrenkiel, and M. S. Lundstrom, "A study of minority carrier lifetime versus doping concentration in n-type GaAs grown by metalorganic chemical vapor deposition," *J. Appl. Phys.*, vol. 72, no. 4, pp. 1436–1442, Aug. 1992, doi: 10.1063/1.351704.
[34] H. C. Casey, D. D. Sell, and K. W. Wecht, "Concentration dependence of the absorption coefficient for n- and p- type GaAs between 1.3 and 1.6 eV," *J. Appl. Phys.*, vol. 46, no. 1, pp. 250–257, Jan. 1975, doi: 10.1063/1.321330.
[35] S. M. Sze and K. K. Ng, *Physics of Semiconductor Devices*. Hoboken, NJ, USA: Wiley, 2006.

JAVIER F. LOZANO received the M.Res. degree in material physics from the University of Santiago de Compostela, Spain, in 2018, where he is currently pursuing the Ph.D. degree in renewable energies and sustainability.

NATALIA SEOANE received the Ph.D. degree from the University of Santiago de Compostela, Santiago, Spain, in 2007. She was a Visiting Postdoctoral Researcher with the University of Glasgow, Glasgow, U.K., from 2007 to 2009, The University of Edinburgh, Edinburgh, U.K., in 2011, and Swansea University, Swansea, U.K., from 2013 to 2015. She is currently a Postdoctoral Researcher with the University of Santiago de Compostela.

ENRIQUE COMESAÑA (Member, IEEE) received the Ph.D. degree from the University of Santiago de Compostela, Spain, in 2013. He is currently an Assistant Professor with the University of Santiago de Compostela. His research interests include modeling and simulation of electronic devices and application of machine learning techniques to simulations of electrical and electronic systems.

FLORENCIA M. ALMONACID received the M.S. degree in electronic engineering from the University of Granada, Granada, Spain, in 2002, and the Ph.D. degree in electronic engineering from the University of Jaén, Jaén, Spain, in 2009. She is currently a Full Professor with the Department of Electronic and Automatic Engineering, University of Jaén. Her research interests include the application of the artificial neural networks in the field of the photovoltaic technology as well as the characterization and modeling of conventional and concentrator photovoltaic devices and systems.

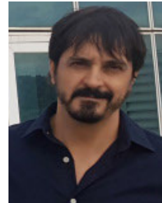

EDUARDO F. FERNÁNDEZ received the Ph.D. degree in concentrator photovoltaics and multi-junction solar cells from the University of Santiago de Compostela, Spain, in 2012. He is currently the Head of the Advances in Photovoltaic Technology Research Group (AdPVTech; https://adpvtech.com/en/home/), University of Jaén, Spain. He has more than ten years of experience in the field of photovoltaics working in several prestigious institutes, universities, and private companies. He has published over 120 papers indexed in ISI JCR, and presented more than 100 contributions in the most relevant international conferences and workshops. He is also the co-inventor of several patents. He is also a member of more than ten academic and scientific societies.

ANTONIO GARCíA-LOUREIRO (Member, IEEE) received the Ph.D. degree from the University of Santiago de Compostela, Santiago, Spain, in 1999. He is currently a Professor of electronics with the University of Santiago de Compostela. His current research interests include multidimensional simulations of nanoscale transistors and solar cells.

USC UNIVERSIDADE DE SANTIAGO DE COMPOSTELA

A.1.3 A new path towards ultra-high efficient laser power converters: Silicon carbide-based multijunction devices

ATTRIBUTION 4.0 INTERNATIONAL

Deed

Canonical URL : https://creativecommons.org/licenses/by/4.0/

See the legal code

You are free to:

Share — copy and redistribute the material in any medium or format for any purpose, even commercially.

Adapt — remix, transform, and build upon the material for any purpose, even commercially.

The licensor cannot revoke these freedoms as long as you follow the license terms.

- Publication quality indicators:
  - Impact factor (JCR 2023): 6.0
  - Quartile: Q1
  - Category: ENGINEERING, MULTIDISCIPLINARY
  - Rank: 10/179
- PhD candidate contribution:

USC UNIVERSIDADE DE SANTIAGO DE COMPOSTELA

- Conceptualization.
- Data curation.
- Investigation.
- Writing – original draft.

USC
UNIVERSIDADE
DE SANTIAGO
DE COMPOSTELA

Results in Engineering 21 (2024) 101987

Contents lists available at ScienceDirect

Results in Engineering

journal homepage: www.sciencedirect.com/journal/results-in-engineering

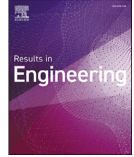

Research paper

A new path towards ultra-high efficient laser power converters: Silicon carbide-based multijunction devices

Javier F. Lozano [a,*], Natalia Seoane [a], Enrique Comesaña [b], Florencia M. Almonacid [c], Eduardo F. Fernández [c], Antonio García-Loureiro [a]

[a] Centro Singular de Investigación en Tecnoloxías de Información (CiTiUS), Departament of Electrónica e Computación, Universidade de Santiago de Compostela, Rúa de Jenaro de la Fuente, s/n, Santiago de Compostela, 15782, Spain

[b] Escola Politécnica Superior de Enxeñaría, Campus Terra, Universidade de Santiago de Compostela, Rúa de Lope Gómez de Marzoa, s/n, Lugo, 27002, Spain

[c] Advances in Photovoltaic Technology (AdPVTech), CEACTEMA, University of Jaén, Edificio C-6 ·Campus de las Lagunillas, Jaén, 23071, Spain

ARTICLE INFO

Keywords:
High power laser transmission
Laser power converters
Silicon carbide
VEHSA
Multijunction cells

ABSTRACT

Current high power laser transmission technology faces two major limitations to improve the efficiency of the photovoltaic receivers: the intrinsic entropic losses associated to low bandgap materials (such as GaAs) and the series resistance losses that degrade the device performance at high power densities. The use of high bandgap materials and new architectures for laser power converters (LPC) have been pointed out as alternatives to overcome these limitations. In this work, three silicon carbide polytypes (3C, 4H and 6H) are proposed as base materials for the standard horizontal laser power converter (hLPC) architecture and the Vertical Epitaxial Hetero-Structure Architecture (VEHSA). 3C SiC based hLPCs outperform the power converters based on the other two polytypes, achieving a maximum efficiency of 84.6% at 100 W cm^{-2}, but suffer from series resistance losses, that deteriorate their efficiency, at higher laser power densities. This issue is solved with 3C SiC 4 cells VEHSAs that demonstrated increasing efficiency with the input power, reaching a maximum of 87.4% at 3000 W cm^{-2}. The VEHSA reduced number of cells minimize the risks of efficiency losses due to current mismatch between cells. These results support the feasibility of a new generation of LPCs capable of efficiently convert ultra-high laser power densities.

1. Introduction

High power laser transmission has been pointed as one of the most promising technologies for far-field wireless power transfer [1]. This technology, which consist of the transmission of power via laser onto a photovoltaic receiver, has the advantage of providing electrical isolation and avoiding electromagnetic interferences [2]. High power laser transmission offers the possibility of transferring power through optic fiber, replacing conventional copper wires and thus reducing the risk of sparks, which is desirable in workplaces under an ATEX directive [3], or through free space, suitable for aerospace environments. There are many applications of this technology, such as the simultaneous transferal of power and data [4,5] or optically powering remote antennas [6], aerial vehicles [7] or even satellites [8,9]. **Fig. 1** depicts the optical powering of a rover in a space application.

The state of the art of the photovoltaic receivers or laser power converters (LPC) are mostly dominated by III-V compounds, specifically GaAs [10]. There are reports of conversion efficiencies exceeding 60% at room temperatures [11] with a record efficiency conversion of 68.9% at 11.4 W cm^{-2}, but as the input power density increases these LPCs suffer from efficiency degradation due to ohmic losses [12]. To face this challenge, new architectures have been proposed [13–16]. The Vertical Epitaxial Hetero-Structure Architecture (VEHSA) stands out among the multijunction LPCs. It consists of monolithically stacked p/n cells connected by tunnel junctions [11], reducing the total current and increasing the outcome voltage in the same ratio, minimizing the Joule heating losses. This allows the device to work under high power densities, which enhances the open circuit voltage (Voc) due to the higher carrier concentration, increasing the conversion efficiency. The current record efficiency for a GaAs-based VEHSA is 66.3% and has been achieved with a 5-cell device at 150 W cm^{-2} [11]. In this work, the au-

* Corresponding author.
E-mail address: javierfernandez.lozano@usc.es (J.F. Lozano).
URL: https://citius.gal/team/javier-fernandez-lozano (J.F. Lozano).

https://doi.org/10.1016/j.rineng.2024.101987
Received 11 December 2023; Received in revised form 26 January 2024; Accepted 4 March 2024
Available online 8 March 2024
2590-1230/© 2024 The Authors. Published by Elsevier B.V. This is an open access article under the CC BY license (http://creativecommons.org/licenses/by/4.0/).

USC UNIVERSIDADE DE SANTIAGO DE COMPOSTELA

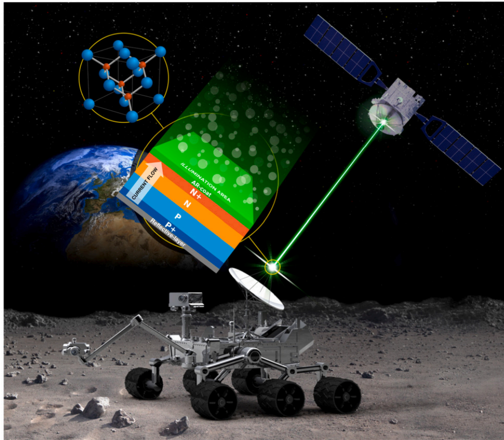

Fig. 1. Artistic example of a high power laser transmission application, a moon rover powered by a remote laser. In the zoom-in yellow circles, a horizontal laser power converter and a cubic silicon carbide structure are depicted.

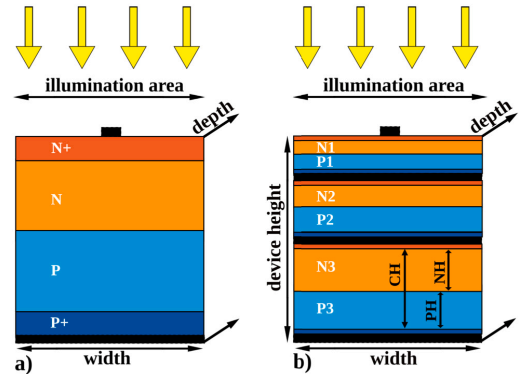

Fig. 2. 2D schemes of the two architectures studied in this work: a) a horizontal laser power converter (hLPC) and b) a 3-cell Vertical Epitaxial Hetero-Structure Architecture (VEHSA) device. The structure of single cells is N+/N/P/P+ doping types. The width and depth dimensions are fixed to 10 and 1 μm, respectively, to save computational costs. The device height, cell height (CH), and N and P layer heights (NH/PH) are shown.

thors also explored VEHSAs with up to 20 cells to try to handle even larger input powers. However, when the number of cells is increased the effect of current mismatching also increments, due to intrinsic fabrication issues, deteriorating the efficiency. Note that, this architecture has also been applied to concentrating photovoltaic solar cells to achieve ultra-high efficiencies [17].

To further improve the performance of the technology, materials with high bandgap have been pointed out [18–20]. These materials will not only reduce the series resistance losses due to the higher energy of the incident photons, increasing the outcome voltage and reducing the current, but they will also reduce the intrinsic entropic losses. In this sense, the use of high bandgap materials such as silicon carbide (SiC) will be beneficial over commonly used photovoltaic materials as silicon or gallium arsenide, which have a lower energy bandgap when compared with this material. In the last two decades, silicon carbide has been extensively researched, and their main applications are in the field of power electronics [21]. So far, 4H and 6H hexagonal polytypes are the most employed [22]. Due to the high electron mobility and isotropic properties of 3C SiC [23], efforts are been made to obtain high quality 3C crystals [24]. Indeed, long carrier lifetimes of 8.2 μs have been achieved in 3C grown by sublimation epitaxy [23]. These values are comparable to those of post growth treated chemical-vapor-deposition grown 4H [25] and 6H [26]. Beyond the high bandgap of these materials, silicon carbide polytypes exhibit other interesting properties. The thermal stability, resistance to radiation and dielectric strength [27,28] of these polytypes make them very interesting candidates for electronic devices and sensors in space applications, where other materials like Si or GaAs will suffer great degradation due to harsh environments [29,30]. Note that these polytypes are also good candidates to manufacture multijunction VEHSA devices, since the requirements for the tunnel junction (TJ) materials are a high conductivity, optical transparency and low lattice mismatch [31]. The highly doped SiC polytypes used as TJ exhibit great conductivity, low absorption coefficient (the absorption is negligible when compared to that of the whole device) and no lattice mismatch. Furthermore, the manufacturing of LPCs made of SiC polytypes is based on non-critical raw materials (compared with the scarcity of III-V materials), more eco-friendly processes (employs less toxic agents than GaAs) and reuses some of the low-cost Si fabrication procedures [32].

In this work we test the suitability of silicon carbide as base material for LPCs comparing the efficiency of three different polytypes (3C, 4H and 6H) for two architectures: the conventional horizontal laser power converter (hLPC) and the VEHSA architecture with 2 (VEHSA-2), 3 (VEHSA-3) and 4 (VEHSA-4) cells. The obtained results open a promising new path to efficiently transmit high power energy densities.

2. Simulation methodology

We investigate the feasibility of the three proposed SiC polytypes through the conventional horizontal laser power converter (hLPC) architecture, see a scheme in **Fig. 2a**. The structure consists of four layers with N+/N/P/P+ doping types. The third dimension (depth) is set to 1 μm to save computational costs, since it does not affect the obtained results. Since there are several technological solutions to minimize the effect of surface recombination, e.g. using passivation layers [33], and considering that the generation and transport processes occur in the vertical direction, the width of the devices is set to 10 μm also to save computational costs. We emulate the behavior of an anti-reflective coating by setting total transmittance in the illumination area, which is a realistic approximation because the device is illuminated with only one wavelength. As the SiC polytypes have a low absorption coefficient due to their indirect bandgap [34], a textured reflective layer is needed at the bottom of the device. This layer increases the optical path, greatly enhancing light absorption and photon recycling [35], which avoids an excessively long device where the minority carriers will recombine. The cathode is placed at the top of the device, covering a 3% of the illumination area, while the anode is placed along the bottom of the device. Once the polytype with the best performance has been determined, we explore the use of this polytype in the VEHSA architecture (see an example in **Fig. 2b**).

In this work we have employed Silvaco Atlas [36], a TCAD simulator widely used in modeling all kind of semiconductor devices, including photovoltaic cells. Indeed, it has been applied to model laser power converters [13], multijunction concentrator solar cells [37] and VEHSA devices [15]. The J-V characteristics of the devices are obtained by solving the Poisson and charge continuity equations. The models and parameters used in this work are suitable for silicon carbide polytypes. We use the Caughey–Thomas model for carrier mobility, which accounts for doping density dependence [38]. The simulations include the following recombination processes: Shockley–Read–Hall (SRH), which is the main recombination mechanism in indirect bandgap semiconductors [39], and Auger recombination, which affects at high injection levels. We used the Lindefelt bandgap narrowing model [40], which was developed specifically for silicon carbide polytypes. The beam-

USC UNIVERSIDADE DE SANTIAGO DE COMPOSTELA

Table 1
Material parameters included in the simulation framework. The bandgap [46], incident wavelength (λ), thermal conductivity (κ)[47], effective densities of states in the conduction/valence bands(N_C/N_V) [36], electron and hole mobilities [44,48,49], Auger recombination coefficients [44,45] and Shockley-Read-Hall base lifetimes (SRH τ_0) [23,25,26,50] are shown.

Polytypes	Bandgap [eV]	λ [nm]	κ [W m^{-1} K^{-1}]		N_C / N_V [cm^{-3}]	Mobility [cm^2/V/s]	Auger coeff. [cm^6 s^{-1}]	SRH τ_0 [s]
3C	2.36	525	500	e-	6.5×10^{18}	900	3×10^{-32}	1.1×10^{-5}
				h+	1.7×10^{18}	70	2×10^{-32}	2.2×10^{-6}
4H	3.23	366	350	e-	1.7×10^{19}	950	5×10^{-31}	1.7×10^{-4}
				h+	3.3×10^{19}	125	2×10^{-31}	2.1×10^{-5}
6H	3.02	400	320	e-	7.7×10^{18}	420	3×10^{-29}	1.3×10^{-5}
				h+	4.7×10^{18}	95	3×10^{-29}	2.5×10^{-6}

Table 2
Optimum design parameters of 3C, 4H and 6H SiC hLPCs at laser power densities (P_{in}) of 1, 100 and 1000 W cm^{-2}. The thicknesses and doping values of the P and N layers are shown.

	Layer	3C			4H			6H		
P_{in} [W cm^{-2}]		1	100	1000	1	100	1000	1	100	1000
Thickness [µm]	N	14	14	14	14	14	12	14	22	8
	P	69	69	61	69	69	53	69	40	30
Doping [cm^{-3}]	N	1×10^{15}	1×10^{15}	1×10^{15}	1×10^{15}	1×10^{15}	1×10^{15}	1×10^{16}	1×10^{16}	5×10^{16}
	P	7×10^{16}	3×10^{17}	1×10^{18}	1×10^{15}	5×10^{16}	3×10^{17}	1×10^{16}	5×10^{16}	1×10^{17}

device interaction is modeled with the ray tracing method [36]. The absorption coefficient used for each polytype fits experimental data [34,41,42]. We conducted this study at a constant temperature of 298 K, which is the standard in the photovoltaic (PV) field. Note that, to ensure the success of this technology, it will be necessary to examine how the temperature changes with increasing laser power densities and its impact on the device performance, considering relevant factors, such as efficiency, surface area, and thermal resistance. However, there are available mechanisms to manage the heat waste, for instance the use of simple passive solutions based on a flat plate, already implemented in ultra-high CPV systems at concentrations up to 10,000 suns (1 kW cm^{-2}) [43]. Also, note that these LPCs are expected to have efficiencies above 70%, which means that a maximum of 30% of the power could be transformed into heat.

Table 1 shows material parameters for the three SiC polytypes for electrons and holes, being these the energy bandgap, the effective conduction and valence bands density of states (DOS), the maximum mobilities, the Auger recombination coefficients and the Shockley-Read-Hall recombination base lifetimes. The effective DOS are higher in the 4H than in the 3C and 6H, both in conduction and valence bands [36]. The Auger recombination coefficients are smaller in 3C (i.e. material less affected by Auger recombination), being one order and three orders of magnitude lower than those of the 4H and 6H, respectively [44,45]. The higher bandgap energy and higher carrier mobilities of the 4H (3.23 eV and 950/125 cm^2 V^{-1} s^{-1} for e-/h+, respectively) make it a sound candidate for LPC base material. The 6H also has a high bandgap of 3.02 eV, but the mobilities are lower than in the 4H (420/95 cm^2 V^{-1} s^{-1} for e-/h+). The 3C has the lowest bandgap energy of the proposed polytypes (2.36 eV), and the mobilities are comparable to those of the 4H (900/70 cm^2 V^{-1} s^{-1} for e-/h+). However, the thermal conductivity is higher for the 3C (500 W m^{-1} K^{-1}) than for the 4H and 6H (350 and 320 W m^{-1} K^{-1}, respectively). This could position the 3C SiC as the preferred choice for LPC base material in extreme conditions, making it better suited for space applications.

The optimization of the hLPC devices was performed with a multivariable iterative process, varying the design parameters in discrete steps to find the optimum design that maximizes the efficiency. These parameters are the thicknesses and doping values of the N and P layers. In the VEHSA architecture, the optimization is more challenging and requires more sophisticated methods, because there are several cells in the same LPC. For that, the authors recently proposed PhPO (Photogeneration and Performance Optimization), a new optimization algorithm suitable for TCAD studies of multijunction photovoltaic devices [51]. This algorithm consists of two stages. First, the total height of the device is adjusted to absorb the largest part of the incident beam. Once that is fixed, the second stage first modifies the relative size of the cells to reduce the current mismatch to a certain tolerance value. Then, each design parameter of each individual cell (relative N/P layer sizes, N/P doping values) is optimized. This second stage iterates to reduce again the current mismatch between cells, since the new design parameters could change the current of some cells.

3. Results

In this section we evaluate the feasibility of three SiC polytypes (3C, 4H and 6H) as base material for LPCs. We performed optimizations under several input power densities using the conventional horizontal architecture (hLPC). Once the polytype with the best performance has been established, we explore its feasibility as base material for the VEHSA architecture. This is done by conducting a series of optimizations for VEHSA devices with 2, 3 and 4 cells under a wide range of laser power densities.

Table 2 shows the optimum design parameters of the hLPCs made of the three polytypes. At an input power density of 1 W cm^{-2} the optimum thicknesses of the N/P layers for the three polytypes are identical, 14 µm for the N layer and 69 µm for the P layer, which produces a total height of the devices of 83 µm. For the 3C and 4H SiC devices these optimum thicknesses do not change at 100 W cm^{-2}, while in the 6H device the total thickness reduces to 62 µm with a 22/40 µm for the N/P layers respectively. This reduction is due to the impact of Auger recombination, which severely degrades the performance in the 6H devices. As seen in Table 1, the Auger coefficients for the 6H are 2 and 3 orders of magnitude larger than the 4H and 3C coefficients, respectively. Decreasing the total height reduces the total amount of photogenerated carriers and thus the Auger recombination, at the cost of reducing the amount of absorbed photons. For this reason, at 1000 W cm^{-2} the 3C, 4H and 6H device total heights reduce to 75 µm, 65 µm, and 38 µm, respectively. The optimum doping values in the P layer consistently increase with a rise in the input power density, with P_{in} ranging from 1 to 1000 W cm^{-2} the 4H acceptor concentrations increase two orders of

USC UNIVERSIDADE DE SANTIAGO DE COMPOSTELA

Table 3
Main figures of merit for the three SiC polytypes using the hLPC architecture, being these: Short circuit current density (J_{SC}), open circuit voltage (V_{OC}), the V_{OC} growth with the laser power density (ΔV_{OC}), the fill factor (FF) and efficiency (Eff). Results are shown for input laser power densities (P_{in}) ranging from 1 to 1000 W cm^{-2}.

	Pin [W cm^{-2}]	Jsc [A cm^{-2}]	Voc [V]	ΔVoc [V]	FF [%]	Eff [%]
3C	1	0.390	2.14	-	93.1	78.3
	10	3.95	2.25	0.11	92.9	82.3
	100	39.8	2.30	0.16	92.2	84.6
	1000	385	2.35	0.21	89.1	80.8
4H	1	0.280	2.88	-	94.7	77.5
	10	2.84	2.94	0.06	94.6	78.9
	100	28.4	2.99	0.12	93.6	79.4
	1000	276	3.04	0.16	91.8	77.2
6H	1	0.310	2.70	-	94.4	77.9
	10	3.08	2.74	0.04	93.3	78.9
	100	29.9	2.79	0.09	90.9	75.9
	1000	270	2.84	0.14	84.4	64.7

magnitude, from 1×10^{15} to 3×10^{17} cm^{-3}, while the 3C and 6H increase around one order of magnitude, from 7×10^{16} to 1×10^{18} cm^{-3} and from 1×10^{16} to 1×10^{17} cm^{-3}, respectively. However, the optimum donor concentration in the 3C and 4H devices remains constant at 1×10^{15} cm^{-3} for all input power densities. In the 6H-SiC, the optimum N doping value is 1×10^{16} cm^{-3}, one order of magnitude higher, except for a P_{in} of 1000 W cm^{-2}, which is 5×10^{16} cm^{-3}.

Table 3 shows the main figures of merit that characterize the hLPCs: the short circuit current density (J_{SC}), the open circuit voltage (V_{OC}), the V_{OC} growth with the laser power density (ΔV_{OC}), which is defined as the difference between the V_{OC} at a given power density and the V_{OC} at 1 W cm^{-2}: $\Delta V_{OC}(P_{in}) = V_{OC}(P_{in}) - V_{OC}(1\,\mathrm{W\,cm^{-2}})$, the fill factor (FF) and the device efficiency (Eff). The J_{SC} grows proportionally to the laser power density, showing slight losses at 1000 W cm^{-2}. The 6H experiences a higher J_{SC} decay with the input power due to the reduction of the total height of the device at high laser power densities previously discussed. The V_{OC} also grows with the laser power density, as expected from the classical approximation [52]:

$$V_{OC} = \frac{k_B T}{q} ln \left[\frac{(N_A + \Delta n)\Delta n}{n_i^2} \right] \quad (1)$$

where $k_B T/q$ is the thermal voltage, N_A is the doping concentration, Δn is the excess carrier concentration and n_i is the intrinsic carrier concentration. By increasing the laser power density the Δn also increases, leading to a larger V_{OC}. ΔV_{OC} is different for each material, as seen in Table 3. Note that the 3C has larger ΔV_{OC} than the 4H. This is due to the higher optimum doping values resulting from the optimization process, and also due to the higher N_C and N_V values of the 4H (see Table 1), that are related to the intrinsic carrier concentration, as follows:

$$n_i = \sqrt{N_C N_V} \cdot e^{\frac{-E_g}{2K_B T}} \quad (2)$$

where E_g is the bandgap energy. For a given E_g, higher N_C and N_V values increase the intrinsic carrier concentration, decreasing the open circuit voltage as seen in **Equation (1)**. The 6H devices, despite having N_C and N_V values similar to those of the 3C, experience less V_{OC} growth than the 3C and 4H devices due to the Auger recombination. The FF exceeds 90% for the three polytypes at all laser power densities except for 1000 W cm^{-2} due to the series resistance losses. These high FF values are due to the large bandgap of the polytypes, which reduce the ohmic losses.

The efficiency of these devices is also shown in Table 3. Theoretically, it is expected that the larger the bandgap, the larger the efficiency of the LPCs, as indicated in [18], if no other material properties are taken into account. However, at a P_{in} value of 1 W cm^{-2} the three hLPCs obtain nearly the same efficiency, around ≈ 78%. This is due to losses related to the light absorption. To ensure an adequate photogeneration inside the devices without greatly increase their height, we chose incident wavelengths for each material that guarantee an extinction coefficient of at least $k = 2 \times 10^{-4}$. This value was established after a preliminary analysis to maximize the light absorption without compromising the efficiency of the device due to the minority carrier diffusion length. These wavelength values can be seen in Table 1. The difference between the energy of the monochromatic incident light and the energy gap of the material produces different efficiency losses. The 3C loses an efficiency of 1%, the 6H a 2.5% and the 4H a 5%. However, note that this assumption does not affect the trend of efficiency versus input power density.

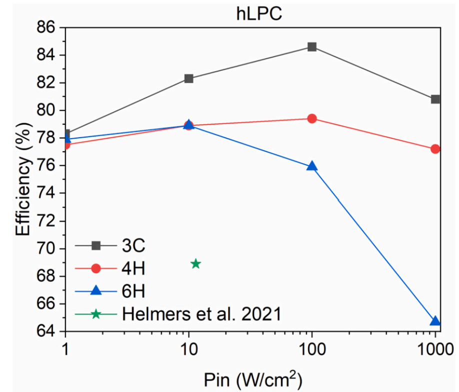

Fig. 3. Efficiency versus input power density (P_{in}) for the three SiC polytypes using the hLPC architecture. The best performance experimental GaAs-hLPC is included for comparison [12].

As the laser power density increases, the efficiencies of the 3C hLPCs increase more than those of the two other polytypes, reaching a 82.3% efficiency at 10 W cm^{-2}, which is a 3.4% higher than those of 4H and 6H. For comparison, the current best performance experimental GaAs-hLPC achieves a 68.9% efficiency at 11.4 W cm^{-2} [12], which is 13.4% lower than the proposed 3C SiC hLPC (note that this device has not been fabricated yet, so the performance may be impacted by manufacturing issues). The 3C SiC hLPC efficiency keeps increasing with the laser power density, achieving a 84.6% at 100 W cm^{-2}. In the case of the 4H, the higher N_C and N_V values limit the growth of the V_{OC} with the laser power density, limiting the efficiency of the 4H hLPCs to a 79.4% at 100 W cm^{-2}. The 6H SiC devices reach a 78.9% efficiency at 10 W cm^{-2} and experience a quick performance degradation to 75.9% at 100 W cm^{-2} due to Auger recombination. At an input power density of 1000 W cm^{-2}, independently of the polytype, the SiC hLPCs reduce their performance due to series resistance losses and Auger recombination, to efficiency values of 80.8%, 77.2% and 64.7% for the 3C, 4H and 6H SiC hLPCs, respectively. These efficiency values are also shown in **Fig. 3**, where it is clear that 3C outperforms the other polytypes for the hLPC architecture.

To evaluate the performance stability with the laser power density of the optimized devices, we chose three 3C-SiC hLPCs, optimized at 1 W cm^{-2} (opt1), 100 W cm^{-2} (opt100), and 1000 W cm^{-2} (opt1000), and tested them under different P_{in} values. Their resulting efficiency values are shown in **Fig. 4**. Note that the main difference in the design parameters of these devices is the P-layer doping value, which is increased from 7×10^{16} cm^{-3} in opt1 to 1×10^{18} cm^{-3} in opt1000 (see Table 2). As expected, the best performance device for each laser power density is the one that has been optimized for that particular power. At 1 W cm^{-2}, opt1 achieves an efficiency 1.5% higher than the opt100 and

USC UNIVERSIDADE DE SANTIAGO DE COMPOSTELA

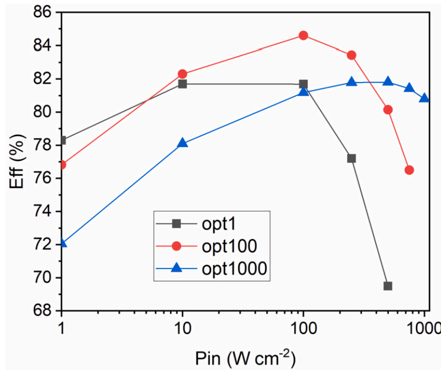

Fig. 4. Efficiency versus input power density (P_{in}) for the 3C SiC hLPCs optimized at $1\,W\,cm^{-2}$ (opt1), $100\,W\,cm^{-2}$ (opt100), and $1000\,W\,cm^{-2}$ (opt1000).

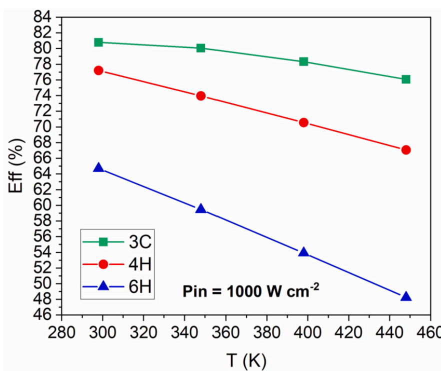

Fig. 5. Efficiency versus temperature for the three hLPC-SiC polytypes optimized at $1000\,W\,cm^{-2}$.

6.25% higher than the opt1000. However, as the laser power density increases, the opt1 performance worsens compared to opt100, which outperforms op1 by 2.9% and opt1000 by 3.4% at $100\,W\,cm^{-2}$. At higher laser power densities, both opt1 and opt100 experience efficiency degradation, loosing at $500\,W\,cm^{-2}$ a 12.2% efficiency for the opt1 and a 4.5% for the opt100. The opt1000 reaches its maximum efficiency of 81.81% at $500\,W\,cm^{-2}$, and manages to convert a laser power density of $1000\,W\,cm^{-2}$ with only a 1% efficiency decay. It is noteworthy that by increasing the doping concentration in the P-layer greater performance stability at high P_{in} values is achieved, but limits its efficiency at lower laser power densities. These results highlight the need to optimize the device structures according to the targeted laser power density, which will depend on the application of the technology.

To analyze the effect of temperature on the proposed devices, **Fig. 5** compares the efficiency of the 3C, 4H and 6H hLPCs versus the temperature (at 25, 50, 100 and 150 °C). This study has been done at a Pin of $1000\,W\,cm^{-2}$, which is the highest laser power density tested for these hLPCs, and therefore, the most likely to suffer from heating problems. The efficiency degradation due to heating is more severe in 6H hLPC, which loses a 16.5% efficiency when the temperature is increased to 150 ºC, whereas the 4H loses a 10.2% and the 3C only loses a 4.7%, which makes the 3C-based hLPCs the most temperature-resilient. These results suggest that the effect of temperature might not be a critical point in the viability of the proposed technology.

Given that all polytypes experience performance degradation at high laser power densities, we introduce the Vertical Epitaxial Hetero-Structure Architecture (VEHSA), to avoid this intrinsic limitation of the hLPC architecture. This design was introduced to reduce the series resistance losses by splitting the photogenerated current between vertically stacked N/P cells, while increasing the output voltage in a similar ratio. As the 3C SiC based hLPC has better performance at all input power densities than those based on the other polytypes, we chose this polytype to conduct a comparative between the hLPC conventional architecture and VEHSA devices with 2, 3, and 4 cells. We optimized these devices for input power densities ranging from 1 to 3000 $W\,cm^{-2}$, since the VEHSA architecture allows us to use higher laser power densities due to the reduction of series resistance losses, as explained in section 1.

Table 4 shows the optimum design parameters for the VEHSA devices at 1 and $3000\,W\,cm^{-2}$, which are the individual cell heights (CH), the relative N/P layer heights, shown in percentage of the correspondent cell height (NH/PH) and the N/P layer doping values (ND/PD). The optimum device height is 106 μm for all the VEHSA devices, which is 23 μm larger than that of the 3C SiC-based hLPC (see Table 2). Since the VEHSA architecture consists of monolithically stacked N/P cells (see Fig. 2), the photogenerated carriers travel less distance than in the hLPC architecture. Therefore the carrier diffusion length is not a limiting factor and the optimum height of VEHSA devices is larger, in order to absorb almost all of the incident beam. The individual cell heights (CH) are adjusted to minimize the current mismatch between the cells. The upper cells are smaller than the lower ones, since the photogeneration decays as the light traverses the device, so each CH needs to be larger to generate the same amount of carriers as in the previous cell. Note that these CH values cannot be obtained through calculations using the Beer-Lambert exponential decay of light, since the optical path is highly increased due to light trapping mechanisms placed at the bottom of the device. Moreover, the optimizer consistently found that optimal configurations are those with the P layer larger than the N layer. This is more pronounced at low input power densities and in the lower cells (those closer to the bottom cell), as can be seen in Table 4. The top cell has higher optimum doping values than the other cells, at all configurations and power densities. At a P_{in} value of $1\,W\,cm^{-2}$ the N layer has optimum donor concentrations in the range of 5×10^{17} and 1×10^{18} cm^{-3}, while the P layer has acceptor concentrations ranging from 1×10^{17} to 3×10^{17} cm^{-3}. At $3000\,W\,cm^{-2}$ the optimum N doping values decrease to 1×10^{15} cm^{-3}, while the P doping increase to values ranging from 7×10^{17} to 1×10^{18} cm^{-3}.

The voltages (V_M) and current densities (J_M) at the maximum power point provided by each cell at 1 and $3000\,W\,cm^{-2}$ are shown in **Table 5**. The V_M values of the top cells (cell 1) are larger than those of the other cells due to the higher density of photogenerated carriers (see Equation (1)). Note that the current mismatch in the J_M is minimal. For example, the VEHSA-2 at $1\,W\,cm^{-2}$ has a 0.04% current mismatch. The largest observed mismatch is a 0.73% for the VEHSA-4 at $1\,W\,cm^{-2}$, which shows the good performance of the PhPO algorithm. For 3C SiC only 4 cells are needed to handle these very high input powers, however for other low band gap materials, e.g. GaAs, a much larger number of cells will be needed, which at the same time, will increase the current mismatch, reducing the global efficiency of the system [11].

The JV curves for the hLPC and the VEHSA-2, VEHSA-3 and VEHSA-4 are shown in **Fig. 6** and **7** for $1\,W\,cm^{-2}$ and $3000\,W\,cm^{-2}$, respectively. It can be seen that the V_{OC} values increase with larger laser power densities for all devices, ranging from 2.13 to 2.37 V in the hLPC architecture, from 4.28 V to 4.74 V in the VEHSA-2, from 6.42 V to 7.09 V in the VEHSA-3 and from 8.55 V to 9.42 V in the VEHSA-4. The FF is mainly affected by series resistance as the laser power density increases from 1 to $3000\,W\,cm^{-2}$, thus reduces from 93.17% to 79.65% in the hLPC architecture, from 93.47% to 88.94% in the VEHSA-2, from 93.62% to 91.36% in the VEHSA-3 and from 93.66% to 92.26%in the VEHSA-4. Note that the fill factor consistently increases with the number of VEHSA cells, and also experiences less degradation at high laser power densities than the hLPC, proving the resilience of the VEHSA architecture to the series resistance losses.

USC UNIVERSIDADE DE SANTIAGO DE COMPOSTELA

Table 4
Design parameters (DP) of the VEHSA devices at 1 and 3000 W cm^{-2}. CH is the cell height, NH/PH the relative N/P layer heights in percentage of the respective CH and ND/PD the doping values for the N/P layers.

Pin		1 W cm^{-2}				3000 W cm^{-2}			
DP		CH	NH/PH	ND	PD	CH	NH/PH	ND	PD
Device	Cell	[μm]	[%]	[cm^{-3}]	[cm^{-3}]	[μm]	[%]	[cm^{-3}]	[cm^{-3}]
VEHSA-2	1	48.6	10/90	1e18	1e17	48.1	35/65	1e15	1e18
	2	57.4	5/95	5e17	1e17	57.9	15/85	1e15	1e18
VEHSA-3	1	30.6	10/90	1e18	3e17	30.5	35/65	1e15	1e18
	2	36.3	5/95	5e17	1e17	36.5	5/95	1e15	1e18
	3	39.1	5/95	5e17	1e17	39.0	5/95	1e15	1e18
VEHSA-4	1	22.4	10/90	1e18	3e17	22.3	45/55	1e15	1e18
	2	25.7	5/95	5e17	3e17	25.8	5/95	1e15	7e17
	3	28.6	5/95	5e17	1e17	28.7	5/95	1e15	7e17
	4	29.3	5/95	5e17	3e17	29.3	5/95	1e15	7e17

Table 5
Figures of merit (FOM) voltage (V_M) and current density (J_M) at the maximum power point for the hLPC architecture and all the individual cells of the VEHSA-2, VEHSA-3 and VEHSA-4 for 1 and 3000 W cm^{-2} laser power densities.

Pin		1 W cm^{-2}		3000 W cm^{-2}	
FOM		Vm	Jm	Vm	Jm
	Cell	[V]	[A cm^{-2}]	[V]	[A cm^{-2}]
hLPC	-	2.010	0.38754	1.96	1109.2
VEHSA-2	1	2.030	0.19815	2.164	587.35
	2	2.018	0.19807	2.117	587.73
VEHSA-3	1	2.050	0.13281	2.223	397.43
	2	2.013	0.13262	2.168	397.97
	3	2.015	0.13289	2.164	396.21
VEHSA-4	1	2.050	0.09930	2.245	298.51
	2	2.021	0.09913	2.181	298.87
	3	2.009	0.09986	2.180	297.63
	4	2.015	0.09983	2.177	298.79

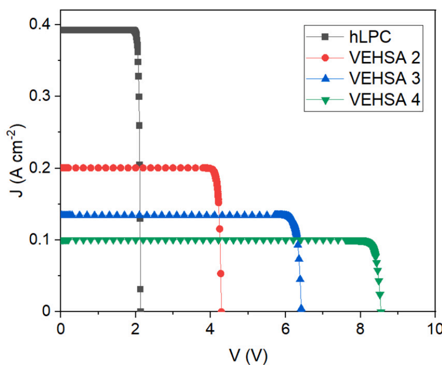

Fig. 6. JV curves of 3C SiC-based devices using the hLPC architecture and VEHSAs with 2, 3 and 4 cells at 1 W cm^{-2}.

The efficiencies of these devices are shown in **Fig.** 8. The hLPC achieves efficiencies of 78.3%, 82.3% and 84.6% at 1, 10 and 100 W cm^{-2}, which are around 2% lower than those of the VEHSA devices. These small differences are due to the higher optimum device height of the VEHSA structures, allowing them to trap a larger part of the beam as previously discussed. The current best performance experimental GaAs-VEHSA-5 device [11] is also included in Fig. 8. Note that,

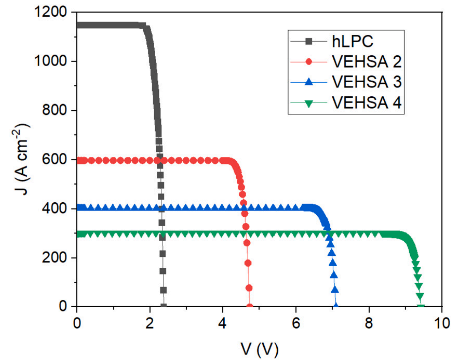

Fig. 7. JV curves of 3C SiC-based devices using the hLPC architecture and VEHSAs with 2, 3 and 4 cells at 3000 W cm^{-2}.

although the proposed 3C VEHSAs have not been fabricated yet, so their final performance might be reduced due to manufacturing issues, their efficiency is 19.7% higher than that of the GaAs-based VEHSA. At an input power density of 1000 W cm^{-2} the hLPC and the VEHSA-2 lose a 6.6% and 1.6% efficiency, respectively, when compared to the VEHSA-3 and VEHSA-4 due to ohmic losses, which achieve an efficiency of ≈86.3%. At 3000 W cm^{-2} all devices show signs of efficiency degradation except VEHSA-4. This structure outperforms the rest of the devices at this P_{in} value, showing an efficiency of 87.4%, a value 0.7%, 3.6% and 14.9% larger than those of the VEHSA-3, VEHSA-2 and hLPC, respectively. This clearly demonstrates that increasing the number of cells mitigates efficiency degradation due to series resistance losses at high input power densities.

4. Conclusions

In this work we combined for the first time two strategies to improve the high power laser transmission technology, the use of high bandgap materials and the VEHSA architecture. For that purpose we explore the suitability of three silicon carbide polytypes, 3C, 4H and 6H as base materials for the commonly used horizontal laser power converter architecture (hLPC). We optimized the hLPC structure for an input power density range of 1-1000 W cm^{-2}. All the polytypes outperform the current best performance achieved for an experimental LPC, which is a GaAs-based hLPC that obtained a 68.9% efficiency at 11.4 W cm^{-2}. At 10 W cm^{-2}, the SiC polytypes exceed the state of the art by 13.4% for the 3C and by 10% for the 4H and 6H. The 3C based hLPCs show greater efficiency than the other polytypes at all the input power den-

USC UNIVERSIDADE DE SANTIAGO DE COMPOSTELA

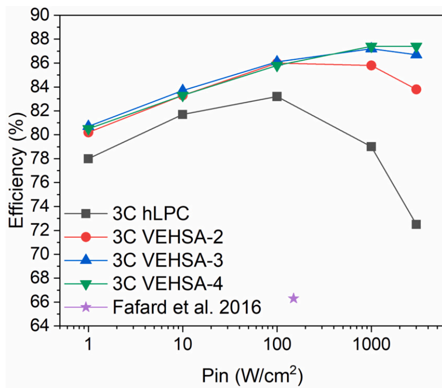

Fig. 8. Efficiency versus input power density (P_{in}) for 3C SiC-based devices using the hLPC architecture and VEHSAs with 2, 3 and 4 cells. The best performance experimental GaAs-VEHSA-5 is included for comparison [11].

sities tested. This is due to the larger effective DOS values of the 4H, which diminish the growth of the V_{OC} with the increase of P_{in}, and the 6H Auger coefficients, which severely degrade the performance of the 6H hLPCs as the P_{in} increases. Also, 3C SiC shows higher resilience to the efficiency reduction due to an increase of the temperature than the other two polytypes. The 3C hLPC reaches a maximum efficiency value of 84.6% at 100 W cm^{-2}. However, as the laser power density increases, the 3C hLPC suffers from efficiency degradation, decreasing to 80.8% at 1000 W cm^{-2}. To counteract for this effect, we performed a series of optimizations of 3C SiC-based VEHSA devices with 2, 3 and 4 cells, increasing the laser power range to 3000 W cm^{-2}. Results show that the VEHSA performs better than the hLPC architecture for all the input power range due to the reduction of the current, allowing to increase the height of these devices to absorb a larger part of the beam than in the hLPC architecture, where the diffusion length of the carriers is one of the main limiting factors. In addition, increasing the number of VEHSA cells mitigates the losses due to Joule effect. At high laser power densities, the VEHSA-2 suffers from series resistance losses, with a 1.6% and 3.6% efficiency drop at 1000 and 3000 W cm^{-2}, respectively, when compared to the VEHSA-4, but outperforms the hLPC by a 5% and a 11.3% at these laser power densities. At 3000 W cm^{-2}, the VEHSA-4 achieves a 87.4% efficiency. Note that, using 3C SiC, only 4 cells are needed to handle these extremely large input powers, whereas when using low bandgap materials (such as GaAs) VEHSAs with larger numbers of cells are mandatory, which suffer from current mismatch issues.

It is worth remarking potential challenges for the future adoption of the high power laser transmission technology, such as the need of a direct line from the laser source to the target (unless optic fiber is used), the possible high laser power attenuation in media like air (lower in SiC than in conventional GaAs based LPCs [18]) or the eye safety implications due to using high power lasers operating in the visible regime (that can be solved via tailored automatic laser shutdown and automatic power reduction systems). Finally, although the performance of real SiC-based LPCs may be impacted by manufacturing issues, the presented results show that the combined use of 3C SiC and the VEHSA architecture is a beneficial addition and opens a promising route towards efficiently transmit ultra-high laser power densities. The proposed technology creates a new paradigm shift with the possibility of transferring power densities up to kilowatts per square centimeter to large distances through a mediums like terrestrial atmosphere (powering aerial drones, remote sensors and robots), water (in underwater autonomous vehicles) or outer space (in rovers and satellites).

CRediT authorship contribution statement

Javier F. Lozano: Writing – original draft, Investigation, Data curation, Conceptualization. **Natalia Seoane:** Writing – review & editing, Supervision, Funding acquisition, Conceptualization. **Enrique Comesaña:** Writing – review & editing, Software, Methodology. **Florencia M. Almonacid:** Investigation. **Eduardo F. Fernández:** Methodology. **Antonio García-Loureiro:** Writing – review & editing, Project administration, Funding acquisition, Conceptualization.

Declaration of competing interest

The authors declare that they have no known competing financial interests or personal relationships that could have appeared to influence the work reported in this paper.

Data availability

Data will be made available on request.

References

[1] K. Jin, W. Zhou, Wireless laser power transmission: a review of recent progress, IEEE Trans. Power Electron. 34 (2019) 3842–3859.

[2] D. Krut, R. Sudharsanan, W. Nishikawa, T. Isshiki, J. Ermer, N.H. Karam, Monolithic multi-cell GaAs laser power converter with very high current density, in: Conference Record of the IEEE Photovoltaic Specialists Conference, 2002, pp. 908–911.

[3] C. Algora, I. García, M. Delgado, R. Peña, C. Vázquez, M. Hinojosa, I. Rey-Stolle, Beaming power: photovoltaic laser power converters for power-by-light, Joule (2021) 1–29.

[4] M. Matsuura, H. Nomoto, H. Mamiya, T. Higuchi, D. Masson, S. Fafard, Over 40-W electric power and optical data transmission using an optical fiber, IEEE Trans. Power Electron. 36 (2021) 4532–4539.

[5] H. Helmers, C. Armbruster, M. Von Ravenstein, D. Derix, C. Schoner, 6-W optical power link with integrated optical data transmission, IEEE Trans. Power Electron. 35 (2020) 7904–7909.

[6] C. Vázquez, J.D. López-Cardona, P.C. Lallana, D.S. Montero, F.M.A. Al-Zubaidi, S. Pérez-Prieto, I. Pérez Garcilópez, Multicore fiber scenarios supporting power over fiber in radio over fiber systems, IEEE Access 7 (2019) 158409–158418.

[7] N. Kawashima, K. Takeda, H. Matsuoka, Y. Fujii, M. Yamamoto, Laser energy transmission for a wireless energy supply to robots, in: 22nd International Symposium on Automation and Robotics in Construction, ISARC 2005, International Association for Automation and Robotics in Construction (IAARC), Ferrara, Italy, 2005.

[8] D. Shi, L. Zhang, H. Ma, Z. Wang, Y. Wang, Z. Cui, Research on Wireless Power Transmission System Between Satellites, 2016 IEEE Wireless Power Transfer Conference, WPTC 2016, vol. 3, IEEE, 2016, pp. 1–4.

[9] M. Sanders, J.S. Kang, Utilization of polychromatic laser system for satellite power beaming, IEEE Aerosp. Conf. Proc. (2020) 1–7.

[10] J. Schubert, E. Oliva, F. Dimroth, W. Guter, R. Loeckenhoff, A.W. Bett, High-voltage GaAs photovoltaic laser power converters, IEEE Trans. Electron Devices 56 (2009) 170–175.

[11] S. Fafard, F. Proulx, M.C.A. York, L.S. Richard, P.O. Provost, R. Arès, V. Aimez, D.P. Masson, High-photovoltage GaAs vertical epitaxial monolithic heterostructures with 20 thin p/n junctions and a conversion efficiency of 60%, Appl. Phys. Lett. 109 (2016) 131107.

[12] H. Helmers, E. Lopez, O. Höhn, D. Lackner, J. Schön, M. Schauerte, M. Schachtner, F. Dimroth, A.W. Bett, 68.9% efficient GaAs-based photonic power conversion enabled by photon recycling and optical resonance, Phys. Status Solidi RRL 15 (2021) 1–7.

[13] C. Outes, E.F. Fernandez, N. Seoane, F. Almonacid, A.J. Garcia-Loureiro, GaAs vertical-tunnel-junction converter for ultra-high laser power transfer, IEEE Electron Device Lett. (2021) 1.

[14] N. Seoane, E.F. Fernández, F. Almonacid, A. García-Loureiro, Ultra-efficient intrinsic-vertical-tunnel-junction structures for next-generation concentrator solar cells, Prog. Photovolt. 29 (2021) 231–237.

[15] M.C. York, A. Mailhot, A. Boucherif, R. Arès, V. Aimez, S. Fafard, Challenges and strategies for implementing the vertical epitaxial heterostructure architecture (VEHSA) design for concentrated photovoltaic applications, Sol. Energy Mater. Sol. Cells 181 (2018) 46–52.

[16] S. Fafard, D.P. Masson, Perspective on photovoltaic optical power converters, J. Appl. Phys. 130 (2021) 160901.

[17] S.P. Philipps, A.W. Bett, III-V Multi-Junction Solar Cells and Concentrating Photovoltaic (CPV) Systems, 2014.

[18] E.F. Fernández, A. García-Loureiro, N. Seoane, F. Almonacid, Band-gap material selection for remote high-power laser transmission, Sol. Energy Mater. Sol. Cells 235 (2022) 111483.

USC UNIVERSIDADE DE SANTIAGO DE COMPOSTELA

[19] E. Oliva, F. Dimroth, A.W. Bett, GaAs converters for high power densities of laser illumination, Prog. Photovolt. 16 (2008) 289–295.
[20] M. Lin, W.E. Sha, W. Zhong, D. Xu, Intrinsic losses in photovoltaic laser power converters, Appl. Phys. Lett. 118 (2021) 1–5.
[21] X. She, A.Q. Huang, O. Lucia, B. Ozpineci, Review of silicon carbide power devices and their applications, IEEE Trans. Ind. Electron. 64 (2017) 8193–8205.
[22] J.N. Shenoy, J.A. Cooper, M.R. Melloch, High-voltage double-implanted power MOSFET's in 6H-SiC, IEEE Electron Device Lett. 18 (1997) 93–95.
[23] I.G. Ivanov, R. Liljedahl, R. Yakimova, M. Syväjärvi, Considerably long carrier lifetimes in high-quality 3C-SiC(111), Appl. Phys. Lett. 100 (2012) 252101.
[24] P. Neudeck, A. Trunek, D. Spry, J. Powell, H. Du, M. Skowronski, X. Huang, M. Dudley, CVD growth of 3C-SiC on 4H/6H mesas, Chem. Vap. Depos. 12 (2006) 531–540.
[25] T. Miyazawa, M. Ito, H. Tsuchida, Evaluation of long carrier lifetimes in thick 4H silicon carbide epitaxial layers, Appl. Phys. Lett. 97 (2010).
[26] S.A. Reshanov, G. Pensl, Comparison of electrically and optically determined minority carrier lifetimes in 6H-SiC, Mater. Sci. Forum 483–485 (2005) 417–420.
[27] J.-M. Lauenstein, M.C. Casey, R.L. Ladbury, H.S. Kim, A.M. Phan, A.D. Topper, Space radiation effects on SiC power device reliability, in: 2021 IEEE International Reliability Physics Symposium (IRPS), IEEE, 2021, pp. 1–8.
[28] S. Tudisco, F. La Via, C. Agodi, C. Altana, G. Borghi, M. Boscardin, G. Bussolino, L. Calcagno, M. Camarda, F. Cappuzzello, D. Carbone, S. Cascino, G. Casini, M. Cavallaro, C. Ciampi, G. Cirrone, G. Cuttone, A. Fazzi, D. Giove, G. Gorini, L. Labate, G. Lanzalone, G. Litrico, G. Longo, D. Lo Presti, M. Mauceri, R. Modica, M. Moschetti, A. Muoio, F. Musumeci, G. Pasquali, G. Petringa, N. Piluso, G. Poggi, S. Privitera, S. Puglia, V. Puglisi, M. Rebai, S. Ronchin, A. Santangelo, A. Stefanini, A. Trifirò, M. Zimbone, SiCILIA—silicon carbide detectors for intense luminosity investigations and applications, Sensors 18 (2018) 2289.
[29] R.K. Baruah, B.K. Mahajan, Y.-P. Chen, R.P. Paily, A junctionless silicon carbide transistor for harsh environment applications, J. Electron. Mater. 50 (2021) 5682–5690.
[30] E.J. Brandon, R. Bugga, J. Grandidier, J.L. Hall, J.A. Schwartz, S. Limaye, Power Beaming for Long Life Venus Surface Missions NIAC Phase I Final Report, Technical Report, 2020.
[31] P. Colter, B. Hagar, S. Bedair, Tunnel Junctions for III-V Multijunction Solar Cells Review, 2018.
[32] A.E. Arvanitopoulos, M. Antoniou, S. Perkins, M. Jennings, M.B. Guadas, K.N. Gyftakis, N. Lophitis, On the suitability of 3C-silicon carbide as an alternative to 4H-silicon carbide for power diodes, IEEE Trans. Ind. Appl. 55 (2019) 4080–4090.
[33] H. Ou, Y. Ou, A. Argyraki, S. Schimmel, M. Kaiser, P. Wellmann, M.K. Linnarsson, V. Jokubavicius, J. Sun, R. Liljedahl, M. Syväjärvi, Advances in wide bandgap SiC for optoelectronics, Eur. Phys. J. B 87 (2014) 58.
[34] E.D. Palik, S. Diego, L. Boston, N. York, S.T. Toronto, Handbook of Optical Constants of Solids, Technical Report, 1998.
[35] M.A. Green, J. Zhao, A. Wang, S.R. Wenham, 45% efficient silicon photovoltaic cell under monochromatic light, IEEE Electron Device Lett. 13 (1992) 317–318.
[36] Silvaco, Silvaco software (version 5.30.0.R), https://www.silvaco.com, 2020.
[37] M. Ochoa, E. Barrigón, L. Barrutia, I. García, I. Rey-Stolle, C. Algora, Limiting factors on the semiconductor structure of III-V multijunction solar cells for ultra-high concentration (1000-5000 suns), Prog. Photovolt. 24 (2016) 1332–1345.
[38] D.M. Caughey, R.E. Thomas, Carrier mobilities in silicon empirically related to doping and field, Proc. IEEE 55 (1967) 2192–2193.
[39] G.L. Harris, Properties of Silicon Carbide, EMIS Datareviews Series, vol. 13, INSPEC, Institution of Electrical Engineers, London, 1995.
[40] U. Lindefelt, A model for doping-induced band gap narrowing in 3C-, 4H-, and 6H-SiC, Mater. Sci. Eng. B 61–62 (1999) 225–228.
[41] L. Patrick, W.J. Choyke, Optical absorption in n-type cubic SiC, Phys. Rev. 186 (1969) 775–777.
[42] S.G. Sridhara, R.P. Devaty, W.J. Choyke, Absorption coefficient of 4H silicon carbide from 3900 to 3250 Å, J. Appl. Phys. 84 (1998) 2963–2964.
[43] A. Valera, E.F. Fernández, P.M. Rodrigo, F. Almonacid, Feasibility of flat-plate heat-sinks using microscale solar cells up to 10,000 suns concentrations, Sol. Energy 181 (2019) 361–371.
[44] A. Arvanitopoulos, N. Lophitis, S. Perkins, K.N. Gyftakis, M. Belanche Guadas, M. Antoniou, Physical parameterisation of 3C-Silicon Carbide (SiC) with scope to evaluate the suitability of the material for power diodes as an alternative to 4H-SiC, in: 2017 IEEE 11th International Symposium on Diagnostics for Electrical Machines, Power Electronics and Drives (SDEMPED), IEEE, 2017, pp. 565–571.
[45] S. Onoda, T. Ohshima, T. Hirao, K. Mishima, S. Hishiki, N. Iwamoto, K. Kawano, Impact of auger recombination on charge collection of a 6H-SiC diode by heavy ions, IEEE Trans. Nucl. Sci. 54 (2007) 2706–2713.
[46] Y. Goldberg, M. Levinshtein, S. Rumyantsev, Properties of advanced semiconductor materials: GaN, AIN, InN, BN, SiC, SiGe, SciTech Book News 25 (2001) 93–146.
[47] Z. Cheng, J. Liang, K. Kawamura, H. Zhou, H. Asamura, H. Uratani, J. Tiwari, S. Graham, Y. Ohno, Y. Nagai, T. Feng, N. Shigekawa, D.G. Cahill, High thermal conductivity in wafer-scale cubic silicon carbide crystals, Nat. Commun. 13 (2022).
[48] F. La Via, A. Severino, R. Anzalone, C. Bongiorno, G. Litrico, M. Mauceri, M. Schoeler, P. Schuh, P. Wellmann, From thin film to bulk 3C-SiC growth: understanding the mechanism of defects reduction, Mater. Sci. Semicond. Process. 78 (2018) 57–68.
[49] T.T. Mnatsakanov, M.E. Levinshtein, L.I. Pomortseva, S.N. Yurkov, Carrier mobility model for simulation of SiC-based electronic devices, Semicond. Sci. Technol. 17 (2002) 974–977.
[50] M. Ruff, H. Mitlehner, R. Helbig, SiC devices: physics and numerical simulation, IEEE Trans. Electron Devices 41 (1994) 1040–1054.
[51] J.F. Lozano, N. Seoane, E. Comesaña, F.M. Almonacid, E.F. Fernández, A. García-Loureiro, Photogeneration and performance optimization (PhPO): a new algorithm to improve the performance of vertical epitaxial hetero-structure architecture laser power converters, IEEE Access 11 (2023) 84371–84378.
[52] R.A. Sinton, A. Cuevas, Contactless determination of current–voltage characteristics and minority-carrier lifetimes in semiconductors from quasi-steady-state photoconductance data, Appl. Phys. Lett. 69 (1996) 2510–2512.

USC UNIVERSIDADE DE SANTIAGO DE COMPOSTELA

List of Figures

Fig. 1.1 Artistic example of a high power laser transmission application, a moon rover powered by a remote laser. In the zoom-in yellow circles, a horizontal laser power converter and a cubic silicon carbide structure are depicted. 12

Fig. 2.1 IV curve of a photovoltaic device. The main points I_{SC}, V_{OC}, *maximum power* (P_M), *voltage at the maximum power point* (V_M) and *current at the maximum power point* (I_M) are highlighted. 18

Fig. 2.2 The three device structures used in this work, the a) hLPC, b) vLPC and c) a VEHSA with 3 cells. 23

Fig. 2.3 Detailed optimization of each design parameter. Efficiency TCAD is the simulation aimed to obtain the efficiency of the evaluated cell. η_0 , η, and η_{max} are the initial, latest simulated and maximum efficiencies of the evaluated cell, respectively. 25

Fig. 2.4 2D-Schematic of a VEHSA device. The variable resistances in tunnel junctions allow to extract the current diferences from the adjacent cells. C1, C2, . . . , Cn are the cells of the VEHSA device. The zoom-in shows the detailed structure of the cell C1, composed by n+/n/p/p+ layers, with a CH1 total height. PH1 and NH1 are the heights of C1 p and n layers, respectively. . . . 27

Fig. 2.5 Flowchart of the different stages of the PhPO method. Photogeneration TCAD and TJC TCAD are simulations aimed to obtain the photogeneration of each cell and the currents extracted in the tunnel junctions (TJC), respectively. The optimum device height is fixed in the photogeneration loop and used as an input to the performance loop. 29

USC UNIVERSIDADE DE SANTIAGO DE COMPOSTELA

Fig. 3.1 Efficiency versus input power density (P_{in}) for the three SiC polytypes using the hLPC architecture. The best performance experimental GaAs-hLPC is included for comparison[17]. 35
Fig. 3.2 Efficiency versus input power density (P_{in}) for the 3C-SiC hLPCs optimized at 1 W cm^{-2} (opt1), 100 W cm^{-2}(opt100), and 1000 W cm^{-2} (opt1000). . . . 36
Fig. 3.3 Efficiency versus temperature for the three hLPC-SiC polytypes optimized at 1000 W cm^{-2}. 38
Fig. 3.4 IV curves comparing the experimental[16] VEHSA PT5 against the optimized structure provided by the PhPO method. The calibrated VEHSA PT5 is also included as validation. 40
Fig. 3.5 IV curves for each cell that composes the calibrated VEHSA PT5. Note that there is an appreciable dispersion in the values of Isc and, to a lesser degree, in those of Voc. 41
Fig. 3.6 IV curves for each cell that composes the optimized VEHSA PT5. Note that, unlike in the case of the calibrated device, there is no dispersion observed in either Isc or Voc. 42
Fig. 3.7 IV curves for the optimized (solid lines) and calibrated (dotted lines) VEHSA PT5 at three temperatures: 223 K (blue), 298 K (green) and 373 K (red). . . 43
Fig. 3.8 IV curves, normalised to each I_{SC}, for various optimized input power densities (P_{in}) in the hLPC. 45
Fig. 3.9 IV curves, normalised to each I_{SC}, for various optimized input power densities (P_{in}) in the vLPC. 46
Fig. 3.10 V_{OC} and V_M dependence on input power density (P_{in}) for the hLPC and vLPC. 46
Fig. 3.11 JV curves of 3C SiC-based devices using the hLPC architecture and VEHSAs with 2, 3 and 4 cells at 1 W cm^{-2}. 50
Fig. 3.12 JV curves of 3C SiC-based devices using the hLPC architecture and VEHSAs with 2, 3 and 4 cells at 3000 W cm^{-2}. 51
Fig. 3.13 Efficiency versus input power density for present work and several state-of-the-art LPCs. vLPC and hLPC refer to the 3C-SiC architectures studied in this work. The LPCs shown correspond to Outes[19], Helmers[17] (illumination area of 0.054 cm^{2}), York[21], Zhao[74], Huang[73], Reichmuth[18] and Kimovec[78]. 53

List of Tables

Tab. 2.1 Material parameters for 3C-SiC, 4H-SiC, 6H-SiC and GaAs included in the simulation framework. The bandgap[45] [REF FALTA GaAs], incident wavelength (λ), thermal conductivity (κ)[46][REF FALTA GaAs] and effective densities of states in the conduction/valence bands(N_C/N_V) [44][REF FALTA GaAs], are shown. 19

Tab. 2.2 Caughey-Thomas mobility parameters for 3C-SiC, 4H-SiC and 6H-SiC. The GaAs doping-dependant mobilities are implemented through a Silvaco internal data taken from empirical measurements. The μ_{max} and μ_{min} GaAs values shown correspond to doping values of 1e14 cm^{-3} and 1e20 cm^{-3}, respectively. 20

Tab. 2.3 Fitting parameters for 3C-SiC, 4H-SiC, 6H-SiC and GaAs, for the recombination models *Shockley–Read–Hall* (SRH), Auger and optical. 22

Tab. 3.1 Optimum design parameters of 3C, 4H and 6H SiC hLPCs at laser power densities (P_{in}) of 1, 100 and 1000 W cm^{-2}. The thicknesses and doping values of the P and N layers are shown. 33

Tab. 3.2 Main figures of merit for the three SiC polytypes using the hLPC architecture, being these: Short circuit current density (J_{SC}), open circuit voltage (V_{OC}), the V_{OC} growth with the laser power density (ΔV_{OC}), the fill factor (FF) and efficiency (Eff). Results are shown for input laser power densities (P_{in}) ranging from 1 to 1000 W cm^{-2}. 33

USC UNIVERSIDADE DE SANTIAGO DE COMPOSTELA

Tab. 3.3 Design parameters (DP) for the VEHSA PT5 validation and optimization. DH and CH are the device and cell heights in microns, NH/PH the N/P layer heights in percent and ND/PD the doping values for the N/P layers, respectively. The width is set to 10 μm. 39
Tab. 3.4 vLPC optimization results and figures of merit for different input power densities (P_{in}). The p and n-layer thickness and doping concentrations are optimized, as well as the vLPC width (see Figure 2.2b). The short circuit current I_{SC}, short circuit current density J_{SC}, quantum efficiency QE, open circuit voltage V_{OC}, voltage at the maximum power point V_M, fill factor FF and efficiency η are shown. The incident wavelength is 525 nm for all the P_{in} values. 44
Tab. 3.5 Design parameters (DP) of the VEHSA devices at 1 and 3000 W cm^{-2}. CH is the cell height, NH/PH the relative N/P layer heights in percentage of the respective CH and ND/PD the doping values for the N/P layers. 49
Tab. 3.6 Voltage (V_M) and current density (J_M) at the maximum power point for the hLPC architecture and all the individual cells of the VEHSA-2, VEHSA-3 and VEHSA-4 for 1 and 3000 W cm^{-2} laser power densities. 50

USC UNIVERSIDADE DE SANTIAGO DE COMPOSTELA

Acronyms

3C-SiC *Cubic Silicon Carbide* 14, 19, 21, 31, 35, 36, 41–43, 45, 47, 52, 55–58, 104

4H-SiC *Hexagonal 4H Silicon Carbide* 14, 19, 21, 31, 55

6H-SiC *Hexagonal 6H Silicon Carbide* 14, 19, 21, 31, 55

DOS *Density Of States* 18, 19, 56

Eff *efficiency* 17

FF *fill factor* 17, 34, 44, 45, 49

FoM *Figures of Merit* 17

GaAs *Gallium Arsenide* 12–14, 18–22, 26, 31, 51, 52, 56–59

hLPC *horizontal Laser Power Converter* 14, 15, 22–24, 31–38, 42–53, 55–59, 103–106

HPLT *High-Power Laser Transmission Technology* 11, 12, 14, 55

I_{M} *current at the maximum power point* 17, 18, 103

I_{SC} *short circuit current* 17, 18, 27, 40, 45, 46, 57, 103, 104

J_{SC} *short circuit current density* 33

LPC *Laser Power Converter* xi, 11–15, 17, 19, 22, 23, 31, 32, 37, 41, 51, 55, 56, 58, 59

USC
UNIVERSIDADE DE SANTIAGO DE COMPOSTELA

LPCs *Laser Power Converters* 15, 21, 24

P_{in} *Input power density* 17, 32–37, 42–46, 48, 51–53, 55, 56, 58, 104–106

P_M *maximum power* 17, 18, 103

PhPO *Photogeneration and Performance Optimization* xi, 15, 24, 31, 32, 37, 55–58

QE *Quantum Efficiency* 26, 42, 43

Si *Silicon* 14, 22

SiC *Silicon Carbide* xi, 13–15, 18–22, 31, 32, 35, 38, 41, 55, 56, 58, 59, 104

SRH *Shockley–Read–Hall* 20, 22, 105

TCAD *Technology Computer Aided Design* xi, 11, 15, 18, 26, 32, 37, 55–57

TJ *tunnel junctions* 14

V_M *voltage at the maximum power point* 17, 18, 39, 43–46, 103, 104

V_{OC} *open circuit voltage* 13, 17, 18, 24, 33–35, 40, 43–46, 49, 52, 56, 57, 103, 104

VEHSA *Vertical Epitaxial Hetero-Structure Architecture* xi, 13–15, 22–26, 31, 32, 37, 41, 42, 47, 51, 52, 55–58, 103

vLPC *vertical Laser Power Converters* 13–15, 22–24, 31, 32, 41–46, 52, 53, 55, 57, 58, 103, 104, 106

WPT *Wireless Power Transfer* 11

USC UNIVERSIDADE DE SANTIAGO DE COMPOSTELA

Two routes to increase the efficiency of the LPC technology have been studied in this thesis. First, the introduction in the common hLPC architecture of three high bandgap semiconductors as base materials for LPCs, being these the Silicon Carbide (SiC) polytypes 3C, 4H and 6H. Second, the implementation of these materials in advanced LPC architectures developed to reduce the series resistance losses, being these configurations the vertical Laser Power Converters (vLPC) and the Vertical Epitaxial Hetero-Structure Architecture (VEHSA). In addition, this second route required the development of optimization techniques for the VEHSA architecture. The presented work opens a promising route towards efficiently transmit ultra-high laser power densities.